

AN ABSTRACT OF THE THESIS OF

Ian M. Davis for the degree of Master of Science in Nuclear Engineering presented on March 10, 2005.

Title: Neutron Transport Benchmarks For Binary Stochastic Multiplying Media: Planar Geometry, Two Energy Groups.

Redacted for privacy

Abstract approved: _____

Todd S. Palmer

Benchmark calculations are performed for neutron transport in a two material (binary) stochastic multiplying medium. Spatial, angular, and energy dependence are included. The problem considered is based on a fuel assembly of a common pressurized water nuclear reactor. The mean chord length through the assembly is determined and used as the planar geometry system length. According to assumed or calculated material distributions, this system length is populated with alternating fuel and moderator segments of random size. Neutron flux distributions are numerically computed using a discretized form of the Boltzmann transport equation employing diffusion synthetic acceleration. Average quantities (group fluxes and k-eigenvalue) and variances are calculated from an ensemble of realizations of the mixing statistics. The effects of varying two parameters in the fuel, two different boundary conditions, and three different sets of mixing statistics are assessed. A probability distribution function (PDF) of the k-eigenvalue is generated and compared with previous research. Atomic mix solutions are compared with these benchmark ensemble average flux and k-eigenvalue solutions.

Mixing statistics with large standard deviations give the most widely varying ensemble solutions of the flux and k-eigenvalue. The shape of the k-eigenvalue PDF qualitatively agrees with previous work. Its overall shape is independent of variations in fuel cross-sections for the problems considered, but its width is impacted

by these variations. Statistical distributions with smaller standard deviations alter the shape of this PDF toward a normal distribution. The atomic mix approximation yields large over-predictions of the ensemble average k-eigenvalue and under-predictions of the flux. Qualitatively correct flux shapes are obtained, however. These benchmark calculations indicate that a model which includes higher statistical moments of the mixing statistics is needed for accurate predictions of binary stochastic media k-eigenvalue problems. This is consistent with previous findings.

©Copyright by Ian M. Davis

March 10, 2005

All Rights Reserved

Neutron Transport Benchmarks For Binary Stochastic Multiplying Media:
Planar Geometry, Two Energy Groups

by

Ian M. Davis

A THESIS

submitted to

Oregon State University

in partial fulfillment of
the requirements for the
degree of

Master of Science

Presented March 10, 2005
Commencement June 2005

Master of Science thesis of Ian M. Davis presented on March 10, 2005.

APPROVED:

Redacted for privacy

Major Professor, representing Nuclear Engineering

Redacted for privacy

Head of the Department of Nuclear Engineering and Radiation Health Physics

Redacted for privacy

Dean of Graduate School

I understand that my thesis will become part of the permanent collection of Oregon State University libraries. My signature below authorizes release of my thesis to any reader upon request.

Redacted for privacy

Ian M. Davis, Author

ACKNOWLEDGEMENTS

First and foremost, I would like to thank my advisor, Dr. Todd Palmer. I have had the unique and distinct pleasure of being a student of his as an undergraduate from 1997-2001 and as a graduate student for the last two years. Dr. Palmer has always been extremely patient, thoughtful, and considerate, and has provided me with much excellent guidance and counsel during the time I have known him. I feel that I have learned a great deal about transport theory and the process of conducting research as his student. If I am one day regarded as even a fraction of the scientist, mentor, and friend that he is to so many people, I can look back on my career favorably.

I would also like to thank Joel Risner at Bechtel Bettis Atomic Power Laboratory for acting as my laboratory advisor while a Naval Nuclear Propulsion Fellow. Joel has also provided me with excellent advice and has worked hard on my behalf, supporting my research efforts and assembling a very interesting research topic for my practicum assignment. I would also like to thank the NNP Fellowship program for the excellent funding and support they have provided me as a NNP fellow. Special thanks is necessary to Nancy Carder at the Medical University of South Carolina as my point of contact with the fellowship program.

In addition, I would like to thank the remaining members of my thesis committee Dr. Rubin Landau from the Department of Physics, Dr. Shoichi Kimura from the Department of Chemical Engineering, and Dr. Wu from the Department of Nuclear Engineering and Radiation Health Physics.

I would also like to thank my friend and fellow graduate student Greg Davidson. Greg was a pleasure to work with, and was essential in providing me with excellent technical feedback, guidance for L^AT_EX styling, and great suggestions regarding

programming technique and philosophies for writing better code. Although I did not get the opportunity to work directly with Brenton Ching, as a former graduate student of Dr. Palmer's, his organized coding style, L^AT_EX styling, and excellent thesis were invaluable references to me. I would also like to thank my friend and fellow graduate student Eric Young. Having already gone through the process of writing a Master's Thesis, Eric gave very helpful feedback and positive reinforcement during this process for me. Eric and his wife Selia also displayed a unique kindness throughout the tougher points of this process, keeping me well fed and encouraged.

I would absolutely be remiss if I did not mention my incredible family for their continued love and support. My father and mother, Mack and Diane Davis, and grandfather and grandmother, Merrill and Joyce M^cCarty, have instilled in me the importance of education as far back as I can remember. They have continually provided me with a tremendous amount of selfless support throughout this difficult process. Some of my most fond memories I have from childhood involve long discussions with my grandfather Merrill, who first introduced me to the breadth of scientific endeavor. I am also very grateful for the love and support of my sister Sidnie, my Aunt Gwen, and Selina Day throughout the process of writing this thesis.

This research was performed under appointment to the Naval Nuclear Propulsion Fellowship Program sponsored by Naval Reactors Division of the U.S. Department of Energy.

TABLE OF CONTENTS

	<u>Page</u>
1 INTRODUCTION	1
1.1 Literature Review	7
1.1.1 Boundary Value Problems in Stochastic Media	7
1.1.2 Eigenvalue Problems in Stochastic Media	17
1.2 Thesis Overview	23
2 THE BOLTZMANN TRANSPORT EQUATION	25
2.1 Introduction	25
2.2 Modeling Philosophies for Radiation Transport	25
2.3 The Boltzmann Transport Equation	27
2.4 The Analytic Steady-State Eigenvalue Problem in General Geom- etry	30
2.5 Discretization of the Planar Geometry Eigenvalue Problem with Isotropic Scattering	33
2.5.1 Angular Discretization	33
2.5.2 Energy Discretization	34
2.5.3 Spatial Discretization	35
2.6 Richardson and Power Iteration	38
2.6.1 Diffusion Synthetic Acceleration	42
2.6.2 Accelerated Reflecting Boundary Conditions	49
2.7 Summary	52
3 NEUTRON TRANSPORT IN STOCHASTIC MEDIA	54
3.1 Introduction	54

TABLE OF CONTENTS (Continued)

	<u>Page</u>
3.2 Modeling Stochastic Background Media	54
3.3 Mixing Statistics	59
3.4 Cross Section Data	65
3.5 Calculations	67
3.6 Summary	69
4 RESULTS	71
4.1 Introduction	71
4.2 Ensemble Average Group Flux Behavior	71
4.3 Code Validation and Statistical Convergence	74
4.4 Markov-Markov Mixing Statistics - Vacuum Boundaries	76
4.4.1 The k-Eigenvalue	76
4.4.2 Scalar Flux	80
4.4.3 The Atomic Mix Approximation	86
4.5 Markov-Markov Mixing Statistics - Reflecting Boundaries	87
4.5.1 The k-Eigenvalue	88
4.5.2 Scalar Flux	88
4.5.3 The Atomic Mix Approximation	92
4.6 Disk-Markov Mixing Statistics - Vacuum Boundaries	95
4.6.1 The k-Eigenvalue	96
4.6.2 Scalar Flux	98
4.6.3 The Atomic Mix Approximation	106
4.7 Disk-Markov Mixing Statistics - Reflecting Boundaries	107

TABLE OF CONTENTS (Continued)

	<u>Page</u>
4.7.1 The k-Eigenvalue	108
4.7.2 Scalar Flux	108
4.7.3 The Atomic Mix Approximation	112
4.8 Disk-Matrix Mixing Statistics - Vacuum Boundaries	115
4.8.1 The k-Eigenvalue	115
4.8.2 Scalar Flux	119
4.8.3 The Atomic Mix Approximation	124
4.9 Disk-Matrix Mixing Statistics - Reflecting Boundaries	126
4.9.1 The k-Eigenvalue	126
4.9.2 Scalar Flux	127
4.9.3 The Atomic Mix Approximation	131
4.10 Markov-Markov, Disk-Markov, and Disk-Matrix PDF Comparison	134
4.11 Summary	137
5 CONCLUSIONS	138
5.1 Introduction	138
5.2 k-Eigenvalue	138
5.3 Scalar Flux	140
5.4 Atomic Mix	144
5.5 Overall Conclusions and Future Work	146
BIBLIOGRAPHY	148

LIST OF FIGURES

<u>Figure</u>		<u>Page</u>
1	Flow Chart of Inner and Outer Transport Iterations	41
2	Flow Chart of Realization Construction	56
3	Flow Chart of Complete Algorithm	58
4	Relative Error of Ensemble Quantities as a Function of Realization	58
5	1/4 Fuel Assembly	59
6	Generation of an Assembly Chord Length	60
7	Distribution of Chord Length in Moderator Material of a 17x17 Fuel Assembly	64
8	Fast Group Solution, Calculation 1.1, Realization 50	72
9	Thermal Group Solution, Calculation 1.1, Realization 50	72
10	Four Thermal Group Scalar Flux Solutions and the Ensemble Av- erage Solution - Calculation 1.1	73
11	Convergence of the Fast Group Ensemble Average Scalar Flux - Calculation 1.1	74
12	Convergence of the Thermal Group Ensemble Average Scalar Flux - Calculation 1.1	75
13	k-Eigenvalue PDF - Calculation 1.1.1	79
14	k-Eigenvalue PDF - Calculation 1.1.2	79
15	k-Eigenvalue PDF - Calculation 1.1.3	80
16	k-Eigenvalue PDF - Calculation 1.3.1, 1.3.2, 1.3.3	81
17	k-Eigenvalue PDF - Calculation 1.1.1, 1.2.1, 1.3.1	81

LIST OF FIGURES (Continued)

<u>Figure</u>		<u>Page</u>
18	Ensemble Average Fast Group Flux - Calculation 1.1.1	84
19	Ensemble Average Fast Group Flux - Calculation 1.3.1	84
20	Ensemble Average Thermal Group Flux - Calculation 1.1.1	85
21	Ensemble Average Thermal Group Flux - Calculation 1.3.1	85
22	k-Eigenvalue PDF - Calculation 1.1	89
23	k-Eigenvalue PDF - Calculation 1.2	89
24	k-Eigenvalue PDF - Calculation 1.3	90
25	k-Eigenvalue PDF - Calculation 1.1 - Calculation 1.3	90
26	Ensemble Average Fast Group Flux - Calculation 1.1	92
27	Ensemble Average Fast Group Flux - Calculation 1.3	93
28	Ensemble Average Thermal Group Flux - Calculation 1.1	93
29	Ensemble Average Thermal Group Flux - Calculation 1.3	94
30	k-Eigenvalue PDF - Calculation 2.2.1	97
31	k-Eigenvalue PDF - Calculation 2.2.2	98
32	k-Eigenvalue PDF - Calculation 2.2.3	99
33	k-Eigenvalue PDF - Calculation 2.1.1, 2.1.2, 2.1.3	99
34	k-Eigenvalue PDF - Calculation 2.1.2, 2.2.2, 2.3.2	100
35	Ensemble Average Fast Group Flux - Calculation 2.1.2	102
36	Ensemble Average Fast Group Flux - Calculation 2.3.2	103
37	Ensemble Average Thermal Group Flux - Calculation 2.1.2	103
38	Ensemble Average Thermal Group Flux - Calculation 2.3.2	104

LIST OF FIGURES (Continued)

<u>Figure</u>	<u>Page</u>
39 Fast Group Material Average Scalar Flux - Calculation 2.2.2	105
40 Fast Group Material Average Scalar Flux with Fixed Fuel Segment Length - Calculation 2.2.2	105
41 k-Eigenvalue PDF - Calculation 2.1	109
42 k-Eigenvalue PDF - Calculation 2.2	109
43 k-Eigenvalue PDF - Calculation 2.3	110
44 k-Eigenvalue PDF - Calculation 2.1 - Calculation 2.3	110
45 Ensemble Average Fast Group Flux - Calculation 2.1	112
46 Ensemble Average Fast Group Flux - Calculation 2.3	113
47 Ensemble Average Thermal Group Flux - Calculation 2.1	113
48 Ensemble Average Thermal Group Flux - Calculation 2.3	114
49 k-Eigenvalue PDF - Calculation 3.3.1	117
50 k-Eigenvalue PDF - Calculation 3.3.2	118
51 k-Eigenvalue PDF - Calculation 3.3.3	118
52 k-Eigenvalue PDF - Calculation 3.2.1 - Calculation 3.2.3	119
53 k-Eigenvalue PDF - Calculation 3.1.3 - Calculation 3.3.3	120
54 Ensemble Average Fast Group Flux - Calculation 3.1.3	122
55 Ensemble Average Fast Group Flux - Calculation 3.3.3	122
56 Ensemble Average Thermal Group Flux - Calculation 3.1.3	123
57 Ensemble Average Thermal Group Flux - Calculation 3.3.3	123
58 Fast Group Material Average Scalar Flux - Calculation 3.2.2	125

LIST OF FIGURES (Continued)

<u>Figure</u>	<u>Page</u>
59	k-Eigenvalue PDF - Calculation 3.1 128
60	k-Eigenvalue PDF - Calculation 3.2 128
61	k-Eigenvalue PDF - Calculation 3.3 129
62	k-Eigenvalue PDF - Calculation 3.1 - Calculation 3.3 129
63	Ensemble Average Fast Group Flux - Calculation 3.1 131
64	Ensemble Average Fast Group Flux - Calculation 3.3 132
65	Ensemble Average Thermal Group Flux - Calculation 3.1 132
66	Ensemble Average Thermal Group Flux - Calculation 3.3 133
67	k-Eigenvalue PDF Mixing Statistics Comparison - Calculation x.2.1 135
68	k-Eigenvalue PDF Mixing Statistics Comparison - Calculation x.2.2 135
69	k-Eigenvalue PDF Mixing Statistics Comparison - Calculation x.2.3 136

LIST OF TABLES

<u>Table</u>	<u>Page</u>
1	Cross Sections by Material and Energy Group 66
2	Calculation Set 1 Variable Parameter Values, Vacuum Boundaries . 68
3	Calculation Set 2 Variable Parameter Values, Vacuum Boundaries . 68
4	Calculation Set 3 Variable Parameter Values, Vacuum Boundaries . 68
5	Calculation Set 1-3 Variable Parameter Values, Reflecting Boundaries 69
6	Designation of the Material Segment Length Distributions For Each Calculation Set 77
7	k-Eigenvalue Results for Set 1; Markov-Markov Statistics, Vacuum Boundaries 77
8	Fast Group Flux Results for Set 1; Markov-Markov Statistics, Vac- uum Boundaries 82
9	Thermal Group Flux Results for Set 1; Markov-Markov Statistics, Vacuum Boundaries 83
10	Atomic Mix Prediction of the Ensemble Average k-Eigenvalue for Set 1; Markov-Markov Statistics, Vacuum Boundaries 86
11	Ensemble Average / Atomic Mix Ratio of Group Scalar Flux Solu- tions for Set 1; Markov-Markov Statistics, Vacuum Boundaries . . . 87
12	k-Eigenvalue Results for Set 1; Markov-Markov Statistics, Reflecting Boundaries 88
13	Fast Group Flux Results for Set 1; Markov-Markov Statistics, Re- flecting Boundaries 91

LIST OF TABLES (Continued)

<u>Table</u>	<u>Page</u>
14 Thermal Group Flux Results for Set 1; Markov-Markov Statistics, Reflecting Boundaries	91
15 Atomic Mix Prediction of the Ensemble Average k-Eigenvalue for Set 1; Markov-Markov Statistics, Reflecting Boundaries	94
16 Ensemble Average / Atomic Mix Ratio of Group Scalar Flux Solutions for Set 1; Markov-Markov Statistics, Reflecting Boundaries	95
17 k-Eigenvalue Results for Set 2; Disk-Markov Statistics, Vacuum Boundaries	96
18 Fast Group Flux Results for Set 2; Disk-Markov Statistics, Vacuum Boundaries	101
19 Thermal Group Flux Results for Set 2; Disk-Markov Statistics, Vacuum Boundaries	101
20 Atomic Mix Prediction of the Ensemble Average k-Eigenvalue for Set 2; Disk-Markov Statistics, Vacuum Boundaries	106
21 Benchmark / Atomic Mix Ratio of Group Scalar Flux Solutions for Set 2; Disk-Markov Statistics, Vacuum Boundaries	107
22 k-Eigenvalue Results for Set 2; Disk-Markov Statistics, Reflecting Boundaries	108
23 Fast Group Flux Results for Set 1; Disk-Markov Statistics, Reflecting Boundaries	111
24 Thermal Group Flux Results for Set 1; Disk-Markov Statistics, Reflecting Boundaries	111

LIST OF TABLES (Continued)

<u>Table</u>	<u>Page</u>
25 Atomic Mix Prediction of the Ensemble Average k-Eigenvalue for Set 2; Disk-Markov Statistics, Reflecting Boundaries	114
26 Ensemble Average / Atomic Mix Ratio of Group Scalar Flux Solutions for Set 2; Disk-Markov Statistics, Reflecting Boundaries	115
27 k-Eigenvalue Results for Set 3; Disk-Matrix Statistics, Vacuum Boundaries	116
28 Fast Group Flux Results for Set 3; Disk-Matrix Statistics, Vacuum Boundaries	120
29 Thermal Group Flux Results for Set 3; Disk-Matrix Statistics, Vacuum Boundaries	121
30 Atomic Mix Prediction of the Ensemble Average k-Eigenvalue for Set 3; Disk-Matrix Statistics, Vacuum Boundaries	125
31 Benchmark / Atomic Mix Ratio of Group Scalar Flux Solutions for Set 3; Disk-Matrix Statistics, Vacuum Boundaries	126
32 k-Eigenvalue Results for Set 3; Disk-Matrix Statistics, Reflecting Boundaries	127
33 Fast Group Flux Results for Set 3; Disk-Matrix Statistics, Reflecting Boundaries	130
34 Thermal Group Flux Results for Set 3; Disk-Matrix Statistics, Reflecting Boundaries	130
35 Atomic Mix Prediction of the Ensemble Average k-Eigenvalue for Set 3; Disk-Matrix Statistics, Reflecting Boundaries	133

LIST OF TABLES (Continued)

<u>Table</u>		<u>Page</u>
36	Ensemble Average / Atomic Mix Ratio of Group Scalar Flux Solutions for Set 3; Disk-Matrix Statistics, Reflecting Boundaries	134

NEUTRON TRANSPORT BENCHMARKS FOR BINARY STOCHASTIC MULTIPLYING MEDIA: PLANAR GEOMETRY, TWO ENERGY GROUPS

1 INTRODUCTION

In recent years, the radiation transport community has shown increased interest in particle interaction with a stochastic or random heterogeneous background medium. The background medium is considered stochastic or random for this class of problems since the precise location of any one of its constituents is not explicitly known. In most nuclear engineering applications, the composition of the background media is fixed. Further, it is common practice to treat material mixtures as homogenous at the atomic level by averaging the isotopic properties by their respective volume fractions. This is a reasonable approximation when the length scale of the material microstructure is less than a mean free path of the particle. Very accurate modeling techniques have been developed for particle transport and diffusion calculations for which the background material is a fixed homogenous mixture.

All materials encountered in nature have some degree of heterogeneity. The assumption that a medium is a homogenous mixture of its components can have various effects on modeling the interaction of particles with the medium. As a particle traverses a heterogeneous mixture, it may encounter pockets of distinctly different material in the microstructure of the medium, causing profoundly different bulk particle flow effects than would be predicted by a homogeneous model. In these cases, the heterogeneous microstructure has to be given specific treatment.

A large body of work now exists for modeling particle transport in stochastic media, but this area of research is still very active. Interest in these problems was

generated in an attempt to accurately describe radiative transfer in a capsule undergoing the implosion stage in inertial confinement fusion [Pom 91b] and [Pom 90b]. This is a system where there is radiative transfer through a medium composed of two fluids of drastically different densities, accelerated toward one another by the propagation front of the implosion shock wave [Cha 61]. The lighter fluid pushes on and accelerates the denser fluid, causing a thin layer of turbulent mixing of these two immiscible materials by a Rayleigh-Taylor type instability. If this layer is modeled as a homogeneous mixture, the radiation transport solutions in this medium suffer from unacceptably large errors.

Since then, focus has turned to other problems spanning a diverse set of disciplines with interest in particle transport, where a stochastic treatment of the background medium is necessary. Stars form in our galaxy from molecular clouds which are a randomly mixed medium of gas and dust grains. The development of models which can accurately determine the radiation transport in such a heterogeneous cloud and the subsequent temperature effect on the medium has been the subject of some research in the astronomy and astrophysics community. Models which can reproduce observed properties of molecular clouds are an important tool in understanding star formation [Boi 90].

Modeling heterogeneous mixtures may become necessary in fully understanding radiation transport and modeling errors in some already mature applications. This may include the thermalhydraulic and neutron density coupling in boiling water reactors where the neutrons traverse a bubbly flow (water-void mixtures). Common materials used in radiation shielding, such as cement, may be treated more accurately as stochastic media where particles may interact with large regions of constituents with different neutron interaction probabilities.

Explicit modeling of the microstructure is also necessary in global climate modeling. Clouds are heterogeneous mixtures of water vapor and ice. Their composition, coverage, and vertical thickness dictate how much sunlight is reflected back into space and how much is absorbed and subsequently reemitted to the Earth's surface. An understanding of cloud structure and the bulk radiative transport effects through them are fundamental to accurate atmospheric and oceanic circulation models. Since radiative transport through a cloudy atmosphere still is not well understood, global climate models produce unacceptably erroneous solutions in the oceanic transport of heat, and predict global warming with uncertainty ranges which have not improved much in over two decades [Ste 02].

Pebble bed nuclear reactors have at least three levels of stochasticity. The fuel pebble itself is a random mixture of smaller fuel spheres in a graphite matrix used for moderation. These pebbles are tightly packed and randomly mixed in the core region surrounded by gaseous coolant. An additional layer of stochasticity is introduced after the reactor has been in operation for some time and the fuel in each pebble is depleted by the fission process at variable rates as they migrate through the core.

Radiation transport in nuclear reactor systems in which the fuel and moderator are a stochastic mixture is the focus of this thesis. Quantifying the impact of randomness in these systems is important from a reactor operations and safety analysis standpoint. The problems characteristic of nuclear reactor systems are eigenvalue problems, where the dominant eigenvalue is an indication of the change in neutron population with successive generations, also known as the multiplication factor. The associated eigenvector is the neutron flux, or "fundamental mode". There are two types of eigenvalue problems commonly of interest in nuclear reactor

analysis: transient and steady-state eigenvalue problems.

When evaluating nuclear reactor systems, changes in the reactor material composition on both a short or long time scale can cause a subsequent change in the eigenvalue indicating the multiplication factor of the neutron population. Examples of those changes on a short time scale (fractions of seconds to minutes) include control rod motion to change the power level in the reactor or the unlikely event of a loss of coolant accident, for which robust safety systems have been designed. Longer scale changes (days to months) include the “burnup” of fissile isotopes in the reactor, where the available fuel in the reactor is decreased by the fission process. Neutron “poisons” embedded in the fuel are also depleted which has the subsequent effect of a reactivity insertion. Poisons are also added to the reactor chemistry for long-term control purposes. The build up and decay of fission products such as iodine and xenon also act as poisons causing fluctuations in the time-dependent reactor criticality which must be anticipated for a constant power level. These mechanisms causing complicated time-dependent reactor behavior on such scales are the subject of reactor kinetics and dynamics [Dud 76].

Reactor kinetics and dynamics in the context of a stochastic background medium *are not* the subject of this thesis. Although some of these problems, such as burnable poison grains with random locations in a modern fuel pellet, are excellent candidates for further stochastic media transport research [San 91]. Problems in which the fuel and moderator loading of a reactor are sampled from a distribution and placed randomly in the reactor geometry are the stochastic reactor criticality problems which *are* the subject of this thesis. The steady-state system behavior described by the fundamental eigenvalue-eigenfunction transport theory solution is evaluated in planar geometry.

Stochastic media transport research has centered around two basic elements: benchmarks and models. The statistical nature of a stochastic media transport problem enters through the random mixing of the components of the background medium. At any point in the mixture, a particle may encounter one of the material components or an interface between components with a probability governed by the mixing statistics. Benchmark radiation transport calculations in a stochastic media is straightforward but computationally expensive, while approximate models are complicated to derive, but ideally should be simple to implement, computationally inexpensive, and yield accurate results. Benchmark calculations for stochastic media involve randomly populating the geometry with segments of each of the constituents whose sizes are determined by known or assumed statistical distributions, and then performing a transport calculation for the aggregate. This is known as a single realization of the statistics. Many realizations are performed, with each transport solution contributing to a statistical solution comprised of an average and higher order statistical moments for the ensemble. Thousands, if not millions, of realizations are performed to ensure that the distributions have been well sampled, and that ensemble solutions have converged.

If the mixing statistics are known with any certainty, a particle transport solution can be generated for an individual realization of the medium as well as statistical ensemble quantities. However, it is clear that the computational expense of this calculation can quickly become prohibitive as multi-material mixtures in two or three dimensions, with full temporal, energy, and angular dependence are contemplated. Since analytical solutions are not possible except in the simplest of systems, approximate numerical models must be derived. The accuracy of these models are then unknown except in certain limits, which can be analyzed. Bench-

mark calculations provide an “exact” answer, acting as a metric against which models can be compared. Insight and understanding gained from benchmark calculations have been used to derive and improve models which predict statistical ensemble quantities.

Deterministic models were developed first from physical understanding of radiation transport for certain types of simple stochastic media systems. When approximations were introduced into these early models to expand their capacity to predict the ensemble behavior of a wider variety of systems, benchmarks were then needed to ascertain the effect of these approximations on the model accuracy. From that point, both benchmarks and models began incorporating more physics, and were capable of providing more accurate solutions of stochastic media systems with increased complexity.

This research has centered around two important types of particle transport problems: boundary value problems of the form $\underline{\underline{\mathbf{A}}}\underline{\underline{\psi}} = \underline{\underline{\mathbf{q}}}$ and eigenvalue problems of the form $\underline{\underline{\mathbf{A}}}\underline{\underline{\psi}} = \lambda\underline{\underline{\mathbf{F}}}\underline{\underline{\psi}}$. The subject of this thesis is eigenvalue problems for stochastic media transport, but the rich history of research and acquired understanding from the analysis of boundary value problems is relevant in this discussion.

The remainder of the introduction is a literature review in the following section, which gives an overview of the published literature on particle transport for stochastic media to date. Research which has been conducted involving benchmarking and modeling for both the boundary value and eigenvalue problem will be reviewed. This will illustrate how the scope of research has narrowed to benchmark calculations for the energy dependent eigenvalue problem. The literature review will be followed by an overview of the remaining sections of the thesis in Section 1.2.

1.1 Literature Review

A review of the literature characterizing particle transport in stochastic media is given in this section. A discussion is given regarding both the eigenvalue problem and the boundary value problem for particle transport in stochastic media. The boundary value problem in stochastic media was first considered and has been researched the most thoroughly of the two problem types. Therefore, the literature review will begin with the boundary value problem.

1.1.1 *Boundary Value Problems in Stochastic Media*

Most of the work to date regarding boundary value problems for particle transport in stochastic media has considered source free, isotropic scattering, monoenergetic transport in rod or planar geometry. Rod geometry means that particles are constrained to move along a line in either the positive or negative direction. Boundary value problems are driven by a particle flux incident on the stochastic medium from its exterior. Quantities of interest are the transmission and reflection probability, as well as the particle flux profile in the interior of the medium.

The most well known, easiest to implement, and consequently, most widely used model is known as atomic mix. This approximation is typically used for fixed (non-stochastic) medium applications. The atomic mix approximation effectively homogenizes a mixture by volume-averaging the characteristics of its constituents. This is a reasonable approximation for media with constituent sizes that are small compared to a mean free path of the transported particle [Mal 92], known as the small correlation length limit. For constituent sizes on the order of a particle mean free path or longer, the atomic mix approximation has been shown to overestimate the absorption as a general trend ([Mal 92], [Mil 01], and [Dav 04]).

Much of the effort to develop models for transport in stochastic media has been centered around deriving accurate models for benchmark calculations in which the material segments or transition lengths are exponentially distributed, or Markovian. It has been shown that a Markovian process is associated with a “no-memory” initial value problem where, if the solution is known at some time (t), then the solution is uniquely defined for some later time (t') ([Pom 91a],[Pom 91b], and [Pom 98]). This is known as a no-memory process since a solution at (t') and later can be calculated from the known solution at (t). Solutions previous to (t) are unnecessary.

The steady-state Boltzmann transport equation governing particle flow (see Section 2.3) in a purely absorbing medium is a spatial Markovian process. Such a system with assumed Markovian mixing statistics for all material components describes a joint Markov process, and the Liouville master equation applies. For a binary mixture, application of the master equation results in two coupled partial differential equations with four unknowns: the volumetric angular flux and interface angular flux in each material. Some relation is needed to close this system of equations, which are known as the Levermore-Pomraning equations. If the interface angular flux is set equal to the volumetric angular flux, the Levermore-Pomraning equations are exact for time independent problems in purely absorbing, binary stochastic media, with Markovian mixing statistics [Pom 90b]. The Levermore-Pomraning equations with this upwind closure will hereafter be referred to as the “classic” model. Exact equations can be written for higher order statistical moments of the classic model (such as the variance) for this same class of problems [Pom 96b]. Statistical moments greater than the average should be included as part of a complete and more meaningful statistical solution for particle transport

in a stochastic medium.

The assumption of Markovian mixing statistics is not purely for academic purposes. It has been shown that in the case of a binary stochastic medium in which disks or spheres are distributed in a background material, that the assumption of Markovian statistics in the background material is reasonable ([Su 93] and [Ols 03]). Results from two-dimensional hydrodynamic calculations indicate that fluid segment lengths in a turbulently mixed, binary stochastic media are Markovian in nature [Pom 90b]. Fragment sizes in rock have also been shown to be exponentially distributed [Pom 90b].

Separate derivations have lead to the classic model, including the method of smoothing, application of the Liouville master equation, the assumption of uncorrelated particle trajectories, reactor noise techniques, and particle balance arguments [Pom 91c]. The classic model simplifies to the atomic mix model when the transition lengths become vanishingly small, and becomes the standard transport equation for transition lengths which increase without bound [Mal 92].

There are other models which are exact for binary stochastic media, but they are limited in scope or result in very complicated expressions. Two independent sets of kinetic equations have been developed which independently and exactly describe time-dependent particle transport with arbitrary mixing statistics in the full three-dimensional setting including scattering [San 89]. Unfortunately, each set of equations does not close, resulting in an infinite system of coupled equations and, while providing a theoretical basis for construction of approximate models, are not amenable to application. The theory of alternating renewal processes yields four coupled, exact transport equations for a purely absorbing, binary stochastic medium without the restriction of Markovian statistics, but including Markovian

statistics as a special case ([Pom 89], [Fri 90], and [Pom 98]). Exact equations for higher statistical moments can be written for this model as well. An extension of this model has been recommended as an approximation to systems including time dependence and scattering [Pom 89]. For a time-independent, purely scattering binary stochastic medium in rod geometry, an exact model has been formulated using the invariant imbedding method [Van 89], and with a more general formalism [Pom 88].

These exact equations are for specialized cases and it is unknown how to extend them rigorously as a general model which is easily solvable. In many applications of particle transport, it is common for the background material to be modestly to highly scattering. Therefore, more generalized models have been, and continue to be, derived and investigated which include the scattering interaction in general geometries. The classic model is known to be exact in time-independent, purely absorbing media, but its ability to predict ensemble flux behavior for the boundary value problem with scattering was unknown. With the introduction of scattering, the transport problem no longer is Markovian and the classic model becomes an approximation. When compared against early benchmark studies in which scattering was allowed in one or both of the materials, the classic model was shown to underestimate the reflection probability and overestimate the transmission probability in both the rod and planar geometries in systems that were sufficiently long ([Ada 89], [Zuc 94], and [Mil 01]). It has been shown that the effective cross section (see Section 2.3) for purely scattering media goes through a pronounced minimum at some system length ([Su 95] and [Van 89]). This “transmission window” is not predicted by the classic model as the system length increases, but predicts that the effective cross section monotonically decreases as a function of system length.

This demonstrates why the classic model fails to accurately predict the flux profile and transmission probability, for systems of sufficient length which include the scattering interaction.

Different closures for the Levermore-Pomraning equations have been proposed which include the scattering interaction. It seems impossible to derive a set of closure equations relating the volumetric material angular flux to the interface material angular flux which results in an exact, general model [Su 95]. More complex closures which include scattering have been the subject of much research ([Ada 89], [Pom 91c], [Su 94], and [Su 95]).

Two additional low order closures were developed from a small transition length analysis (small segment lengths in one or both of the materials) in an attempt to approximate the scattering interaction and capture the atomic mix limit [Su 94]. While these closures are more complex, they are algebraic and thus still considered low order closures. It is unclear how to determine these closure relationships in other than an *ad hoc*, problem-specific way. These closures show only slight improvement, or in some cases, a deterioration in the accuracy when compared with the classic model. Neither of these more complex low order closures predict the transmission window and therefore none of the low order closure models (including the classic model) are well suited as a general model ([Su 94] and [Su 95]).

A higher order closure was developed from a “balance like” equation for the angular flux at the interface of two materials in a binary stochastic medium [Pom 91b]. This yields additional transport equations relating the interface flux to the volumetric flux in each material, resulting in four coupled transport equations. Pomraning named this the “Interface” model. Solving these four transport equations results in a significant improvement over the classic model in approximating the reflection

and transmission probabilities of a time independent, source-free, monoenergetic, isotropic scattering, rod geometry benchmark. However, evaluating four coupled transport equations comes with significant computational expense, and there is no obvious way to extend this closure to general geometries and statistics. The overall conclusion of research on closure schemes for the Levermore-Pomraning equations is that more complex models lead to more accurate solutions [Mal 92]. The Interface model gives more accurate reflection and transmission probabilities compared to the classic model, but sometimes yields unphysical flux profiles in the system interior. The Interface model has been shown to be the only closure capable of predicting the transmission window with any accuracy.

A linear combination of the Interface model and the classic model was also developed in an *ad hoc* way such as to preserve the best qualities of each model [Su 95]. For purely absorbing media, the combined model goes to the classic model, which is exact. For purely scattering systems, the combined model goes to the Interface model which is the best prediction of these systems.

This model was tested for monoenergetic systems in rod and planar geometry with isotropic scattering. Numerical tests against benchmark solutions revealed that the combined model was both robust and yielded accurate results. There are a few specific systems where the combined model was found to be inaccurate. However, since the combination of the classic and Interface model was done in an *ad hoc* way, the model can be “tuned” to specific problems to obtain very accurate results. Therefore, the combined model was recommended as a replacement for both the classic model and the Interface model for source free, isotropically scattering, monoenergetic, binary mixtures in rod and planar geometry, but still cannot be considered a general model [Su 95].

Some of these models have been extended to other transport applications. A low order closure [Su 94] was used in approximating time-dependent grey radiation transport in a purely absorbing binary stochastic media where the transport was coupled to the matter [Mil 01]. The assumption of a source-free, purely absorbing media was made with a linear form of the material temperature equation. The binary stochastic medium was purely absorbing, but the coupling to the matter can be thought of as a scattering source, where the thermal radiation absorbed is reemitted isotropically with some probability. The cases considered were in the small transition length limit which, from the above discussion, is the assumption under which the low order closures of [Su 94] were derived. This model was shown to be a much better approximation than either atomic mix or the classic model since it takes into account the scattering interaction.

Benchmarking studies have been conducted for non-Markovian statistics as well ([Zuc 94] and [Su 93]). Considering eight different mixing statistics in planar geometry, it was shown that the probability of transmission was more statistics dependent than the probability of reflection for systems of sufficient length. Particles which penetrate deeply into the slab would tend to encounter more of the possible variation present in the slab than those particles which partially penetrate the slab and reflect back out. Another important result of this study was that different mixing statistics produce different results in the flux distributions. Furthermore, the mean and variance of the statistical distribution describing the mixing statistics indicate the influence of the mixing statistics on the transport problem. For the different unimodal statistical distributions evaluated, it was shown that the material and ensemble average scalar fluxes are insensitive to statistical moments higher than the second, this being especially true in the case of well mixed systems (small

transition lengths relative to the system length) ([Lev 88] and [Zuc 94]). These studies also revealed that the mean segment length alone was insufficient statistical information for modeling purposes. This has significant impact on modeling particle transport in stochastic media. If one is modeling a mixture with unimodal mixing statistics, one can choose any unimodal distribution with an equivalent mean and variance, and get accurate results if a reasonable model is chosen.

A correction factor to the classic model was developed to include non-Markovian statistics [Lev 88]. Both the classic model and Interface model incorporating this correction were tested against the Renewal model [Zuc 94]. All three models are exact for time-independent, purely absorbing stochastic mixtures with Markovian statistics. The Renewal model is also exact for the above class of problems for non-Markovian mixing statistics. The Renewal model was found to more robustly predict the qualitative behavior of the flux profile as well as the reflection and transmission probability relative to the corrected classic and Interface models.

So far only deterministic models which have been developed for particle transport in stochastic media have been discussed. There has been some benchmarking and modeling research done for particle transport in stochastic media using the Monte Carlo method (see Section 2.2). A chord length sampling (CLS) and limited chord length sampling (LCLS) algorithm have been adopted into a standard Monte Carlo calculation. The application was neutral particle transport in a binary stochastic medium consisting of a fixed number of disks randomly placed in a matrix material ([Don 03a] and [Don 03b]).

In a standard analog Monte Carlo calculation, a particle history is simulated by choosing the minimum of the distances to collision, to escape, or to a material interface. This is based on the particle's current position, direction, and what ma-

terial it resides in. The CLS algorithm replaces the calculation for the distance to a material interface with a sampling from the mixing statistics to determine whether or not the particle advances to a material interface. This models the stochastic mixture by sampling the material mixing statistics in an approximate way as the particle traverses the medium. This can be much less computationally expensive than a Monte Carlo benchmark calculation. This algorithm was shown to be equivalent to the classic, deterministic model in rod geometry. The CLS algorithm assumes a Markovian transition length distribution in the matrix material, and a distribution describing chord lengths in a disk for the disk material. This assumption is not necessarily a reasonable one for particles which penetrate the surface of the disk, since this distribution will be an overestimation of the distance to escape from the disk for any particle whose position is in the disk's interior.

The LCLS algorithm was developed which uses the CLS algorithm in the matrix material, and traditional Monte Carlo in the disk material. When considering the reflection probability on incident flux boundaries, and the transmission probability on the other boundaries, both the CLS and LCLS algorithms were found to be within the statistical error of the benchmark calculation for purely absorbing systems. When scattering is introduced both algorithms become approximate with varying degrees of accuracy, with LCLS being the most accurate in general. As in the case of the classic model, it was shown that the CLS algorithm underestimates reflection and overestimates transmission. CLS and LCLS show a dramatic increase in computational efficiency relative to the Monte Carlo benchmark. The one exception to this result is in the case of CLS in the purely scattering case with high probability of interaction in the disc material. This result is expected since CLS is known to give an overestimate of the chord lengths in the disc material as

discussed above. In the case where there is a large probability of the scattering interaction in the disc, a particle would artificially spend a much longer time in the disc material than it would in analog Monte Carlo.

Another interesting model is the Woodcock algorithm, which uses the Monte Carlo method and a Perlin noise function as an alternative algorithm to analog Monte Carlo [Tic 04]. Like the CLS and LCLS algorithms, the Woodcock algorithm determines what media the particle is in as it traverses the medium, reducing the computational expense relative to the benchmark calculation. However, in the case of the Woodcock algorithm it is unnecessary to compute the distance to material interfaces. When the algorithm determines a point of interaction, the Perlin noise function is evaluated to determine what material is assigned to that interaction point. This model was shown to accurately predict measured fluorescent x-ray intensity from a granular Cu_2S sample excited with a ^{238}Pu source. This model could be extended to potentially simulate a broad variety of complicated stochastic media systems.

Modeling and benchmarking strategies have been summarized for boundary value particle transport problems in stochastic media. The subject of this thesis is eigenvalue problems in binary stochastic media, but the research that has been performed for boundary value problems is relevant to the modeling and benchmarking of eigenvalue problems. A detailed summary and complete list of references of the research efforts on benchmarks, exact models, and closures for approximate models for boundary value particle transport problems in stochastic media can be found in [Pom 98] and [Pom 96a].

A review of research done in the development of models and benchmarks for particle transport stochastic mixtures reveals no general model which is accurate

for systems which include a moderate or high amount of scattering, or for the case of arbitrary mixing statistics, in general geometry. It may be possible to utilize one of the aforementioned models to treat the eigenvalue problem. However, knowledge of the stochastic system is necessary to choose a model which may have to be “tuned” to the specific system, or developed from first principles. Therefore, benchmarks will continue to be developed to gain understanding of specific systems to improve current models, and to develop new models.

1.1.2 Eigenvalue Problems in Stochastic Media

Relative to the bulk of research on boundary value problems, only a small amount of research has been devoted to the development of benchmarks and models for stochastic eigenvalue problems. In the stochastic nuclear reactor, at least one component of the background mixture is a multiplying component. If a neutron interacts with such a component, the reemission factor can be greater than unity from the fission process, where it would be unity for a purely scattering component and zero for a purely absorbing component. Much of this research has used diffusion theory as the basis for analysis, which does not adequately capture the complicated aspects of particle transport in a random multiplying medium. Furthermore, the effect of randomness on the ensemble average criticality of a stochastic nuclear reactor can be ambiguous. This is contrary to the particle flux, where the ensemble average can be precisely defined, as in the solution to the boundary value problem.

Analytical results from monoenergetic diffusion theory have demonstrated the difficulty in trying to make general conclusions regarding the effect of randomness on criticality [Pom 91a]. Different indicators can be used as interpretations of the criticality of a system. Furthermore, these indicators can be averaged differently

to calculate the average criticality of the ensemble. It was shown using different, averaged criticality indicators that the ensemble average criticality will increase, decrease, or stay constant given the same random perturbation about a reference reactor. These conflicting conclusions about the same random system suggest that neutron transport in a stochastic multiplying medium is far too complicated to make any general conclusion about the effect of “randomness” on “criticality” using a single ensemble averaged number. It must be specified how ensemble averaged criticality is interpreted, and how randomness is introduced into the system. Characterizations of a specific random media system as subcritical or supercritical may be too simple, and higher statistical moments of the specified criticality indicator are necessary for a complete solution.

Steady-state, monoenergetic, planar geometry transport for a bare stochastic reactor has also been considered [Jah 98]. A critical, homogenous slab reactor with vacuum boundary conditions was used as a reference case. A heterogeneous slab was then composed of plates of homogenous material, keeping the material loading equal to the reference case, for each realization. This is different from [Pom 91a], since material loading is conserved in individual realizations and for the overall ensemble, while in [Pom 91a], material loading was conserved only for the ensemble. The segment thickness and number of segments were sampled from both binomial and exponential distributions, and later using multinomial statistics [Jah 01]. In the case of the binomial and multinomial statistics, the exact number of perturbations were known for a given segment length, resulting in no sampling error. For the exponential statistics, the distribution was sampled until the ensemble average k -eigenvalue had converged to some criteria. Based on results from these three statistical distributions for the monoenergetic problems considered, any dis-

tribution which does not preferentially distribute fuel to the edges of the reactor will result in a greater ensemble average k-eigenvalue than in the homogeneous reference case.

As the plate size becomes smaller and the slab composition approaches the homogeneous case, the ensemble average k-eigenvalue approaches critical strictly from above. This was true for variable reemission values from 1 to ν (see Section 2.3). This result shows that if homogenization techniques such as atomic mix are used to model multiplying media with components of at least a certain minimum size, it will consistently under predict the ensemble average k-eigenvalue. This is interesting from a reactor safety or criticality safety standpoint. Examination of individual eigenvalues contributing to the ensemble average revealed that the fraction of k-eigenvalues less than unity is smaller than the fraction greater than unity. For the small fraction of eigenvalues less than unity, the deviation from critical is smaller than the fraction of eigenvalues greater than unity. This corresponds to an ensemble average which is supercritical in all the cases evaluated. For these studies it was shown that the departure of the ensemble averaged k-eigenvalue is largest when the slab has little or no scattering interaction. The reverse is true when the slab is highly scattering. The random structure impacts the ensemble averaged k-eigenvalue the greatest for highly absorbing slabs because particles travel a short distance on average. When the slab is highly scattering, the effect of the random structure is reduced, since the scattering interaction will “smooth out” the effect of the random structure. Thus, the reactor which is purely absorbing and the reactor which is highly scattering give the bounds for the maximum and minimum change in the eigenvalue for these monoenergetic calculations.

Using the monoenergetic diffusion equation describing a Markovian binary

stochastic reactor, the ensemble averaged reactivity is always greater than the nonstochastic reference case [Pom 99]. Randomness was introduced into the problem differently than in [Jah 98] and [Jah 01] by fluctuations of the mean number of secondaries per collision about the ensemble average of this quantity. This result was found to be true only for rods of sufficient length and is dependent on what mode of the eigenvalue is of interest. If higher modes are considered the opposite conclusion can be drawn on the effect of randomness on criticality. In nuclear reactor analysis, usually it is the fundamental mode that is of primary interest.

Much research has been done by M.M.R. Williams on stochastic multiplying media problems using the Feinberg-Galanin-Horning (FGH) method for heterogeneous reactors ([Wil 00a],[Wil 00b],[Wil 01],[Wil 02], and [Wil 03a]- [Wil 03c]). The FGH method was used by Williams in these studies for benchmark type calculations, but is a simple model of the complexities of radiation transport in a stochastic reactor. This method employs diffusion theory and models the fuel material as a point source of fast neutrons and a point sink of thermal neutrons in a matrix of moderating material with an approximate slowing down kernel. Using the critical size of an ordered lattice of source-sink points in a moderator matrix as the reference case, the effect of random placement of source-sink points was investigated, while preserving the total number of source-sink points in the problem. The source-sink points were either placed in the moderator matrix at random, or perturbed from their ordered position by a random fraction of the pitch. Some general conclusions were drawn about heterogeneous reactors of this type, and probability distribution functions (PDF) were created for the k-eigenvalue to demonstrate the effect of randomness on the specific systems. Both one-dimensional and three-dimensional bare and reflected systems were considered.

An overall conclusion of these studies was that a maximum k-eigenvalue would occur when the source-sink points resided in some optimal positioning near the reactor center (a small reflected core), and a minimum when the points resided near the reactor edge (a system with high leakage). For the simplest of one-dimensional studies, it was found that random plate positions lead to a preferentially supercritical ensemble average for randomly distributed source-sink points. When the positions of the source-sink points are perturbed a small amount from their fixed positions, the resulting probability distribution function is symmetric around unity and Gaussian in shape. A Gaussian like distribution is also approached for an increasing number of source-sink points with a corresponding decrease in the variance. This is expected since the placement of materials becomes less random with an increase in the number of source-sink points.

The FGH model was extended to include resonance absorption and variable enrichment in the source-sink points. The source-sink points were composed of ^{238}U and ^{235}U and allowed variable enrichment and fixed position, variable position and fixed enrichment, and both variable enrichment and position. For this material mixture in the source-sink points, all values of the ensemble average k-eigenvalue were found to be subcritical. This is also the result when random absorbing strengths are allowed for the source-sink points. When the material composition of the source-sink points was changed to be ^{235}U and ^{27}Al and the source-sink positions chosen at random from the critical reference case, it was found that there exists an ensemble of reactors whose average k-eigenvalue is greater than or less than unity for a given number of source-sink points. In the case of those subcritical ensemble average k-eigenvalues, they are less than, but very close to unity. Since it was unknown in this study what type of error was made in calculating the ensem-

ble average k -eigenvalue for the given number of realizations, it is unknown if this subcriticality is attributed to statistical sampling error. Thus, the inclusion of this approximate energy dependence shows a departure from the previous conclusions that randomness increases the ensemble average k -eigenvalue.

A review of the literature given above points naturally to an area of research in stochastic media transport which has yet to be undertaken. Research for eigenvalue problems in stochastic media has not been explored as thoroughly as the boundary value problem. Of the work that has been done, very little has employed transport theory. For stochastic reactor problems randomly distributed sources and strong absorbers can be present on variable spatial scales where diffusion will be a poor approximation. To accurately define the behavior of statistical moments of the ensemble k -eigenvalue for benchmarking purposes, transport theory will be required. None of the research employing transport theory to investigate eigenvalue problems in stochastic media has included energy dependence. The work done by Williams includes energy dependence in an approximate sense using diffusion theory.

An understanding of the behavior of stochastic nuclear reactors developed from benchmark studies employing steady-state, energy dependent transport theory is the goal of this thesis. The mean and variance of the ensemble k -eigenvalue are used as the specific indications of reactivity, and probability distribution functions of the k -eigenvalue are constructed. Comparisons with the atomic mix approximation will also be explored. Mixing statistics will include Markovian (and others) for consistency with past research with the intent of gathering data to guide the development of accurate models from the current, previous, and successive works. This work is a natural extension of the research done in this area to date.

1.2 Thesis Overview

The remainder of this thesis is organized as follows:

- II. In Chapter 2, the general geometry, analytic Boltzmann transport equation is introduced. The transport equation is a representation of the transport of neutral particles in any arbitrary medium. Several assumptions are made, and the analytic transport equation for planar geometry is derived. The discretization schemes used to discretize each of the independent variables in planar geometry transport are introduced. The iteration techniques are then described in which this discretized transport equation is solved, resulting in a solution composed of a neutron flux and multiplication factor (eigenvalue-eigenvector pair). A derivation of the diffusion synthetic acceleration procedure used to improve the rate of convergence is also included here.
- III. In Chapter 3, the algorithm for modeling stochastic media and integration of the deterministic transport method into this algorithm is described. Convergence of the statistical solution is discussed. The binary stochastic medium problem considered in this study is defined, and a physical basis is given for both the mixing statistics and material cross sections. The sets of calculations performed are provided.
- IV. In Chapter 4, flux results for individual realizations are given to aid in the understanding of ensemble flux results. A brief description of code validation is given. Tables of results and representative plots of both the ensemble flux solution and probability distribution function of the k-eigenvalue are provided for each set of calculations performed, for each boundary condition

type. Trends in the results are identified for the group ensemble average scalar flux and standard deviation and the ensemble average k-eigenvalue and standard deviation. The atomic mix prediction of benchmark ensemble average quantities is assessed.

- V. In Chapter 5, conclusions are drawn from the trends identified in Chapter 4 for the k-eigenvalue, the group scalar flux, and the atomic mix approximation. Overall conclusion are made and possible future work is discussed.

2 THE BOLTZMANN TRANSPORT EQUATION

2.1 Introduction

This chapter provides a discussion of the modeling philosophies in current numerical radiation transport calculations and the deterministic method used in this study. The governing analytic Boltzmann transport equation describing neutron transport in any arbitrary medium is provided. The assumptions behind this are given, as is an example of the particular eigenvalue problem solved and its physical significance. Further assumptions are made to the analytic general geometry Boltzmann transport equation, arriving at the analytic planar geometry transport equation. The discretization techniques for the spatial, energy, and angular variables are then discussed, yielding a system of equations which are solved numerically in an iterative fashion. The nested iterative procedure used to solve this system of equations is outlined. Finally, there is a detailed derivation of the preconditioner of the system of equations used as a synthetic acceleration scheme to improve the convergence rate of the iterative solution procedure.

2.2 Modeling Philosophies for Radiation Transport

There currently exists two major, and for the most part separate, particle transport modeling philosophies for any media: deterministic and Monte Carlo. Deterministic transport involves designing methods to explicitly solve the Boltzmann transport equation. The Boltzmann transport equation considers an arbitrary volume and those mechanisms by which particles enter or escape that volume. The transport equation is a complicated integro-differential equation, and cannot be

solved analytically except for highly idealized problems. Current deterministic transport research includes improving the speed, accuracy, and physical fidelity of calculations. The diffusion equation has been a successful approximation to the transport equation in many applications. The quantity of interest in a deterministic calculation is typically the particle flux of the system (and k -eigenvalue if applicable), obtained to some requested deterministic error.

Monte Carlo transport simulates individual particle tracks from their time and place of birth, through each interaction with the background medium, until they eventually escape from the system or become absorbed. This simulation is statistical in nature, but it can be shown that it solves the integral form of the Boltzmann transport equation in the limit of an infinite number of particle histories. Current Monte Carlo transport research centers primarily around variance reduction, where an accurate mean behavior of the solution can be obtained more rapidly by giving particles important to the measurement of interest greater weight than those that make little or no contribution. The Monte Carlo solution is also typically related to a particle flux solution (and k -eigenvalue if applicable), but is statistical in nature and has an associated statistical error.

This study involves deterministic solutions of the transport equation. This choice was made because a transport solution in one dimension can be obtained much more rapidly when using a deterministic method than a Monte Carlo method. Also, the solution of a deterministic calculation gives the flux profile for the entire system, instead of only at specified locations, which is usually the case in typical Monte Carlo calculations. The effect of random distributions of the constituents of the background material on the flux profile is of interest. The numerical solution approach to the stochastic mixture transport problem of this thesis does have a

statistical component to it, which will be described in more detail in Chapter 3. Next, a detailed description of the Boltzmann transport equation will be given, followed by the discretization procedures used for each independent variable.

2.3 The Boltzmann Transport Equation

The neutron transport equation gives the neutron distribution in a general, arbitrary phase space and is given by the Boltzmann transport equation:

$$\frac{\partial n}{\partial t} + v\hat{\Omega} \cdot \nabla n + \sigma vn = \int_{4\pi} d\hat{\Omega}' \int_0^\infty dE' \sigma_s(E' \rightarrow E, \hat{\Omega}' \rightarrow \hat{\Omega}) v' n(\mathbf{r}, E', \hat{\Omega}', t) + q \quad (1)$$

where,

t	=	time,
E or E'	=	energy,
\mathbf{v} or \mathbf{v}'	=	neutron velocity vector,
v or v'	=	$ \mathbf{v} $ or $ \mathbf{v}' $; neutron speed,
$\hat{\Omega}$ or $\hat{\Omega}'$	=	$\frac{\mathbf{v}}{ \mathbf{v} }$ or $\frac{\mathbf{v}'}{ \mathbf{v}' }$; unit vector for neutron direction of travel with both a polar and azimuthal component,
σ	=	$\sigma(\mathbf{r}, E)$; total macroscopic cross-section, or the probability per unit path length that a neutron at point \mathbf{r} with energy E will undergo some interaction,
$\sigma_s(E' \rightarrow E, \hat{\Omega}' \rightarrow \hat{\Omega})$	=	scattering cross-section, or the probability per unit path length that a neutron at point \mathbf{r} with energy E' traveling in direction $\hat{\Omega}'$ will scatter into the energy and direction of interest, $E, \hat{\Omega}$,

$n = n(\mathbf{r}, E, \hat{\Omega}, t) =$ angular neutron density at point \mathbf{r} , with energy E ,
moving in direction $\hat{\Omega}$, at time t ,

$q = q(\mathbf{r}, E, \hat{\Omega}, t) =$ source of neutrons at point \mathbf{r} , producing neutrons
with energy E , moving in direction $\hat{\Omega}$, at time t .

Thus, the Boltzmann transport equation is an exact equation for the angular neutron density through a balance of gain and loss mechanisms of neutrons in an arbitrary phase space, $(\mathbf{r}, E, \hat{\Omega}, t)$. Possible gain mechanisms, or ways in which neutrons appear in $(\mathbf{r}, E, \hat{\Omega}, t)$ include:

- **Sources** into $(\mathbf{r}, E, \hat{\Omega}, t)$ - fission or nuclide decay resulting in neutron production
- **Streaming** into $(\mathbf{r}, E, \hat{\Omega}, t)$ - neutrons moving into $(\mathbf{r}, E, \hat{\Omega}, t)$ from $(\mathbf{r}', E, \hat{\Omega}, t)$
- **Collision** into $(\mathbf{r}, E, \hat{\Omega}, t)$ - neutrons in $(\mathbf{r}, E', \hat{\Omega}', t)$ colliding into $(\mathbf{r}, E, \hat{\Omega}, t)$

Possible loss mechanisms, where neutrons disappear from $(\mathbf{r}, E, \hat{\Omega}, t)$ include:

- **Leakage** out of $(\mathbf{r}, E, \hat{\Omega}, t)$ - neutrons from $(\mathbf{r}, E, \hat{\Omega}, t)$ escape into $(\mathbf{r}', E, \hat{\Omega}, t)$
- **Collision** out of $(\mathbf{r}, E, \hat{\Omega}, t)$ - neutrons in $(\mathbf{r}, E, \hat{\Omega}, t)$ collide into $(\mathbf{r}, E', \hat{\Omega}', t)$ or are absorbed (including those that cause fission).

The Boltzmann transport equation is a linear, integrodifferential equation for the angular neutron density in a seven dimensional phase space, $(\mathbf{r} = x, y, z; E; \hat{\Omega} = \Theta, \gamma; t)$. It is assumed in the Boltzmann transport equation that [Lew 93]:

- Particles and the sites where they interact with the background medium are considered as points,
- Particles are so rarefied that they do not interact with one another,

- No forces influence the momentum of particles between interaction sites, so particles stream in straight lines,
- Collisions are considered instantaneous,
- Particles interact with the background material isotropically,
- The properties of the background material are assumed known and,
- Only the mean value of the particle distribution is considered.

Defining the angular neutron flux as a product of the angular neutron density and the neutron speed,

$$\psi(\mathbf{r}, E, \hat{\Omega}, t) = v n(\mathbf{r}, E, \hat{\Omega}, t), \quad (2)$$

it is convenient to rewrite the neutron transport equation in terms of the angular neutron flux,

$$\frac{\partial \psi}{\partial t} + \hat{\Omega} \cdot \nabla \psi + \sigma \psi = \int_{4\pi} d\hat{\Omega}' \int_0^\infty dE' \sigma_s(E' \rightarrow E, \hat{\Omega}' \rightarrow \hat{\Omega}) \psi(\mathbf{r}, E', \hat{\Omega}', t) + q, \quad (3)$$

since the neutron scalar flux, defined as,

$$\phi(\mathbf{r}, E, t) = \int_{4\pi} d\hat{\Omega}' \psi(\mathbf{r}, E, \hat{\Omega}', t) \quad (4)$$

is often the quantity of interest as it is the simplest to conceptualize and used in calculating reaction rates.

2.4 The Analytic Steady-State Eigenvalue Problem in General Geometry

With the Boltzmann transport equation defined (Eq. (1)), the eigenvalue problem investigated for a stochastic multiplying background medium can be developed using an example adopted from reference [Bel 70]. Consider the transport problem governed by Eq. (1) where the first generation of neutrons is a pulsed neutron source given as q_1 resulting in the angular neutron density of the first generation of neutrons in a multiplying medium,

$$\frac{\partial n_1}{\partial t} + v\hat{\Omega} \cdot \nabla n_1 + \sigma v n_1 = \int_{4\pi} d\hat{\Omega}' \int_0^\infty dE' \sigma_s(E' \rightarrow E, \hat{\Omega}' \rightarrow \hat{\Omega}) v' n_1(\mathbf{r}, E', \hat{\Omega}', t) + q_1. \quad (5)$$

Integrating over all time ($0 \leq t \leq \infty$) results in the first term on the left-hand-side going to zero, since the pulsed source is of finite duration. Those pulsed neutrons in that generation eventually scatter or leak out of the system, or are absorbed in the medium into either a multiplying component (fuel) or another non-multiplying component. The time integrated neutron source shall be denoted as $\tilde{q}_1 = \tilde{q}_1(\mathbf{r}, E, \hat{\Omega})$ and the time integrated angular neutron density as $\tilde{n}_1 = \tilde{n}_1(\mathbf{r}, E, \hat{\Omega})$ giving,

$$v\hat{\Omega} \cdot \nabla \tilde{n}_1 + \sigma v \tilde{n}_1 = \int_{4\pi} d\hat{\Omega}' \int_0^\infty dE' \sigma_s(E' \rightarrow E, \hat{\Omega}' \rightarrow \hat{\Omega}) v' \tilde{n}_1(\mathbf{r}, E', \hat{\Omega}', t) + \tilde{q}_1. \quad (6)$$

The second generation of neutrons, \tilde{n}_2 , are produced by those neutrons in \tilde{n}_1 which are absorbed in fuel and cause a fission. Thus, fission is the process by which a generation of neutrons gives birth to a subsequent generation, making it the

event separating generations. The source, \tilde{q}_2 , producing the second generation of neutrons, \tilde{n}_2 , is given by,

$$\tilde{q}_2 = \chi \int_{4\pi} d\hat{\Omega}' \int_0^\infty dE' \nu \sigma_f v' \tilde{n}_1(\mathbf{r}, E', \hat{\Omega}', t) \quad (7)$$

where,

$\chi = \chi(E)$; the probability that a neutron produced from fission will have energy E , where, $\int_0^\infty \chi(E) dE = 1$,

$\nu = \nu(E')$; the mean number of neutrons produced by fission from a neutron with energy E'

$\sigma_f = \sigma_f(\mathbf{r}, E')$; fission cross section, or the probability per unit path length that a neutron with energy E' is absorbed at point \mathbf{r} in fuel will fission.

Equations can be written in this manner for the $(i)^{th}$ generation of neutrons produced by the $(i-1)^{th}$ generation or by the following recursive equation,

$$v\hat{\Omega} \cdot \nabla \tilde{n}_i + \sigma v \tilde{n}_i = \int_{4\pi} d\hat{\Omega}' \int_0^\infty dE' \sigma_s(E' \rightarrow E, \hat{\Omega}' \rightarrow \hat{\Omega}) v' \tilde{n}_i(\mathbf{r}, E', \hat{\Omega}', t) + \chi \int_{4\pi} d\hat{\Omega}' \int_0^\infty dE' \nu \sigma_f v' \tilde{n}_{i-1}(\mathbf{r}, E', \hat{\Omega}', t). \quad (8)$$

As the number of generations becomes large for Eq. (8), the ratio of successive generations will be a constant, or,

$$\lim_{i \rightarrow \infty} \frac{\tilde{n}_i}{\tilde{n}_{i-1}} = \text{constant} = k \quad (9)$$

This constant k is known as the multiplication factor and indicates the ‘‘criticality’’ of the system. Calculating the multiplication factor is most often approached as an eigenvalue problem, where $\lambda = \frac{1}{k}$ and ψ are eigenvalue-eigenvector pairs that are solutions to the eigenvalue problem. In practical application, the ν of Eq. (7) is replaced by ν/k , or $\lambda\nu$, adjusting the average number of neutrons per fission to balance the equation. The maximum λ (or minimum k) and resulting eigenvector

(fundamental mode) are the quantities of interest for typical reactor analysis applications. For a system where $k < 1$ the neutron density in successive generations is decreasing, or the number of neutrons per fission, ν/k , required to make the system exactly critical is larger than ν . This is known as a subcritical system. If $k > 1$ the neutron density in successive generations is increasing, or the number of neutrons per fission, ν/k , required to make the system exactly critical is smaller than ν . This is known as a supercritical system. For $k = 1$, the total neutron population is unchanging from generation to generation; the total neutron gain mechanisms being exactly balanced by the loss mechanisms. This is known as a critical system. The resulting time-independent governing equation for this eigenvalue problem, written here in terms of the angular flux, is

$$\hat{\Omega} \cdot \nabla \psi + \sigma \psi = \int_{4\pi} d\hat{\Omega}' \int_0^\infty dE' \sigma_s(E' \rightarrow E, \hat{\Omega}' \rightarrow \hat{\Omega}) \psi(\mathbf{r}, E', \hat{\Omega}', t) + \frac{\chi}{k} \int_{4\pi} d\hat{\Omega}' \int_0^\infty dE' \nu \sigma_f \psi(\mathbf{r}, E', \hat{\Omega}', t). \quad (10)$$

This study is confined to planar geometry (1-D) and considers only isotropic scattering. Defining the single spatial variable x , and μ as the cosine of the angle measured from the x -axis, the above equation governing the eigenvalue problem of interest then becomes,

$$\mu \frac{\partial \psi}{\partial x} + \sigma \psi = \frac{1}{2} \left[\int_{-1}^1 d\mu' \int_0^\infty dE' \sigma_s(E' \rightarrow E) \psi(x, E', \mu') + \frac{\chi}{k} \int_{-1}^1 d\mu' \int_0^\infty dE' \nu \sigma_f \psi(x, E', \mu') \right], \quad (11)$$

where all of the dependent variables are written now as functions of the planar

geometry independent variables, i.e.

$$\psi = \psi(x, E, \mu). \quad (12)$$

2.5 Discretization of the Planar Geometry Eigenvalue Problem with Isotropic Scattering

Since the phase space has been confined to include a single angular and spatial variable as well as energy dependence, each of these variables is discretized. The transport equation is then solved at discrete values of each of the independent variables. This reduces the complicated integro-differential transport equation for the eigenvalue problem to a system of linear equations amenable to numerical solution.

2.5.1 Angular Discretization

To discretize the angular variable (μ) in the planar geometry transport equation, the well known S_N method is used [Lew 93]. The transport equation is rewritten as N linearly independent equations for the angular flux in each discrete angle μ_m ,

$$\psi(x, E, \mu_m) = \psi_m(x, E). \quad (13)$$

A symmetric Gauss-Legendre quadrature is chosen to numerically integrate this angular flux over angle yielding the scalar flux (zeroth angular moment),

$$\phi(x, E) = \int_{-1}^1 \psi(x, E, \mu') d\mu' \approx \sum_{m=1}^N w_m \psi_m(x, E), \quad (14)$$

and the current (first angular moment),

$$j(x, E) = \int_{-1}^1 \psi(x, E, \mu') \mu' d\mu' \approx \sum_{m=1}^N \mu_m w_m \psi_m(x, E), \quad (15)$$

where the weights of the quadrature set have been normalized such that,

$$\sum_m w_m = 2. \quad (16)$$

2.5.2 Energy Discretization

To discretize the energy variable (E), the multigroup approximation is employed (reference [Lew 93]). The multigroup approximation discretizes the continuous energy variable into G discrete energy groups, where the angular flux in each discrete group (g) is given as,

$$\psi_g(x, \mu) = \int_{E_g}^{E_{g-1}} \psi(x, E', \mu) dE', \quad E_g < E' \leq E_{g-1}. \quad (17)$$

The full energy integral can then be approximated by,

$$\int_0^\infty \psi(x, E', \mu) dE' = \sum_{g=1}^G \int_{E_g}^{E_{g-1}} \psi(x, E', \mu) dE', \quad E_g < E' \leq E_{g-1}. \quad (18)$$

Multigroup constants are then given as [Dud 76],

$$\sigma_g(x) = \frac{1}{\phi_g(x)} \int_{E_g}^{E_{g-1}} dE' \sigma(x, E') \phi(x, E'), \quad (19a)$$

$$\sigma_{s,g' \rightarrow g}(x) = \frac{1}{\phi_{g'}(x)} \int_{E_g}^{E_{g-1}} dE \int_{E_{g'}}^{E_{g'-1}} dE' \sigma_s(x, E' \rightarrow E) \phi(x, E'), \quad (19b)$$

$$\nu_g \sigma_{f,g}(x) = \frac{1}{\phi_g(x)} \int_{E_g}^{E_{g-1}} dE' \nu(E') \sigma_f(x, E') \phi(x, E'), \quad (19c)$$

$$\chi_g = \int_{E_g}^{E_{g-1}} dE' \chi(E'), \quad (19d)$$

where, $\phi_g(x)$ is given by Eq. (14) for $\psi_g(x)$.

Rewriting Eq. (11) with the discretizations in angle and energy yields for neutrons in a group (g) and quadrature direction (m),

$$\mu_m \frac{\partial \psi_{g,m}(x)}{\partial x} + \sigma_g(x) \psi_{g,m}(x) = \frac{1}{2} \sum_{g'=1}^G \sigma_{s,g' \rightarrow g}(x) \phi_{g'}(x) + \frac{\chi_g}{2k} \sum_{g'=1}^G \nu_{g'} \sigma_{f,g'}(x) \phi_{g'}(x). \quad (20)$$

The scope of this thesis is focused on calculations which include “in-group” or downscatter only. This is to say that if a neutron undergoes a scattering event, it can either experience no change in energy (coherent scatter) or a decrease in energy. This assumption is inserted into the first term of the right-hand-side of Eq. (20) giving,

$$\mu_m \frac{\partial \psi_{g,m}(x)}{\partial x} + \sigma_g(x) \psi_{g,m}(x) = \frac{1}{2} \sum_{g'=1}^g \sigma_{s,g' \rightarrow g}(x) \phi_{g'}(x) + \frac{\chi_g}{2k} \sum_{g'=1}^G \nu_{g'} \sigma_{f,g'}(x) \phi_{g'}(x), \quad (21)$$

where from the previously mentioned assumption of coherent or downscatter only, it is clear that, ($g' \leq g$). Defining the scattering source as,

$$S_g(x) = \sum_{g'=1}^g \sigma_{s,g' \rightarrow g}(x) \phi_{g'}(x), \quad (22)$$

and the fission source as,

$$F(x) = \sum_{g'=1}^G \nu_{g'} \sigma_{f,g'}(x) \phi_{g'}(x), \quad (23)$$

all source terms can be combined into a single source term, $Q_g(x)$,

$$Q_g(x) = S_g(x) + \frac{\chi_g}{k} F(x), \quad (24)$$

giving,

$$\mu_m \frac{\partial \psi_{g,m}(x)}{\partial x} + \sigma_g(x) \psi_{g,m}(x) = \frac{1}{2} Q_g(x). \quad (25)$$

This in-group transport equation will be the focus of the discussion in the next section on spatial discretization.

2.5.3 Spatial Discretization

The spatial discretization chosen for Eq. (25) is the linear characteristics method, since it provides highly accurate solutions and is not difficult to derive or implement

in planar geometry. The linear characteristic spatial discretization gives exact results for steady-state, purely absorbing media for planar geometry systems in which there is no interior source. Linear characteristics provides fourth-order accuracy otherwise [Ada 04]. The discretization is based on the assumption of a linear form of the total source as a first-order spatial expansion in Legendre polynomials,

$$Q_g(x) = Q_{i,g} [P_{0,i}(x)] + Q_{i,g}^x [P_{1,i}(x)] , \quad (26a)$$

where,

$$[P_{0,i}(x)] = 1 , \quad (26b)$$

$$[P_{1,i}(x)] = \frac{2(x - x_i)}{\Delta x_i} . \quad (26c)$$

This is often referred to as “slope-average” form. The analytic equation for the angular flux on the edges of a discrete spatial zone is found by integrating Eq. (25) over the length of the zone. This yields an equation for the angular flux exiting the zone in terms of the angular flux incident on the zone and the linear source in the zone,

$$\begin{aligned} \psi_{i_{exit},g,m} = \psi_{i_{inc},g,m} e^{-\sigma_{i,g}\Delta x_i/\mu_m} + \frac{1}{2\sigma_{i,g}} \left\{ Q_{i,g} (1 - e^{-\sigma_{i,g}\Delta x_i/\mu_m}) + \right. \\ \left. Q_{i,g}^x \left[(1 + e^{-\sigma_{i,g}\Delta x_i/\mu_m}) - \frac{2\mu_m}{\Delta x_i\sigma_{i,g}} (1 - e^{-\sigma_{i,g}\Delta x_i/\mu_m}) \right] \right\} . \quad (27) \end{aligned}$$

“Average” quantities are defined as:

$$f_i = \frac{1}{\Delta x_i} \int_{x_{inc}}^{x_{exit}} [P_{0,i}(x)] f(x) dx , \quad (28a)$$

and “slope” quantities are defined as:

$$f_i^x = \frac{3}{\Delta x_i} \int_{x_{inc}}^{x_{exit}} [P_{1,i}(x)] f(x) dx . \quad (28b)$$

The zeroth and first spatial moments of the transport equation yield, respectively,

$$\psi_{i,g,m} = \frac{Q_{i,g}}{2\sigma_{i,g}} - \frac{\mu_m}{\sigma_{i,g}\Delta x_i} (\psi_{i_{exit},g,m} - \psi_{i_{inc},g,m}), \quad (29)$$

and,

$$\psi_{i,g,m}^x = \frac{Q_{i,g}^x}{2\sigma_{i,g}} - \frac{3\mu_m}{\sigma_{g,i}\Delta x_i} (\psi_{i_{exit},g,m} + \psi_{i_{inc},g,m} - 2\psi_{i,g,m}). \quad (30)$$

Together with boundary conditions, Eq. (27), Eq. (29), and Eq. (30) form a closed set of equations which can be solved to obtain $\psi_{g,m,i}$ and $\psi_{g,m,i}^x$ in each zone by a “transport sweep”. Only vacuum boundary conditions on both of the system boundaries given by,

$$\psi_{1_{inc},g,m} = \psi_{1/2,g,m} = 0, \quad \mu_m > 0, \quad (31a)$$

$$\psi_{I_{inc},g,m} = \psi_{I+1/2,g,m} = 0, \quad \mu_m < 0, \quad (31b)$$

and specular reflection boundary conditions on both of the system boundaries given by,

$$\psi_{1/2,g,n} = \psi_{1/2,g,m}, \quad \mu_m < 0, \quad (32a)$$

$$\psi_{I+1/2,g,n} = \psi_{I+1/2,g,m}, \quad \mu_m > 0, \quad (32b)$$

$$\mu_n = -\mu_m \quad (32c)$$

for (I) total zones, are considered for the purposes of this study. Of course, in the case of specular reflection on both of the system boundaries results in an infinite medium, which has zero leakage. A single transport sweep begins at one edge of the system beginning with the incoming information from the boundary condition, and “sweeps” the spatial mesh toward the opposite side of the system. In a sweep, Eq. (27), Eq. (29), and Eq. (30) are solved along an angle in the quadrature set, where $\psi_{i_{exit},g,m}$ becomes $\psi_{i+1_{inc},g,m}$ when sweeping from left-to-right or $\psi_{i-1_{inc},g,m}$ when sweeping from right-to-left.

The next section gives a description of the iterative procedure in which equations Eq. (27), Eq. (29), and Eq. (30) are evaluated to solve Eq. (25), obtaining a k-eigenvalue and scalar flux solution for the system.

2.6 Richardson and Power Iteration

Eq. (21) is numerically solved using a nested iterative process. A group scalar flux solution to Eq. (25) is determined through Richardson (or source) iteration, giving the inner iteration of the nested iterative process. Power iteration is used in the outer iteration to determine an improved k-eigenvalue estimate in Eq. (21) from each improved estimate of the group scalar flux. Eq. (21) is rewritten to include the inner and outer iteration indices, and the spatial zone index below,

$$\mu_m \frac{\partial \psi_{i,g,m}^{(l+1,n)}}{\partial x} + \sigma_{i,g} \psi_{i,g,m}^{(l+1,n)} = \frac{1}{2} \sum_{g'=1}^g \sigma_{s,i,g' \rightarrow g} \phi_{i,g'}^{(l,n)} + \frac{\chi_g}{2k^{(n)}} \sum_{g'=1}^G \nu_{g'} \sigma_{f,i,g'} \phi_{i,g'}^{(n)}, \quad (33)$$

where, (i) is the spatial zone, (l) is the inner iteration index and (n) is the outer iteration index. A description of the Richardson iteration solution procedure for each $\phi_{i,g'}^{(l,n)}(x)$ and the power iteration procedure for each $k^{(n)}$ of Eq. (33) is given below.

Consider a simple system of equations written in matrix notation,

$$\underline{\underline{\mathbf{A}}}\underline{\underline{\psi}} = \underline{\underline{q}} \quad (34)$$

where $\underline{\underline{\mathbf{A}}}$ is an invertible matrix acting on some vector $\underline{\underline{\psi}}$ resulting in some other vector $\underline{\underline{q}}$. In order to obtain a solution for $\underline{\underline{\psi}}$, it is common to split the operator ($\underline{\underline{\mathbf{A}}} = \underline{\underline{\mathbf{L}}} - \underline{\underline{\mathbf{S}}}$) to obtain the iterative equation [Ada 04],

$$\underline{\underline{\psi}}^{(l+1)} = \underline{\underline{\mathbf{L}}}^{-1} \underline{\underline{\mathbf{S}}}\underline{\underline{\psi}}^{(l)} + \underline{\underline{\mathbf{L}}}^{-1} \underline{\underline{q}}. \quad (35)$$

The iteration is performed by the repetitive evaluation of Eq. (35) with a trial vector $\underline{\psi}^{(l)}$ to obtain the new vector $\underline{\psi}^{(l+1)}$. When the splitting is done such that ($\underline{\mathbf{L}} = \underline{\mathbf{I}}$) and ($\underline{\mathbf{S}} = \underline{\mathbf{I}} - \underline{\mathbf{A}}$), this is known as Richardson iteration. Richardson iteration is known to be unconditionally stable for the discretized Boltzmann transport equation in planar geometry if $c < 1$, where,

$$c = \frac{\sigma_{i,s,g \rightarrow g}}{\sigma_{i,g}}, \quad (36)$$

and converges very slowly when ($c \approx 1$). It can be shown that the slowest converging modes are relatively flat spatially and nearly isotropic in angle [Ada 04]. This nice feature makes the diffusion equation a good choice of preconditioner for this system of equations for faster convergence in the limit of ($c \approx 1$). This is further explored in the discussion of diffusion synthetic acceleration in the following subsection, 2.6.1 .

Now consider the simple system of equations written in matrix notation,

$$\underline{\mathbf{A}}\underline{\phi} = \lambda\underline{\mathbf{F}}\underline{\phi} \quad (37)$$

where $\underline{\mathbf{A}}$ is again an invertible matrix, λ is an eigenvalue with a corresponding eigenvector $\underline{\phi}$, and $\underline{\mathbf{F}}$ some other “source” matrix. An iterative equation for this eigenvalue problem can be written as [Hof 01],

$$\underline{\mathbf{A}}\underline{\phi}^{(n)} = \hat{\underline{\phi}}^{(n+1)} = \lambda^{(n+1)}\underline{\mathbf{F}}\underline{\phi}^{(n+1)}. \quad (38)$$

Power iteration is performed by the repetitive evaluation of Eq. (38) with a trial eigenvector $\underline{\phi}^{(n)}$ to obtain $\hat{\underline{\phi}}^{(n+1)}$ until convergence. The eigenvector $\underline{\phi}^{(n)}$ is scaled at each iteration to give $\hat{\underline{\phi}}^{(n+1)}$, such that the scaling factor approaches the largest eigenvalue λ . Power iteration will converge to the largest eigenvalue and corresponding eigenvector, if the largest eigenvalue is distinct and the eigenvalues are

independent. It can be shown that the vector $\underline{\phi}^{(n)} \rightarrow \infty$ for $\lambda^{(n)} > 1$, and $\underline{\phi}^{(n)} \rightarrow 0$ for $\lambda^{(n)} < 1$, as $n \rightarrow \infty$, unless the vector is normalized after each power iteration [Hof 01].

When performing power iteration to obtain a new estimate of the eigenvalue in Eq. (33), the scaling is the ratio of the integrated fission sources from successive outer iterations. Recalling the definition of the fission source from Eq. (23), the scaling to determine the new estimate of the eigenvalue k is given by,

$$k^{(n+1)} = k^{(n)} \frac{\int_0^X dx' F^{(n+1)}(x')}{\int_0^X dx' F^{(n)}(x')}, \quad (39)$$

where, (X) is the planar system length. After the latest estimate of the eigenvalue $k^{(n+1)}$ has been evaluated, the fission source is normalized such that:

$$\int_0^X dx' F^{(n)}(x') = 1, \quad (40)$$

which reduces Eq. (39) to

$$k^{(n+1)} = k^{(n)} \int_0^X dx' F^{(n+1)}(x'). \quad (41)$$

Figure 1 is a flow chart of the nested iteration algorithm used to determine the largest eigenvalue ($\lambda = \frac{1}{k}$) and corresponding eigenvector ($\underline{\phi}$) of Eq. (33).

When the system is dominated by the scattering interaction with the background medium in any group, the problem can become intractable due to the large computational expense it may take to converge the inner iterations. The next section contains a discussion and derivation of the diffusion synthetic acceleration equations for Eq. (35), improving the convergence rate of the inner Richardson iteration for diffusive systems.

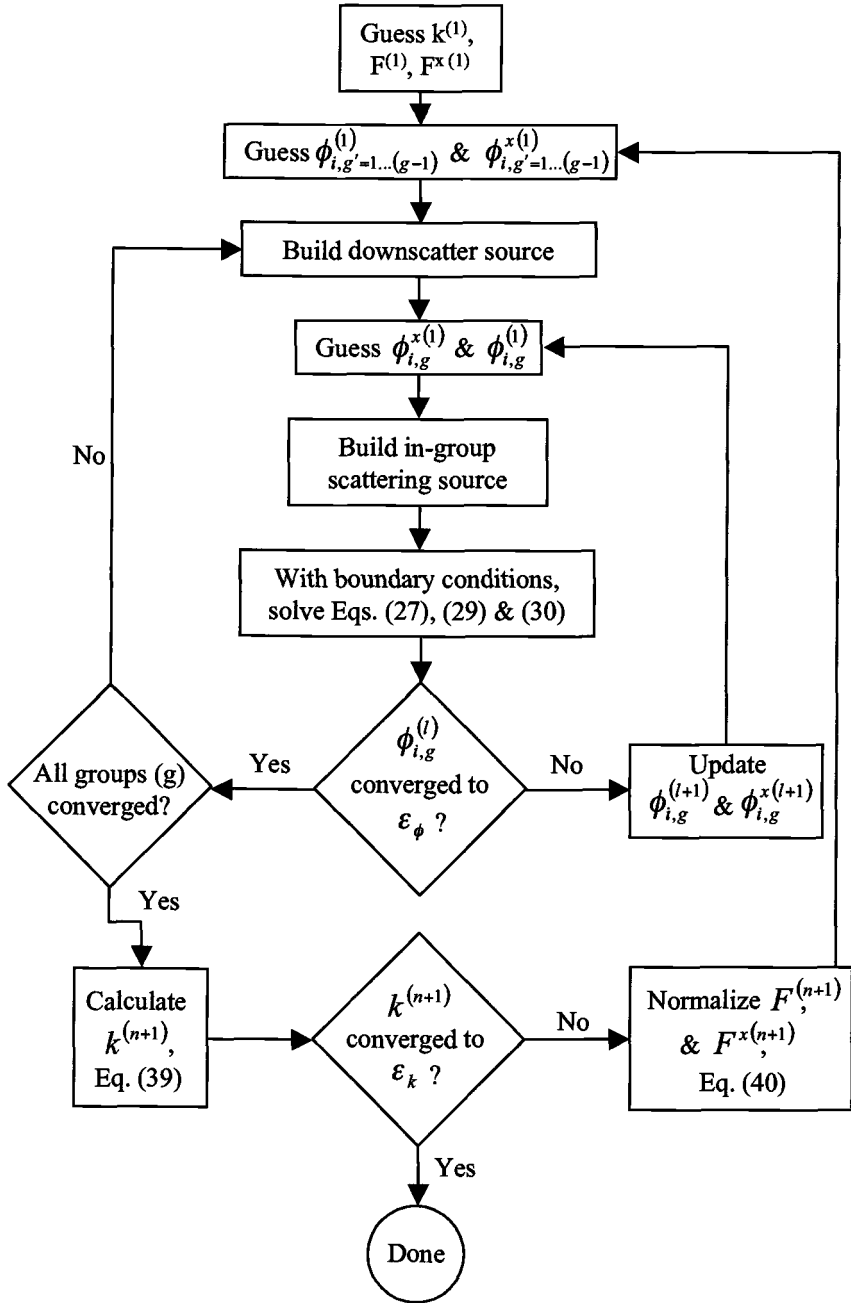


Figure 1: Flow Chart of Inner and Outer Transport Iterations

2.6.1 Diffusion Synthetic Acceleration

Richardson iteration is unconditionally stable and convergent when particle interaction with the background material is not dominated by scattering (when c of Eq. (36) is < 1). The number of Richardson iterations needed in order to converge to a solution increases drastically as $c \rightarrow 1$. When considering moderate to highly scattering systems, accelerating the inner Richardson iterations for each group scalar flux is necessary. As briefly discussed in Section 2.6, the diffusion equation makes a good choice of preconditioner for the inner iterations (Eq. (33)) because the slowest converging modes are relatively flat spatially and nearly isotropic in angle [Ada 04]. Diffusion synthetic acceleration (DSA) has been used widely in the nuclear engineering community with great success.

A procedure for the derivation of the DSA equations for a discontinuous finite element spatial discretization is given in [Ada 92]. These DSA equations can be used to accelerate Richardson iterations with a linear characteristics spatial discretization since both the linear characteristics and linear discontinuous finite element spatial discretization schemes have the same diffusion limit [Ada 98]. Using these DSA equations to precondition the Richardson iteration vastly reduces the number of iterations and will yield the same solution as in the unaccelerated case.

Eq. (33) written with a spatially discretized fission source (as given in Eq. (23)), and quadrature integration for the scalar flux is,

$$\mu_m \frac{\partial \psi_{i,g,m}^{(l+1/2,n)}}{\partial x} + \sigma_{i,g} \psi_{i,g,m}^{(l+1/2,n)} = \frac{1}{2} \sum_{g'=1}^g \sigma_{s,i,g' \rightarrow g} \sum_{m=1}^N w_m \psi_{i,g',m}^{(l,n)} + \frac{\chi_g}{2k^{(n)}} F_i^{(n)}, \quad (42)$$

where $(\chi_g/2k^{(n)}) F_i^{(n)}$ does not change with each inner iteration (l), as it is updated as part of the outer iteration, given by index (n). In this study only downscatter is

considered, and the inner iteration over each energy group always starts with the highest energy group (group 1) and continues to lower energy groups. If $\Psi_{i,g,m}^{(n)}$ is defined to be the converged discrete angular flux, the first term on the right-hand side of Eq. (42) can be written in terms of the in-group scatter and downscatter component,

$$\frac{1}{2} \sum_{g'=1}^g \sigma_{s,i,g' \rightarrow g} \sum_{m=1}^N w_m \psi_{i,g',m}^{(l,n)} = \frac{1}{2} \sum_{g'=1}^{g-1} \sigma_{s,i,g' \rightarrow g} \sum_{m=1}^N w_m \Psi_{i,g',m}^{(n)} + \frac{1}{2} \sigma_{s,i,g \rightarrow g} \sum_{m=1}^N w_m \psi_{i,g,m}^{(l,n)}, \quad (43)$$

and Eq. (42) becomes,

$$\mu_m \frac{\partial \psi_{i,g,m}^{(l+1/2,n)}}{\partial x} + \sigma_{i,g} \psi_{i,g,m}^{(l+1/2,n)} = \frac{1}{2} \sum_{g'=1}^{g-1} \sigma_{s,i,g' \rightarrow g} \sum_{m=1}^N w_m \Psi_{i,g',m}^{(n)} + \frac{1}{2} \sigma_{s,i,g \rightarrow g} \sum_{m=1}^N w_m \psi_{i,g,m}^{(l,n)} + \frac{\chi_g}{2k^{(n)}} F_i^{(n)}, \quad (44)$$

Another discretized transport equation may be written for the converged scalar flux with the same notation for the in-group scatter and downscatter terms given in Eq. (43),

$$\mu_m \frac{\partial \Psi_{i,g,m}^{(n)}}{\partial x} + \sigma_{i,g} \Psi_{i,g,m}^{(n)} = \frac{1}{2} \sum_{g'=1}^{g-1} \sigma_{s,i,g' \rightarrow g} \sum_{m=1}^N w_m \Psi_{i,g',m}^{(n)} + \frac{1}{2} \sigma_{s,i,g \rightarrow g} \sum_{m=1}^N w_m \Psi_{i,g,m}^{(n)} + \frac{\chi_g}{2k^{(n)}} F_i^{(n)}. \quad (45)$$

Subtracting Eq. (44) from Eq. (45) gives an equation for the inner iteration error

(dropping the outer iteration index (n):

$$\mu_m \frac{\partial f_{i,g,m}^{(l+1/2)}}{\partial x} + \sigma_{i,g} f_{i,g,m}^{(l+1/2)} = \frac{1}{2} \sigma_{s,i,g \rightarrow g} \sum_{m=1}^N w_m \Psi_{i,g,m} - \sigma_{s,i,g \rightarrow g} \sum_{m=1}^N w_m \psi_{i,g,m}^{(l)}, \quad (46)$$

where,

$$f_{i,g,m}^{(l+1/2)} = \Psi_{i,g,m} - \psi_{i,g,m}^{(l+1/2)}. \quad (47)$$

Substituting Eq. (47) for $\Psi_{i,g,m}$ into Eq. (46) gives,

$$\begin{aligned} \mu_m \frac{\partial f_{i,g,m}^{(l+1/2)}}{\partial x} + \sigma_{i,g} f_{i,g,m}^{(l+1/2)} - \frac{1}{2} \sigma_{s,i,g \rightarrow g} \sum_{m=1}^N w_m f_{i,g,m}^{(l+1/2)} = \\ \frac{1}{2} \sigma_{s,i,g \rightarrow g} \left(\sum_{m=1}^N w_m \psi_{i,g,m}^{(l+1/2)} - \sum_{m=1}^N w_m \psi_{i,g,m}^{(l)} \right). \end{aligned} \quad (48)$$

The scalar flux, ϕ , is defined as the integral of ψ over angle, so Eq. (48) can be rewritten as,

$$\begin{aligned} \mu_m \frac{\partial f_{i,g,m}^{(l+1/2)}}{\partial x} + \sigma_{i,g} f_{i,g,m}^{(l+1/2)} - \frac{1}{2} \sigma_{s,i,g \rightarrow g} \sum_{m=1}^N w_m f_{i,g,m}^{(l+1/2)} = \\ \frac{1}{2} \sigma_{s,i,g \rightarrow g} \left(\phi_{i,g}^{(l+1/2)} - \phi_{i,g}^{(l)} \right). \end{aligned} \quad (49)$$

The above equation is a transport equation for the iteration error term, f , with a source equal to the residual error term between current and previous scalar flux iterates. Eq. (49) will be spatially discretized according to the discontinuous finite element scheme [Ada 92]. Instead of slope-average notation, the two spatial unknowns per zone are written as a coupled set of left and right spatial unknowns. The zeroth spatial moments of Eq. (49) are taken by multiplying by the cardinal linear weight and basis functions [Ada 04],

$$w_{L,i} = 1; \quad b_{L,i} = \left(\frac{x_{i+1/2} - x}{\Delta x_i} \right), \quad (50a)$$

$$w_{R,i} = 1; \quad b_{R,i} = \left(\frac{x - x_{i+1/2}}{\Delta x_i} \right), \quad (50b)$$

where the range of the basis function is:

$$x_{i-1/2} < x < x_{i+1/2}, \quad (51)$$

and integrating over a spatial zone (assuming the $(l + 1/2)$ inner iteration notation unless explicitly stated otherwise), yielding,

$$\begin{aligned} \mu_m \left[\left(\frac{f_{i,g,m,L} + f_{i,g,m,R}}{2} \right) - f_{i-1/2,g,m} \right] + \sigma_{i,g} \Delta x_i \left[\frac{f_{i,g,m,L}}{3} + \frac{f_{i,g,m,R}}{6} \right] - \\ \frac{\sigma_{s,i,g \rightarrow g} \Delta x_i}{2} \left[\frac{F_{i,g,L}}{3} + \frac{F_{i,g,R}}{6} \right] = \frac{\sigma_{s,i,g \rightarrow g} \Delta x_i}{2} [R_{i,g,L}], \quad (52a) \end{aligned}$$

$$\begin{aligned} \mu_m \left[f_{i+1/2,g,m} - \left(\frac{f_{i,g,m,L} + f_{i,g,m,R}}{2} \right) \right] + \sigma_{i,g} \Delta x_i \left[\frac{f_{i,g,m,L}}{6} + \frac{f_{i,g,m,R}}{3} \right] - \\ \frac{\sigma_{s,i,g \rightarrow g} \Delta x_i}{2} \left[\frac{F_{i,g,L}}{6} + \frac{F_{i,g,R}}{3} \right] = \frac{\sigma_{s,i,g \rightarrow g} \Delta x_i}{2} [R_{i,g,R}], \quad (52b) \end{aligned}$$

where,

$$f_{i,g,m,(L,R)} = f_{i,g,m,(L,R)}^{(l+1/2)}, \quad (53a)$$

$$F_{i,g,(L,R)} = \sum_{m=1}^N w_m f_{i,g,m,(L,R)}^{(l+1/2)}, \quad (53b)$$

and,

$$R_{i,g,L} = \left[\left(\frac{\phi_{i,g,L}^{(l+1/2)}}{3} + \frac{\phi_{i,g,R}^{(l+1/2)}}{6} \right) - \left(\frac{\phi_{i,g,L}^{(l)}}{3} + \frac{\phi_{i,g,R}^{(l)}}{6} \right) \right], \quad (53c)$$

$$R_{i,g,R} = \left[\left(\frac{\phi_{i,g,L}^{(l+1/2)}}{6} + \frac{\phi_{i,g,R}^{(l+1/2)}}{3} \right) - \left(\frac{\phi_{i,g,L}^{(l)}}{6} + \frac{\phi_{i,g,R}^{(l)}}{3} \right) \right]. \quad (53d)$$

The closure for the linear discontinuous finite element spatial discretization is given as,

$$f_{i+1/2,g,m}^{(l+1/2)} = \begin{cases} f_{i,g,m,R}^{(l+1/2)}, & \mu > 0 \\ f_{i+1,g,m,L}^{(l+1/2)}, & \mu < 0 \end{cases}, \quad (54a)$$

$$f_{i-1/2,g,m}^{(l+1/2)} = \begin{cases} f_{i-1,g,m,R}^{(l+1/2)}, & \mu > 0 \\ f_{i,g,m,L}^{(l+1/2)}, & \mu < 0 \end{cases}. \quad (54b)$$

Redefining the error terms as a two-term Legendre polynomial expansions in angle,

$$f_{i\pm 1/2,g,m}^{(l+1/2)} \approx \frac{1}{2}F_{i\pm 1/2,g}^{(l+1/2)} + \frac{3}{2}\mu_m J_{i\pm 1/2,g}^{(l+1/2)} \quad (55)$$

where,

$$J_{i\pm 1/2,g}^{(l+1/2)} = \sum_{m=1}^N \mu_m w_m f_{i\pm 1/2,g,m}^{(l+1/2)}, \quad (56)$$

the DSA equations can now be derived.

Inserting Eq. (55) into Eqs. (52) and taking the zeroth angular moment yields,

$$\left[\left(\frac{J_{i,g,L} + J_{i,g,R}}{2} \right) - J_{i-1/2,g} \right] + \sigma_{i,g} \Delta x_i \left[\frac{F_{i,g,L}}{3} + \frac{F_{i,g,R}}{6} \right] - \sigma_{s,i,g \rightarrow g} \Delta x_i \left[\frac{F_{i,g,L}}{3} + \frac{F_{i,g,R}}{6} \right] = \sigma_{s,i,g \rightarrow g} \Delta x_i [R_{i,L}], \quad (57a)$$

$$\left[J_{i+1/2,g} - \left(\frac{J_{i,g,L} + J_{i,g,R}}{2} \right) \right] + \sigma_{i,g} \Delta x_i \left[\frac{F_{i,g,L}}{6} + \frac{F_{i,g,R}}{3} \right] - \sigma_{s,i,g \rightarrow g} \Delta x_i \left[\frac{F_{i,g,L}}{6} + \frac{F_{i,g,R}}{3} \right] = \sigma_{s,i,g \rightarrow g} \Delta x_i [R_{i,R}]. \quad (57b)$$

Defining the removal cross section as,

$$\sigma_{r,i,g} = \sigma_{i,g} - \sigma_{s,i,g \rightarrow g} \quad (58)$$

Eqs. (57) can be rewritten as,

$$\left[\left(\frac{J_{i,g,L} + J_{i,g,R}}{2} \right) - J_{i-1/2,g} \right] + \sigma_{r,i,g} \Delta x_i \left[\frac{F_{i,g,L}}{3} + \frac{F_{i,g,R}}{6} \right] = \sigma_{s,i,g \rightarrow g} \Delta x_i [R_{i,L}], \quad (59a)$$

$$\left[J_{i+1/2,g} - \left(\frac{J_{i,g,L} + J_{i,g,R}}{2} \right) \right] + \sigma_{r,i,g} \Delta x_i \left[\frac{F_{i,g,L}}{6} + \frac{F_{i,g,R}}{3} \right] = \sigma_{s,i,g \rightarrow g} \Delta x_i [R_{i,R}]. \quad (59b)$$

Inserting Eq. (55) into Eqs. (52) and taking the first angular moment gives,

$$\frac{1}{3} \left[\left(\frac{F_{i,g}^L + F_{i,g}^R}{2} \right) - F_{i-1/2,g} \right] + \sigma_{i,g} \Delta x_i \left[\frac{J_{i,g}^L}{3} + \frac{J_{i,g}^R}{6} \right] = 0, \quad (60a)$$

$$\frac{1}{3} \left[F_{i+1/2,g} - \left(\frac{F_{i,g}^L + F_{i,g}^R}{2} \right) \right] + \sigma_{i,g} \Delta x_i \left[\frac{J_{i,g}^L}{6} + \frac{J_{i,g}^R}{3} \right] = 0. \quad (60b)$$

Replacing the zeroth moment of the correction term at the cell edges in Eqs. (60) with the nearest within-cell zeroth moment of the correction,

$$F_{i-1/2,g} = F_{i,g,L}, \quad (61a)$$

$$F_{i+1/2,g} = F_{i,g,R}, \quad (61b)$$

yields two Fick's Law equations,

$$J_{i,g,L} = \frac{1}{3\sigma_{i,g}\Delta x_i} [F_{i,g,L} - F_{i,g,R}], \quad (62a)$$

$$J_{i,g,R} = \frac{1}{3\sigma_{i,g}\Delta x_i} [F_{i,g,L} - F_{i,g,R}]. \quad (62b)$$

Finally, inserting Eq. (55) into Eq. (54) and taking the first angular moment yields,

$$J_{i+1/2,g} = \frac{1}{4} F_{i,g}^R - \frac{1}{4} F_{i+1,g}^L + \frac{1}{2} J_{i+1,g}^L + \frac{1}{2} J_{i,g}^R, \quad (63a)$$

$$J_{i-1/2,g} = \frac{1}{4} F_{i-1,g}^R - \frac{1}{4} F_{i,g}^L + \frac{1}{2} J_{i,g}^L + \frac{1}{2} J_{i-1,g}^R. \quad (63b)$$

The combination of Eqs. (59), Eqs. (62), and Eqs. (63) yields the DSA equations,

$$[D_{i-1,g}] F_{i-1,g,L} + [C_{i-1,g}] F_{i-1,g,R} + [A_{i,g}] F_{i,g,L} + [B_{i,g}] F_{i,g,R} = \sigma_{s,i,g \rightarrow g} \Delta x_i [R_{i,L}] , \quad (64a)$$

$$[B_{i,g}] F_{i,g,L} + [A_{i,g}] F_{i,g,R} + [C_{i+1,g}] F_{i+1,g,L} + [D_{i+1,g}] F_{i+1,g,R} = \sigma_{s,i,g \rightarrow g} \Delta x_i [R_{i,R}] , \quad (64b)$$

where,

$$A_{i,g} = \left[\frac{1}{6\sigma_{i,g}\Delta x_i} + \frac{1}{4} + \frac{\sigma_{r,i,g}\Delta x_i}{3} \right] , \quad (65a)$$

$$B_{i,g} = \left[\frac{\sigma_{r,i,g}\Delta x_i}{6} - \frac{1}{6\sigma_{i,g}\Delta x_i} \right] , \quad (65b)$$

$$C_{i,g} = \left[\frac{1}{6\sigma_{i,g}\Delta x_i} - \frac{1}{4} \right] , \quad (65c)$$

$$D_{i,g} = \left[-\frac{1}{6\sigma_{i,g}\Delta x_i} \right] . \quad (65d)$$

When solved these equations yield the correction terms to the scalar fluxes at the current iteration level in left-right notation ($F_{i,g,L}$ and $F_{i,g,R}$). These corrections are then translated into slope-average notation so that they can be added to $\phi_{i,g}^{(l+1/2)}$ and $\phi_{i,g}^{x(l+1/2)}$ in each cell. This translation takes the form:

$$F_{i,g} = \frac{1}{2} [F_{i,g,L} + F_{i,g,R}] , \quad (66a)$$

$$F_{i,g}^x = \frac{1}{2} [F_{i,g,R} - F_{i,g,L}] , \quad (66b)$$

and, redefining the left and right residual terms of Eq. (53c) and Eq. (53d) in terms of slope-average scalar fluxes,

$$R_{i,L} = \left[\left(\frac{\phi_{i,g}^{(l+1/2)} - \phi_{i,g}^{x(l+1/2)}}{3} + \frac{\phi_{i,g}^{(l+1/2)} + \phi_{i,g}^{x(l+1/2)}}{6} \right) - \left(\frac{\phi_{i,g}^{(l)} - \phi_{i,g}^{x(l)}}{3} + \frac{\phi_{i,g}^{(l)} + \phi_{i,g}^{x(l)}}{6} \right) \right], \quad (66c)$$

$$R_{i,R} = \left[\left(\frac{\phi_{i,g}^{(l+1/2)} - \phi_{i,g}^{x(l+1/2)}}{6} + \frac{\phi_{i,g}^{(l+1/2)} + \phi_{i,g}^{x(l+1/2)}}{3} \right) - \left(\frac{\phi_{i,g}^{(l)} - \phi_{i,g}^{x(l)}}{6} + \frac{\phi_{i,g}^{(l)} + \phi_{i,g}^{x(l)}}{3} \right) \right]. \quad (66d)$$

The group correction terms are then added to the group scalar flux slope and average for each spatial zone:

$$\phi_{i,g}^{(l)} = \phi_{i,g'}^{(l+1/2)} + F_{i,g}^{(l+1/2)}, \quad (67a)$$

$$\phi_{i,g}^{x(l)} = \phi_{i,g'}^{x(l+1/2)} + F_{i,g}^{x(l+1/2)}. \quad (67b)$$

2.6.2 Accelerated Reflecting Boundary Conditions

If vacuum boundary conditions (Eqs. (31)) are used on both edges of the system, no additional acceleration is needed. However, if specular reflection boundary conditions (Eqs. (32)) are used, then a guess is needed for the incident angular flux on one edge of the slab. This guess has to be accelerated or the effectiveness of the preconditioner is greatly reduced or can cause the iterative solution to diverge [Yav 88].

In the case of unaccelerated Richardson iteration, a guess is used for the incident angular flux on the edges of the system on the first iteration in order to perform a

single sweep,

$$\psi_{1_{inc},g,m}^{(1)} = \psi_{1/2,g,m}^{(1)} = 0, \quad \mu_m > 0, \quad (68a)$$

$$\psi_{I_{inc},g,m}^{(1)} = \psi_{I+1/2,g,m}^{(1)} = 0, \quad \mu_m < 0, \quad (68b)$$

given (I) spatial zones. After the sweep is performed in each direction, the exiting flux on each system edge is reflected according to Eqs. (32). This is repeated until convergence, but convergence can be prohibitively slow for diffusive systems.

In the accelerated case, an initial guess is made for the incident flux on the left edge:

$$\psi_{1/2,g,m}^{(1)} = g_m^{(1)} = 0, \quad \mu_m > 0. \quad (69)$$

A left-to-right transport sweep yields the exiting angular flux on the right edge of the system:

$$\psi_{I+1/2,g,m}^{(l+1/2)}, \quad \mu_m > 0. \quad (70)$$

This exiting flux is reflected back in according to Eq. (32b). A right-to-left transport sweep yields the outgoing angular flux on the left edge of the system:

$$\psi_{1/2,g,m}^{(l+1/2)}, \quad \mu_m < 0. \quad (71)$$

In Richardson iteration, this outgoing flux would be reflected back into the slab using Eq. (32a):

$$g_n^{(l+1/2)} = \psi_{1/2,g,m}^{(l+1/2)}, \quad \mu_n < 0; \quad (72a)$$

$$\mu_n = -\mu_m \quad (72b)$$

Information from the DSA equations can be used to generate a more accurate estimate of $g^{(l+1/2)}$, thereby accelerating the reflecting boundary conditions. This is done after a slight modification to Eqs. (59) in the first and last zone of the

system. For the left edge of the system, Eq. (59a) becomes,

$$\left[\left(\frac{J_{1,g,L} + J_{1,g,R}}{2} \right) \right] + \sigma_{r,1,g} \Delta x_1 \left[\frac{F_{1,g,L}}{3} + \frac{F_{1,g,R}}{6} \right] = \sigma_{s,1,g \rightarrow g} \Delta x_1 [R_{1,L}] + J_{1/2,g}. \quad (73)$$

Recalling the definition of the current from Eq. (15), the correction term for the net current on the left edge is known exactly as,

$$J_{1/2,g} = 0 - \sum_{m=1}^N \mu_m w_m \psi_{1/2,g,m}^{(l+1/2)}, \quad (74)$$

since it is known that the net current on the system boundaries must converge to zero. This changes the terms in the first row of the matrix given in Eq. (65a) and Eq. (65b) to,

$$A_{1,g}^* = \left[\frac{1}{3\sigma_{1,g}\Delta x_1} + \frac{\sigma_{r,1,g}\Delta x_1}{3} \right], \quad (75a)$$

$$B_{1,g}^* = \left[\frac{\sigma_{r,1,g}\Delta x_1}{6} - \frac{1}{3\sigma_{1,g}\Delta x_1} \right], \quad (75b)$$

At the right system edge, Eq. (59b) becomes,

$$\left[\left(\frac{J_{I,g,L} + J_{I,g,R}}{2} \right) \right] + \sigma_{r,I,g} \Delta x_I \left[\frac{F_{I,g,L}}{6} + \frac{F_{I,g,R}}{3} \right] = \sigma_{s,I,g \rightarrow g} \Delta x_I [R_{I,R}]. \quad (76)$$

The correction term $J_{I+1/2,g}$ of Eq. (59b) is exactly zero on this side since perfect reflection of the exiting angular flux is done at the beginning of each right-to-left sweep. The terms in the last row of the matrix given in Eq. (65a) and Eq. (65b) become,

$$A_{I,g}^{**} = \left[\frac{1}{3\sigma_{I,g}\Delta x_I} + \frac{\sigma_{r,I,g}\Delta x_I}{6} \right], \quad (77a)$$

$$B_{I,g}^{**} = \left[\frac{\sigma_{r,I,g}\Delta x_I}{3} - \frac{1}{3\sigma_{I,g}\Delta x_I} \right], \quad (77b)$$

After the correction terms are computed and added to the group scalar flux slope and average, $\phi_{i,g}^{(l+1/2)}$ and $\phi_{i,g}^{x(l+1/2)}$, the incident angular flux on the left edge is computed by:

$$g_n^{(l+1/2)} = \psi_{1/2,g,m}^{(l+1/2)} + \frac{1}{2}F_{1,g,L} + \frac{3}{2}\mu_n \sum_{m=1}^N \mu_m w_m \psi_{1/2,g,m}, \quad (78a)$$

$$\mu_n = -\mu_m, \quad \mu_m < 0. \quad (78b)$$

This method of acceleration for the boundary conditions allows the same rapid rate of convergence that is realized implementing DSA with vacuum boundaries on both system edges.

For (I) total spatial zones in the problem, Eqs. (64) will form a $(2I) \times (2I)$ pentadiagonal matrix and Eq. (66c) and Eq. (66d) form the $(2I)$ source vector. The computational cost of constructing this matrix and vector, and subsequent cost of solution for the correction terms by a banded solver, is insignificant compared to the overall speed-up for highly diffusive systems. The overall computational cost is also reduced for systems dominated by absorption, but by a smaller factor.

2.7 Summary

In this chapter the analytic Boltzmann transport equation for a general geometry eigenvalue problem has been introduced. An example of the specific eigenvalue problem of interest was given to clarify the scope of this thesis. Simplifying assumptions were made to reduce the phase space to steady-state, planar geometry transport. A discretized form of this analytic transport equation was derived which is amenable to numerical solution techniques. The discretization schemes employed were S_N in angle, multigroup in energy, and linear characteristics in space. The nested iterative procedure for solving the discretized eigenvalue problem was then

outlined. Since systems which may be highly diffusive are of interest but are computationally inefficient with Richardson iteration alone, diffusion synthetic acceleration was derived. This system of acceleration equations was derived for the linear discontinuous spatial discretization, and altered to accelerate the system of equations for the linear characteristic discretization. The above deterministic calculation procedure is integrated into an algorithm for performing radiation transport benchmark calculations in a stochastic background medium in the following chapter.

3 NEUTRON TRANSPORT IN STOCHASTIC MEDIA

3.1 Introduction

This chapter provides a description of the algorithm which implements the preconditioned, discretized transport equations discussed in the previous chapter for a binary stochastic medium. The choice of cross section data and statistical distributions are given and the physical basis for these choices is discussed. Finally, the sets of calculations performed are provided.

3.2 Modeling Stochastic Background Media

The transport equation can be deterministically solved with great accuracy using the solution method discussed in Chapter 2 for a fixed, heterogeneous medium. This method is integrated into an algorithm for generating transport solutions for a binary stochastic medium. Statistical distributions describe the material mixing. Since the precise location of any of the components is known only in this statistical sense, the mixing statistics are sampled to populate the spatial domain of the system. Once the system has been defined, a transport calculation is then performed for the single fixed medium realization of the mixing statistics. If the mixing statistics are well sampled, an ensemble transport solution with an acceptable statistical error can be computed.

Since planar geometry is considered for this study, populating the system is a simple task. The statistical distributions which govern the segment lengths of each material and their mean lengths are known (assumed, calculated, or measured). The mixing statistics are assumed to be homogeneous, meaning that they are not

a function of space, only a function of which material is considered. Mean segment lengths for the two materials (0 or 1) are given as,

$$\lambda_\alpha; \quad \alpha = 0, 1. \quad (79)$$

The probability of finding any given material in the system on average is then defined as a material transition probability,

$$p_\alpha = \frac{\lambda_\alpha}{\lambda_\alpha + \lambda_\beta}; \quad \alpha = 0, 1; \quad \alpha \neq \beta. \quad (80)$$

A random number generator is utilized to sample each segment length distribution, populating a system of length (X) with alternating material segments of random size from left-to-right [Ada 89]. The algorithm for constructing a single realization of the mixing statistics using random numbers (ξ) is outlined in Figure 2. After the realization is generated, the transport algorithm of Figure 1 is invoked. The mean and standard deviation are calculated for the k-eigenvalue and group scalar flux. The group scalar flux and k-eigenvalue from each realization contribute to an ensemble average group scalar flux and k-eigenvalue over the total number of realizations (R). The mean is defined as the first statistical moment, or,

$$\bar{x} = \int_{-\infty}^{\infty} dx x f(x), \quad (81)$$

where x is a random variable and $f(x)$ is a probability distribution function with the property ($\int_{-\infty}^{\infty} f(x) = 1$) [Lew 93]. The ensemble average k-eigenvalue and group flux can be approximated with a large number of realizations,

$$\bar{\phi}_{i,g} = \frac{1}{R} \sum_{r=1}^R \phi_{i,g,r} \quad (82a)$$

$$\bar{k} = \frac{1}{R} \sum_{r=1}^R k_r \quad (82b)$$

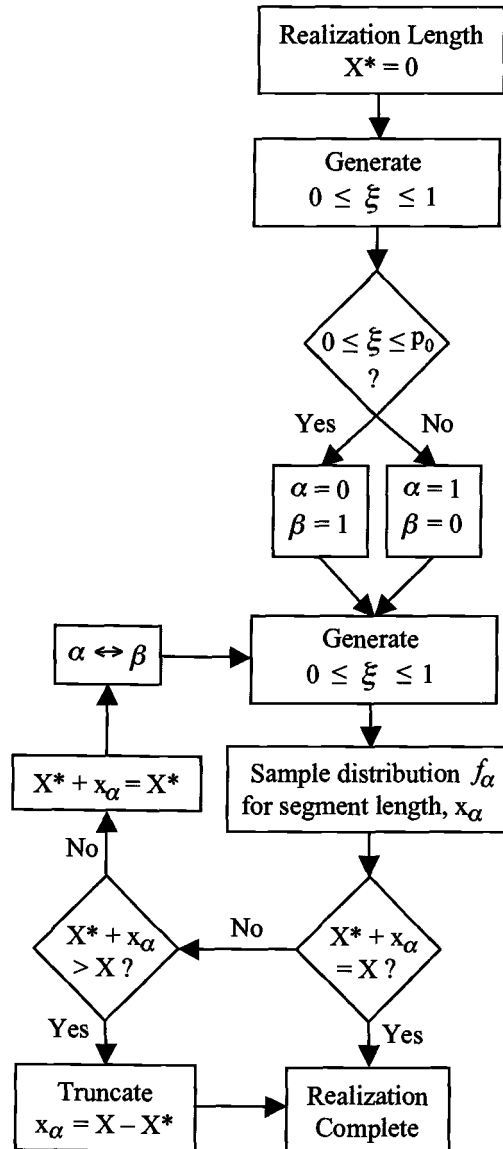


Figure 2: Flow Chart of Realization Construction

Standard deviation is related to the square-root of the second statistical moment about the mean:

$$\bar{x}^2 = \int_{-\infty}^{\infty} dx x^2 f(x), \quad (83a)$$

$$\sigma(x) = \sqrt{\bar{x}^2 - \bar{x}^2}. \quad (83b)$$

The standard deviation of the ensemble average k-eigenvalue and group fluxes can also be approximated with a large number of realizations,

$$\sigma_{\phi_{i,g}} = \sqrt{\left(\frac{1}{R} \sum_{r=1}^R \phi_{i,g,r}^2 \right) - \bar{\phi}_{i,g}^2} \quad (84a)$$

$$\sigma_k = \sqrt{\left(\frac{1}{R} \sum_{r=1}^R k_r^2 \right) - \bar{k}^2}. \quad (84b)$$

The complete algorithm consists of three nested iteration loops, shown in Figure 3. Using preconditioned Richardson iteration in a transport calculation for any given realization, accuracy is increased with each iteration. In the case of the statistical ensemble calculations averaged over all realizations, the error decreases as $1/\sqrt{R}$ and is governed by the central limit theorem [Lew 93]. This theorem states that as $R \rightarrow \infty$ the statistical solution approaches a normal distribution, and the mean and variance of the solution will converge to their exact values. The central limit theorem is only valid in the limit of a large number of realizations. Therefore, a statistically significant minimum number of realizations is chosen before convergence is tested (R^* in Figure 3). The mean and standard deviation are compared every 10^{th} realization thereafter to determine if the solution has converged. An example of the statistical convergence of the relative error of ensemble quantities as a function of realization is given in Figure 4.

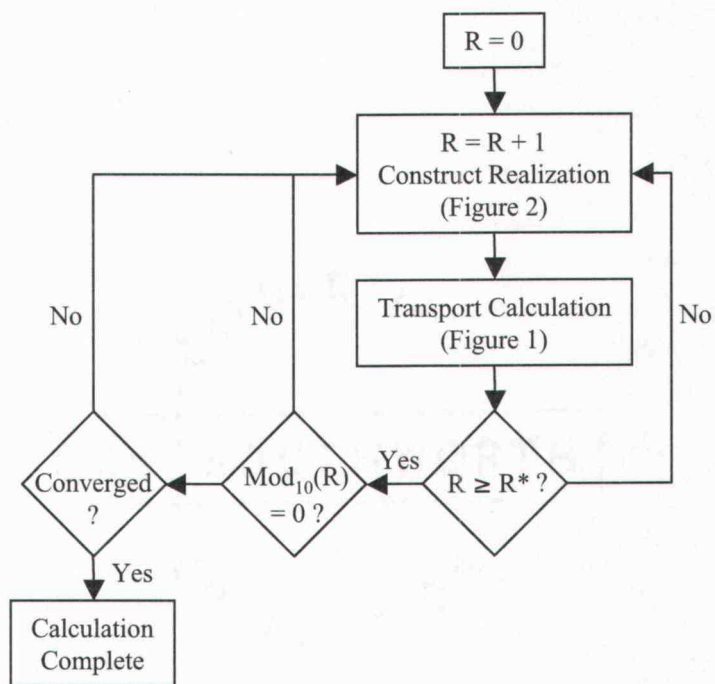


Figure 3: Flow Chart of Complete Algorithm

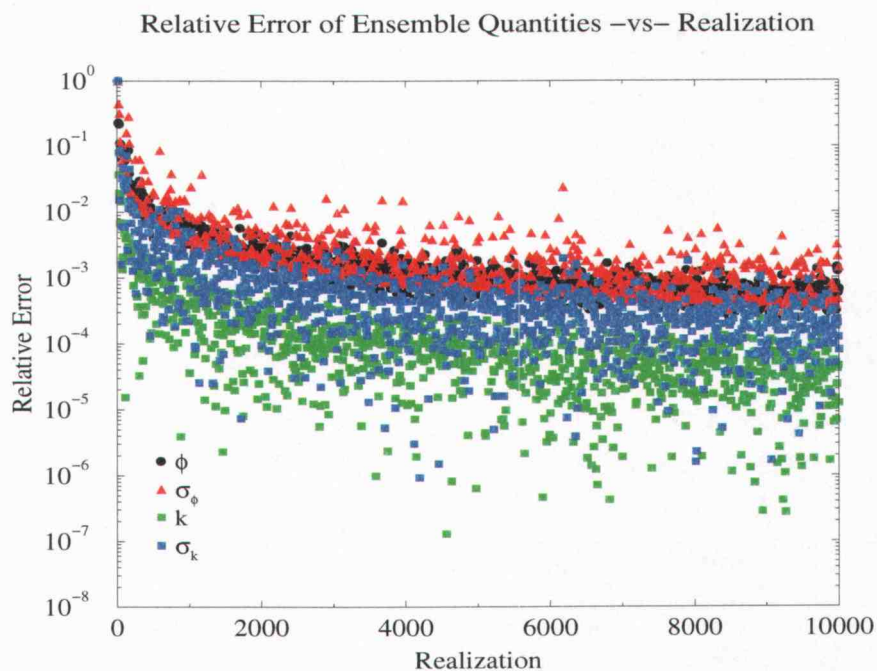


Figure 4: Relative Error of Ensemble Quantities as a Function of Realization

3.3 Mixing Statistics

The purpose of this study is to determine the effect of energy dependence on the group flux and k-eigenvalue for a binary stochastic medium. A suitable problem has to be chosen in order to illustrate this effect. Planar geometry transport is not a realistic model of a fuel assembly or a nuclear reactor. However, the data used for this study is based upon a standard 17x17 pressurized water reactor (PWR) fuel assembly so that the cross section data is physically realistic. Using this data, the effect of energy dependence is investigated in a simple stochastic transport study.

A two-dimensional axial slice of a fuel assembly can be crudely modeled as a two-material heterogeneous medium. A 1/4 fuel assembly is given in Figure 5. In this model, the fuel pins (red) exist in a fixed lattice surrounded by a water

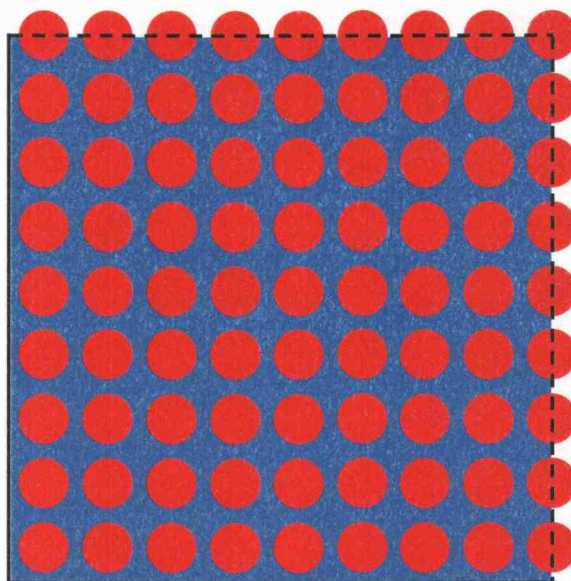


Figure 5: 1/4 Fuel Assembly

moderator (blue). The system length is taken to be the average chord length through a PWR assembly. [This is described in detail briefly.] This chord is a 1-

dimensional system populated with random segments of fuel and moderator. It is the goal of this study to model random chord lengths with random material loading as a binary stochastic medium in planar geometry. Suitable mixing statistics and system lengths must be determined to perform a transport calculation for this stochastic medium.

The system length was chosen to be the average chord length connecting two sides of a PWR fuel assembly of standard size. The standard PWR fuel assembly is a square, with a side of length 21.4 cm [Dud 76]. The average chord length through a square of this size was determined numerically. This numerical calculation involved randomly sampling a point on a side of the assembly $0 \leq \xi_s \leq 21.4$ cm and a random angle $0 \leq \xi_\theta \leq \pi$. A chord was then drawn from the point ξ_s along the angle ξ_θ to a point of intersection with another side of the assembly (Figure 6). These chord lengths were calculated and the average chord length determined from

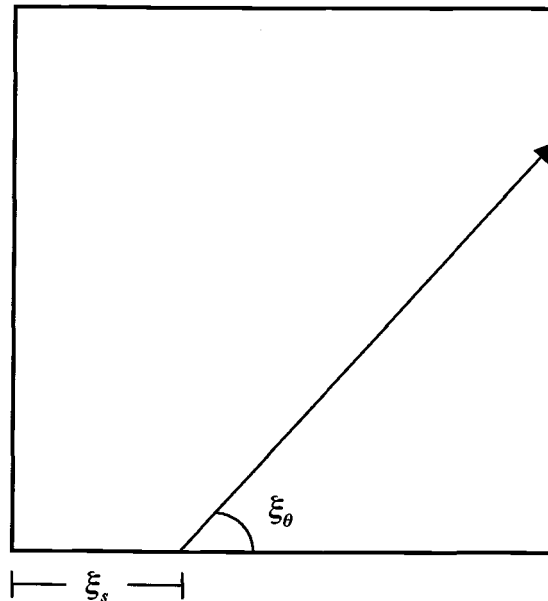


Figure 6: Generation of an Assembly Chord Length

a simulation of 10^7 random chords. The average chord length determined from this simulation is 15.206 *cm* and is taken to be the system length (X).

Different segment length distributions for each material describing the mixing statistics of this binary stochastic mixture are assumed or calculated. For historical reasons discussed in Section 1.1, segment lengths which are exponentially distributed in each material (Markovian distributions) are the first set of mixing statistics considered. This is known to be a reasonable approximation for the segment length distribution in a matrix material containing randomly distributed disks [Ols 03]. Therefore, Markovian statistics are a reasonable approximation to the segment length distribution for the moderator material. A Markovian distribution is not representative of segment lengths in disks of a fixed radius. The segment lengths in a disk range from $0 \leq x \leq 2r$ and the segment lengths in a Markovian distribution range from $0 \leq x \leq \infty$. A Markovian distribution is given by,

$$f(x) = \frac{1}{\lambda} e^{-x/\lambda}, \quad (85)$$

where $f(x)dx$ is the probability of any segment length lying between x and $x + dx$. This distribution function has the property,

$$\int_0^{\infty} dx \frac{1}{\lambda} e^{-x/\lambda} = 1. \quad (86)$$

This distribution is sampled randomly with a random number ξ , yielding a random segment length,

$$\xi = \int_0^{x_i} dx \frac{1}{\lambda} e^{-x/\lambda}, \quad (87a)$$

$$(x_i)_{Mark} = -\lambda \ln(\xi). \quad (87b)$$

The mean segment length for the Markovian distribution is,

$$\lambda_{Mark} = \int_0^{\infty} dx x \frac{1}{\lambda} e^{-x/\lambda} = \lambda. \quad (88a)$$

The standard deviation of this distribution is,

$$(\sigma_{x_i})_{Mark} = \sqrt{\left(\int_0^\infty dx x^2 \frac{1}{\lambda} e^{-x/\lambda}\right) - \lambda^2} = \lambda, \quad (88b)$$

which is large relative to the mean.

The next natural choice of mixing statistics is the Disk distribution in the fuel material and a Markovian distribution in the moderator material. The Disk distribution is given by,

$$f(x) = \frac{x}{2r\sqrt{4r^2 - x^2}}, \quad (89)$$

where r is the disk radius [Don 03a]. This is a distribution of segment lengths ranging from $0 \leq x_i \leq 2r$, such that:

$$\int_0^{2r} dx \frac{x}{2r\sqrt{4r^2 - x^2}} = 1. \quad (90)$$

This distribution is sampled randomly yielding a random segment length,

$$\xi = \int_0^{x_i} dx \frac{x}{2r\sqrt{4r^2 - x^2}}, \quad (91a)$$

$$(x_i)_{Disk} = 2r\sqrt{2\xi - \xi^2}. \quad (91b)$$

The mean segment length for the Disk distribution is,

$$\lambda_{Disk} = \int_0^{2r} dx \frac{x^2}{2r\sqrt{4r^2 - x^2}} = \frac{\pi r}{2}, \quad (92a)$$

and the standard deviation is,

$$(\sigma_{x_i})_{Disk} = \sqrt{\left(\int_0^{2r} dx \frac{x^3}{2r\sqrt{4r^2 - x^2}}\right) - \frac{\pi^2 r^2}{4}} = \frac{r\sqrt{3(32 - 3\pi^2)}}{6} \approx 0.4464 r. \quad (92b)$$

The Disk distribution is exact in the fuel material and the Markovian distribution is approximate in the moderator considering a random chord drawn through a PWR

fuel assembly. The standard deviation of the Disk distribution is considerably less than the Markovian distribution.

In the third set of statistics considered, an “exact” segment length distribution is sought for both the fuel and moderator materials. The Disk distribution is again used in the fuel material. The numerical calculation of the average chord length in a square was modified to determine the average chord length in the moderator of a 17x17 PWR fuel assembly (Figure 5). An ordered lattice of 17x17 fuel disks is placed in a square with dimensions of a common PWR fuel assembly. Again a point on a side of the assembly is randomly sampled $0 \leq \xi_s \leq 21.4 \text{ cm}$ and a random angle is sampled $0 \leq \xi_\theta \leq \pi$. A chord is then drawn from the point ξ_s along the angle ξ_θ to a point of intersection with a fuel pin or a point of intersection with an assembly side. Distances to intersections of the random chord with either fuel disks, or an assembly side are calculated and the chord length is taken to be the minimum of these distances. Again, 10^7 chords were drawn to determine both the average chord length in the moderator material and the PDF of the chord length distribution. The mean chord length of this distribution, hereafter referred to as the Matrix distribution, is,

$$\lambda_{Matrix} = 1.1531 \text{ cm}, \quad (93a)$$

and the standard deviation is,

$$(\sigma_{x_i})_{Matrix} = 1.8829 \text{ cm} \approx 1.63\lambda_{Matrix}. \quad (93b)$$

This is even a larger standard deviation about the mean chord length than in the Markovian distribution giving the expectation of a large variability of chord lengths for the Matrix distribution. The distribution of chord lengths in the moderator material is approximately exponentially distributed with peaks between each row

of pins. Figure 7 shows the PDF of chord lengths in the moderator material of the assembly.

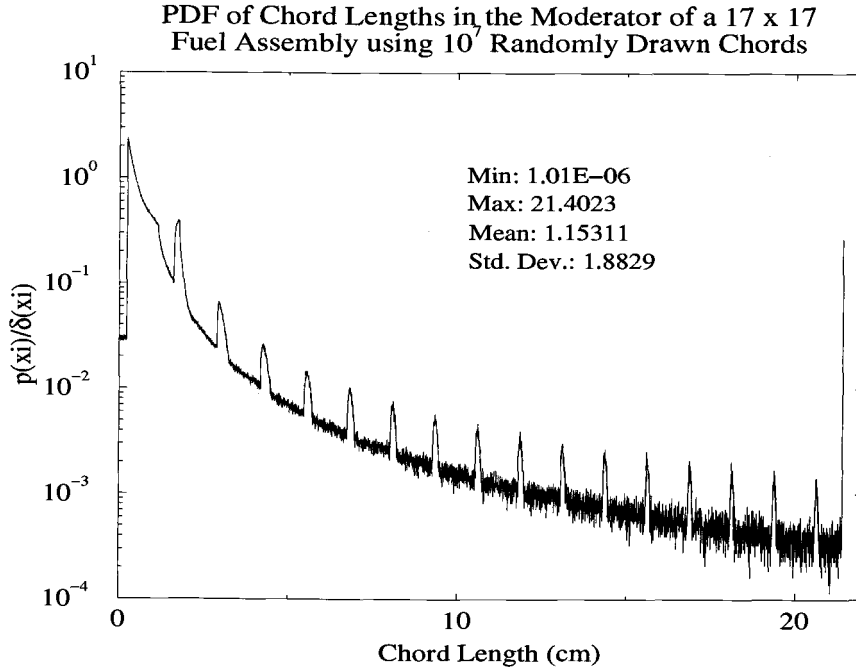


Figure 7: Distribution of Chord Length in Moderator Material of a 17x17 Fuel Assembly

The angle formed between adjacent fuel pins in a row and the random point on a side of the assembly decreases for increasing distance of the row from the random point. Therefore, these peaks become more narrow for longer chord lengths. The peak on the right-hand side of the PDF is due to those chords of a length equal to, or slightly longer than, an assembly side. These chords can exist in the small gap between an edge of the fuel lattice and an assembly boundary, or between fuel pins. The cumulative probability distribution function (numerically integrated PDF) of chord lengths of the Matrix distribution is sampled for segment lengths in the moderator material and the Disk distribution is sampled for fuel material segment lengths in the third set of mixing statistics. This is an exact distribution in the

fuel material and a better approximation to the distribution of chord lengths in the moderator material in a PWR fuel assembly.

For all three sets of statistics, the same mean chord lengths in each material are utilized. The mean chord length in the fuel material is calculated using Eq. (92a) with a radius determined from standard PWR data of 0.4749 cm [Dud 76]. This radius is slightly greater than the actual fuel pellet radius, since it includes the thickness of the gap between the pellet and clad, and the clad thickness. The mean chord length in the moderator for all simulations is given in Eq. (93a).

3.4 Cross Section Data

The two-group cross-sections for this study were based on a group collapse calculation performed with CASMO-3 for a standard PWR fuel pin with 5% enriched UO_2 [Ede 93]. The impact of variability in *each* cross section, for *each* material, and for different segment length distributions is beyond the scope of this study. Therefore, assumptions are made which are common to reactor analysis (Table 1) to narrow the range of variable parameters: no upscatter is allowed, and neutrons are only born in the fast group. The moderator cross sections are fixed, with no fast within-group scatter, and no fission. All of the variability in cross section data exists in the fuel material. Downscatter and thermal within-group scatter are not allowed in the fuel. The fission cross section and average neutron yield per fission are fixed. The fast within-group scatter and both the fast and thermal group total cross sections are variable. The fast group absorption cross section of the fuel material is fixed ($\sigma_{a,1}^{fuel} = 0.0197155 \text{ cm}^{-1}$) where, $\sigma_1^{fuel} = \sigma_{a,1}^{fuel} + \sigma_{s,1 \rightarrow 1}^{fuel}$. Only the absorption interaction is allowed in the thermal group fuel material ($\sigma_2^{fuel} = \sigma_{a,2}^{fuel}$). Therefore, if any interaction takes place in the fuel material in the thermal group,

Material: Fuel		
Cross Section (cm^{-1})	Group 1	Group 2
$\sigma_{t,g}$	$0.01972 + \sigma_{s,1 \rightarrow 1}^{fuel}$	Variable
$\sigma_{s,1 \rightarrow g}$	Variable	0.0
$\sigma_{s,2 \rightarrow g}$	0.0	0.0
$\nu_g \sigma_{f,g}$	0.0	0.564819
χ	1	0
Material: Moderator		
Cross Section (cm^{-1})	Group 1	Group 2
$\sigma_{t,g}$	0.02678	1.662
$\sigma_{s,1 \rightarrow g}$	0.0	0.02678
$\sigma_{s,2 \rightarrow g}$	0.0	1.655
$\nu_g \sigma_{f,g}$	0.0	0.0
χ	0	0

Table 1: Cross Sections by Material and Energy Group

it will be either fission or parasitic capture ($\sigma_a = \sigma_s + \sigma_c$), with a fixed average number of neutrons released per fission of $\nu = 2.4188$. The ranges of variability for these parameters are given by,

$$0 < \frac{\sigma_{s,1 \rightarrow 1}^{fuel}}{\sigma_{s,1 \rightarrow 1}^{fuel} + \sigma_{a,1}^{fuel}} = c^{fuel} < 1, \quad (94a)$$

and,

$$1 < \frac{\nu_2^{fuel} \sigma_{f,2}^{fuel}}{\sigma_{a,2}^{fuel}} = k_\infty < \nu. \quad (94b)$$

The simple atomic mix approximation of the cross sections is made by calculating a homogenized cross section based on the material transition probability of Eq. (80),

$$\langle \sigma_\ell \rangle_{i,g} = p_\alpha \sigma_{\alpha,\ell,i,g} + p_\beta \sigma_{\beta,\ell,i,g}; \quad \alpha = 0, 1; \quad \alpha \neq \beta, \quad (95)$$

where, ℓ represents any of the cross sections: scattering, fission, absorption or total. Since the atomic mix approximation considers a homogeneous medium, the computational expense of an atomic mix calculation is significantly less than in the

benchmark case. The accuracy of the atomic mix approximation for a two-group, binary stochastic medium is unknown. Atomic mix solutions will be compared with the ensemble average benchmark to determine its validity as a model.

3.5 Calculations

The calculations are grouped by boundary conditions, material segment length distribution (sets), c^{fuel} (cases) and k_{∞} (calculations). For vacuum boundaries, three values of both c^{fuel} and k_{∞} are considered. These nine calculations are repeated for each of the three sets of mixing statistics. This gives a total of 27 benchmark calculations with vacuum boundary conditions. Another 27 homogeneous medium calculations were performed employing the atomic mix approximation of the cross sections (Eq. (95)).

Using reflecting boundaries, three values of k_{∞} of Eq. (94b) were considered for the three different sets of mixing statistics. Variation of c^{fuel} was not considered since the solution will be exactly the same for any given value of k_{∞} because there is no leakage. This gives a total of nine benchmark calculations with reflecting boundary conditions. Another nine homogeneous medium calculations are performed employing the atomic mix approximation. The set of cases for each of the mixing statistics are summarized for vacuum boundaries in Tables 2 - 4 below. The sets of cases for each of the mixing statistics are summarized for reflecting boundaries in Table 5 below.

The described sampling algorithm does not preserve a specified material loading from realization to realization. Therefore, the overall behavior of the random system will not be compared to a non-random reference case. In the case of reflecting boundaries, these calculations are indicative of the possible transport solutions

Set 1: Fuel: Markov, Moderator: Markov								
Vacuum Boundaries								
Case 1			Case 2			Case 3		
Calc.	c^{fuel}	k_{∞}	Calc.	c^{fuel}	k_{∞}	Calc.	c^{fuel}	k_{∞}
1.1.1	0.1	1	1.2.1	0.5	1	1.3.1	0.9	1
1.1.2	0.1	$\nu/2$	1.2.2	0.5	$\nu/2$	1.3.2	0.9	$\nu/2$
1.1.3	0.1	ν	1.2.3	0.5	ν	1.3.3	0.9	ν

Table 2: Calculation Set 1 Variable Parameter Values, Vacuum Boundaries

Set 2: Fuel: Disk, Moderator: Markov								
Vacuum Boundaries								
Case 1			Case 2			Case 3		
Calc.	c^{fuel}	k_{∞}	Calc.	c^{fuel}	k_{∞}	Calc.	c^{fuel}	k_{∞}
2.1.1	0.1	1	2.2.1	0.5	1	2.3.1	0.9	1
2.1.2	0.1	$\nu/2$	2.2.2	0.5	$\nu/2$	2.3.2	0.9	$\nu/2$
2.1.3	0.1	ν	2.2.3	0.5	ν	2.3.3	0.9	ν

Table 3: Calculation Set 2 Variable Parameter Values, Vacuum Boundaries

Set 3: Fuel: Disk, Moderator: Matrix								
Vacuum Boundaries								
Case 1			Case 2			Case 3		
Calc.	c^{fuel}	k_{∞}	Calc.	c^{fuel}	k_{∞}	Calc.	c^{fuel}	k_{∞}
3.1.1	0.1	1	3.2.1	0.5	1	3.3.1	0.9	1
3.1.2	0.1	$\nu/2$	3.2.2	0.5	$\nu/2$	3.3.2	0.9	$\nu/2$
3.1.3	0.1	ν	3.2.3	0.5	ν	3.3.3	0.9	ν

Table 4: Calculation Set 3 Variable Parameter Values, Vacuum Boundaries

Set 1: Fuel: Markov, Moderator: Markov					
Reflecting Boundaries					
Case 1		Case 2		Case 3	
Calc.	k_∞	Calc.	k_∞	Calc.	k_∞
1.1	1	1.2	$\nu/2$	1.3	ν
Set 2: Fuel: Disk, Moderator: Markov					
Reflecting Boundaries					
Case 1		Case 2		Case 3	
Calc.	k_∞	Calc.	k_∞	Calc.	k_∞
2.1	1	2.2	$\nu/2$	2.3	ν
Set 3: Fuel: Disk, Moderator: Matrix					
Reflecting Boundaries					
Case 1		Case 2		Case 3	
Calc.	k_∞	Calc.	k_∞	Calc.	k_∞
3.1	1	3.2	$\nu/2$	3.3	ν

Table 5: Calculation Set 1-3 Variable Parameter Values, Reflecting Boundaries

of an infinite lattice of a randomly fueled planar geometry system of length (X). In the case of vacuum boundaries, these solutions are related to transport solutions for a small subcritical, randomly fueled assembly.

3.6 Summary

This chapter outlines the method used to generate individual realizations of the mixing statistics. The preconditioned discretized transport algorithm of Chapter 2 is integrated into a statistical sampling algorithm to generate realizations of the binary stochastic mixture. The method for calculating the ensemble average k -eigenvalue and scalar flux was given, and the determination of convergence of the statistical solution was discussed.

The origin of the distributions of the mixing statistics was discussed. These distributions approximate the distribution of segment lengths for a random chord

through a simplified two-material PWR fuel assembly model. The cross section data used in this study is based on a two-group collapsed PWR pin cell calculation using CASMO-3. The variability in these cross sections based on common assumptions in reactor analysis was given. Finally, a listing of the calculations performed and what knowledge is expected to be gleaned from their solution was provided.

4 RESULTS

4.1 Introduction

This chapter gives the results for the three sets of calculations considered with both vacuum and reflecting boundary conditions. Trends are identified in the statistical solutions of ensemble group scalar flux and the k-eigenvalue when varying k_∞ and c^{fuel} . Representative plots are shown of the group scalar flux and k-eigenvalue PDF. Finally, the atomic mix approximation is compared with the calculated benchmark ensemble average quantities.

4.2 Ensemble Average Group Flux Behavior

To develop intuition regarding ensemble quantities, a discussion of group scalar flux solutions of individual realizations is necessary. Figure 8 and 9 show group scalar flux plots for a realization of calculation 1.1. The fast group scalar flux shows a peak in fuel segments, as all the fission neutrons are born in this group. A fast group neutron that interacts with the moderator will slow down to the thermal group if an interaction takes place. Therefore, the fast group scalar flux will show a trough in the moderator segments. The reverse of this profile is observed in the thermal group. The thermal group scalar flux shows a trough in the fuel segments since the absorption of thermal neutrons drives the fission reaction. The thermal scalar flux peaks in the moderator segments since those neutrons which slow down from the fast group are a source for the thermal group.

Figure 8 and 9 also display the widely varying segment lengths which can occur in any given realization of Markovian mixing statistics. With such variable segment

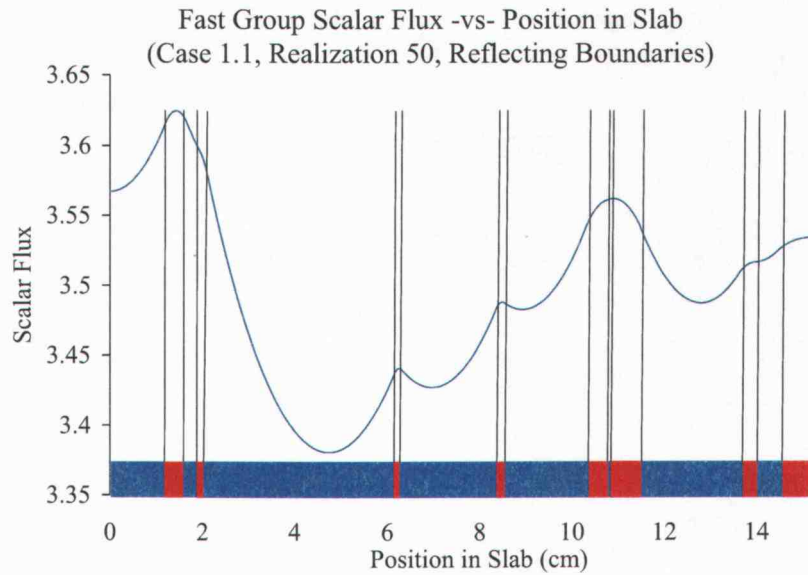


Figure 8: Fast Group Solution, Calculation 1.1, Realization 50

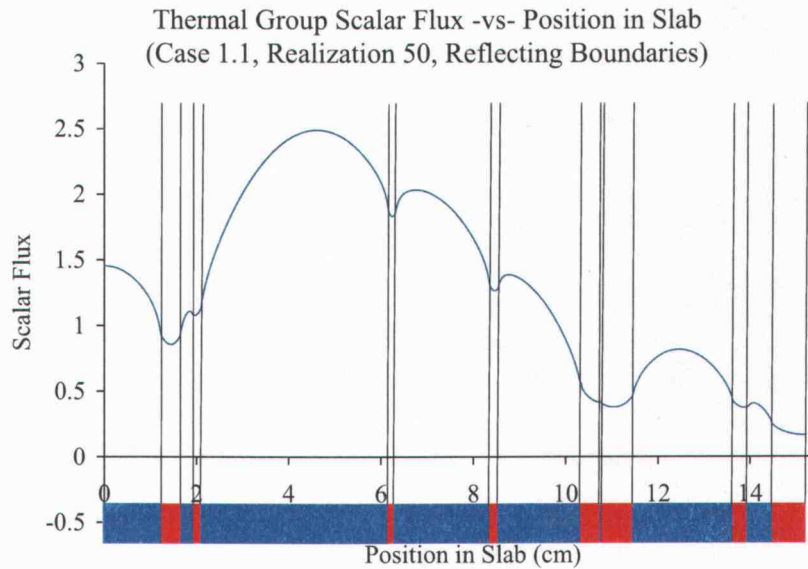


Figure 9: Thermal Group Solution, Calculation 1.1, Realization 50

lengths, and consequent variation in the flux profile shape and magnitude, a large standard deviation about the ensemble average group flux solution is expected. Similar flux shapes are observed in problems with vacuum boundaries.

Figure 10 shows the thermal scalar flux solutions of four individual realizations and the ensemble average solution with a $\pm 2\sigma$ confidence interval, for calculation 1.1. This figure shows the wide variation in the shape and magnitude of

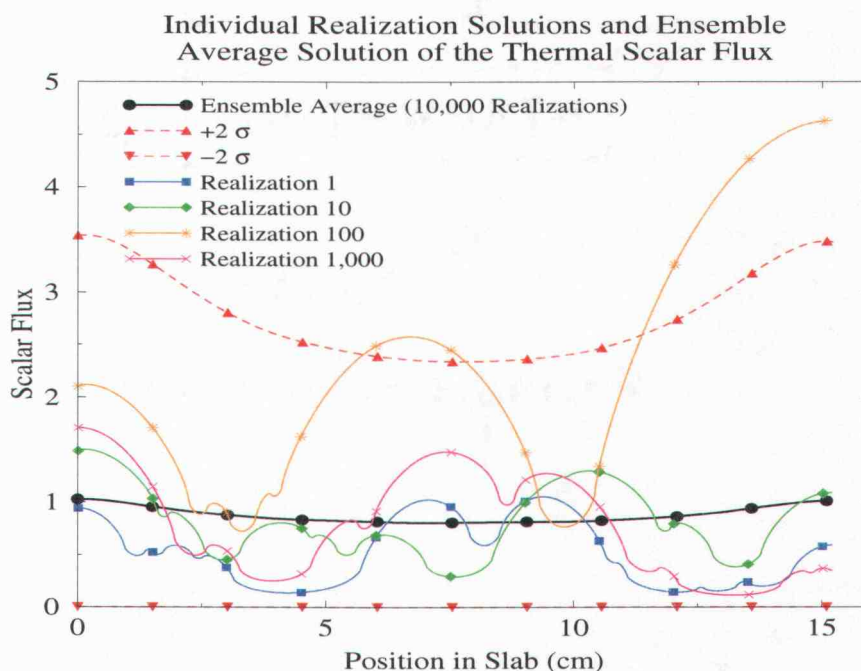


Figure 10: Four Thermal Group Scalar Flux Solutions and the Ensemble Average Solution - Calculation 1.1

the thermal flux in individual realizations. These solutions explain the size of the $+2\sigma$ confidence interval. [The -2σ confidence is bounded by zero, since negative flux values are unphysical]. Given a large number of realizations, 95.4% of the flux solutions produced for individual realizations lie within a 2σ confidence interval [Lew 93].

Figures 11 and 12 show the convergence of the ensemble average flux solution of

the fast and thermal flux respectively. The convergence of the mean is not strictly from the top or bottom, but appears random, as it should for this stochastic calculation.

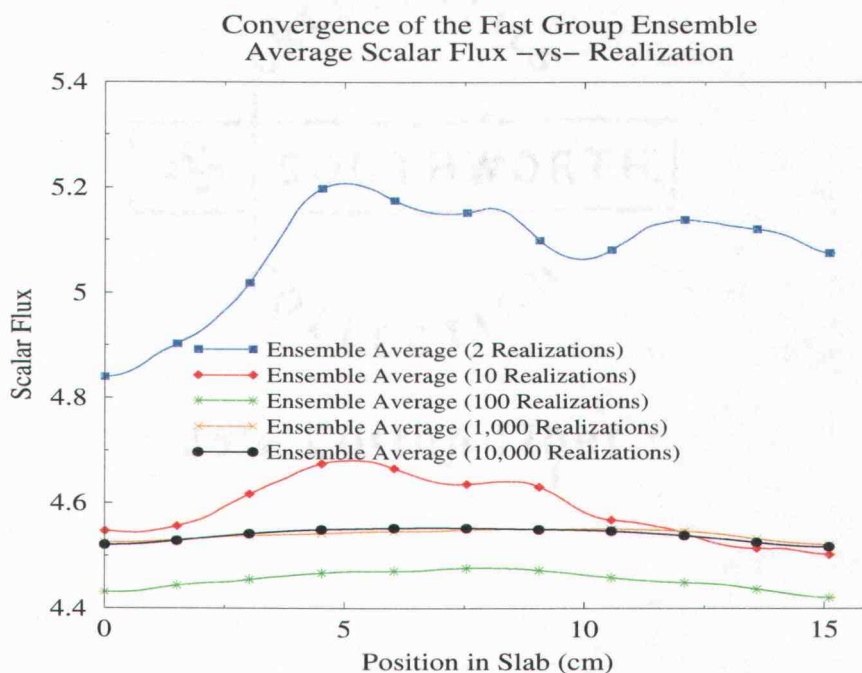


Figure 11: Convergence of the Fast Group Ensemble Average Scalar Flux - Calculation 1.1

4.3 Code Validation and Statistical Convergence

A brief outline of the code validation and the statistical convergence of the ensemble averaged quantities is given to establish confidence in the deterministic transport results. A suite of tests is used to validate the transport section of the code. These include a number of homogeneous infinite medium calculations, for which the flux and k-eigenvalue solutions can be solved analytically. The code is also tested against analytic diffusion with extrapolated boundaries for the case of vacuum boundaries. The accelerated transport algorithm has been shown to give

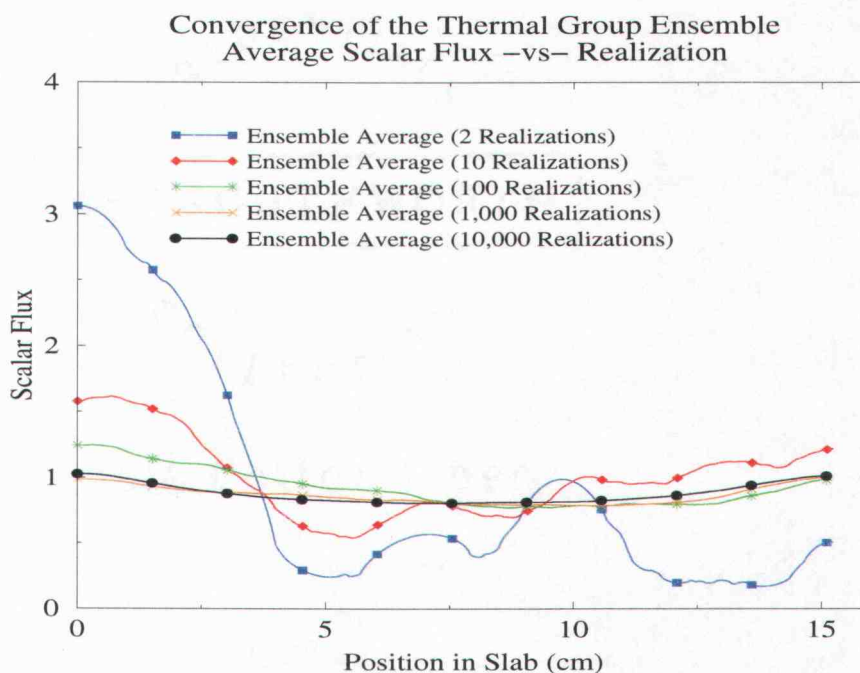


Figure 12: Convergence of the Thermal Group Ensemble Average Scalar Flux - Calculation 1.1

the unaccelerated transport solution of the flux and k -eigenvalue for both vacuum and reflecting boundary conditions. The group scalar flux and k -eigenvalue solutions were shown to be in excellent agreement compared with another planar geometry transport code employing the linear-discontinuous spatial discretization. The convergence tolerance for the k -eigenvalue and group scalar flux for each realization was 10^{-5} and 10^{-4} absolute error, respectively.

The statistical convergence of the ensemble quantities is tested and monitored for every 10^{th} realization to avoid terminating the calculation prematurely. The convergence of both the mean and standard deviation of the group flux and k -eigenvalue are monitored. The calculation is allowed to complete only after a statistically significant number of realizations, ensuring that the mixing statistics have been well-sampled. The minimum number of realizations considered is 10,000,

which is based on previous experience in performing these types of calculations.

Figure 4 of Section 3.2 shows the typical convergence of ensemble quantities as a function of an increasing number of realizations. The relative error decreases as $1/\sqrt{R}$ with some statistical fluctuation. The convergence of the ensemble average and standard deviation of the flux are the tested quantities, as they appear to have the slowest convergence rate. A 0.1% convergence tolerance was used for the ensemble average and standard deviation of the scalar flux. Entire benchmark calculations take between 5 and 9 hours on a 750 MHz Sun UltraSPARCTM III processor.

The ensemble k -eigenvalue and group scalar flux solutions will now be discussed for each group of mixing statistics. The results of the ensemble calculations described in Tables 2-4 for vacuum boundaries and Table 5 for reflecting boundaries are discussed below.

4.4 Markov-Markov Mixing Statistics - Vacuum Boundaries

The first set of results considered are those for Set 1, having mixing statistics which consist of Markovian segment length distributions in both the fuel and moderator materials, with vacuum boundaries.

4.4.1 The k -Eigenvalue

In Tables 2-4 each vacuum boundary calculation is designated by “calculation $x.y.z$ ”. “ z ” refers to the value of k_∞ and can take on the values $z = 1, 2, 3$ corresponding to $k_\infty = 1, \nu/2, \nu$, respectively. “ y ” refers to the value of c^{fuel} and can take on the values $y = 1, 2, 3$ corresponding to $c^{fuel} = 0.1, 0.5, 0.9$, respectively. “ x ” refers to the set of mixing statistics and can take on the values of $x = 1, 2, 3$ corre-

sponding to the different sets of mixing statistics given in Table 6. In this section,

Material Distribution Designation		
“x”	Fuel	Moderator
1	Markovian	Markovian
2	Disk	Markovian
3	Disk	Matrix

Table 6: Designation of the Material Segment Length Distributions For Each Calculation Set

only $x = 1$ is discussed. Table 7 shows the k -eigenvalue data from the nine vacuum boundary calculations performed with Markovian segment length distributions in each material.

Ensemble k -Eigenvalue Results			
Calc.	\bar{k}	$\sigma_{\bar{k}}$	$(\frac{\sigma_{\bar{k}}}{\bar{k}}\%)$
1.1.1	0.2000	0.02995	14.98
1.1.2	0.3174	0.04516	14.23
1.1.3	0.4216	0.05790	13.73
1.2.1	0.1996	0.03018	15.12
1.2.2	0.3161	0.04575	14.47
1.2.3	0.4194	0.05861	13.98
1.3.1	0.2072	0.03188	15.39
1.3.2	0.3256	0.04796	14.73
1.3.3	0.4301	0.06115	14.22

Table 7: k -Eigenvalue Results for Set 1; Markov-Markov Statistics, Vacuum Boundaries

The first column of Table 7 lists the calculation designator of each of the nine calculations considered in this section. This is followed by the corresponding ensemble average k -eigenvalue (\bar{k}), the standard deviation about this average ($\sigma_{\bar{k}}$), and the percent relative standard deviation ($\frac{\sigma_{\bar{k}}}{\bar{k}}\%$).

The increase in \bar{k} as a function of increased k_{∞} for a fixed c^{fuel} reflects the

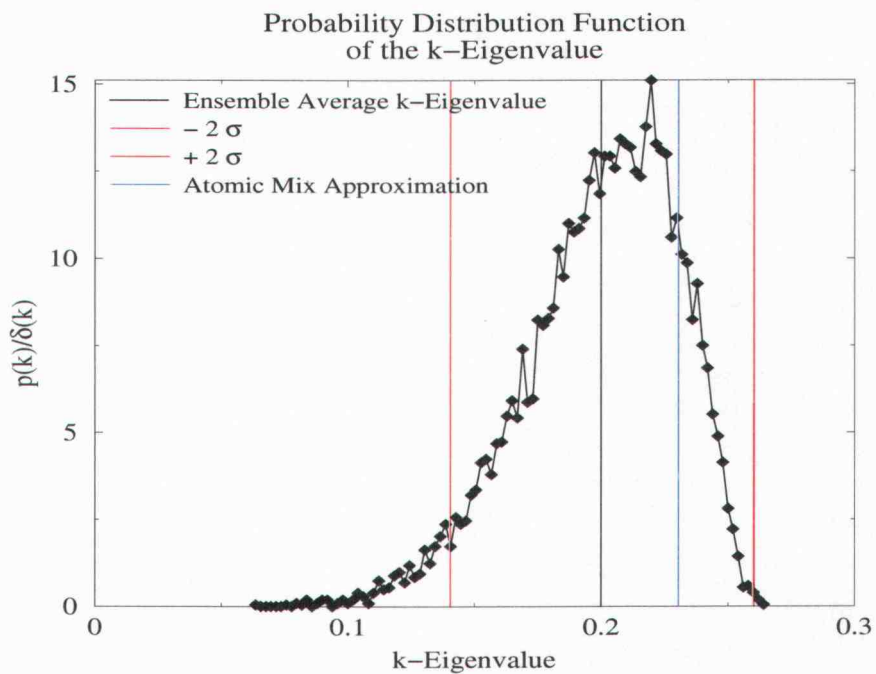
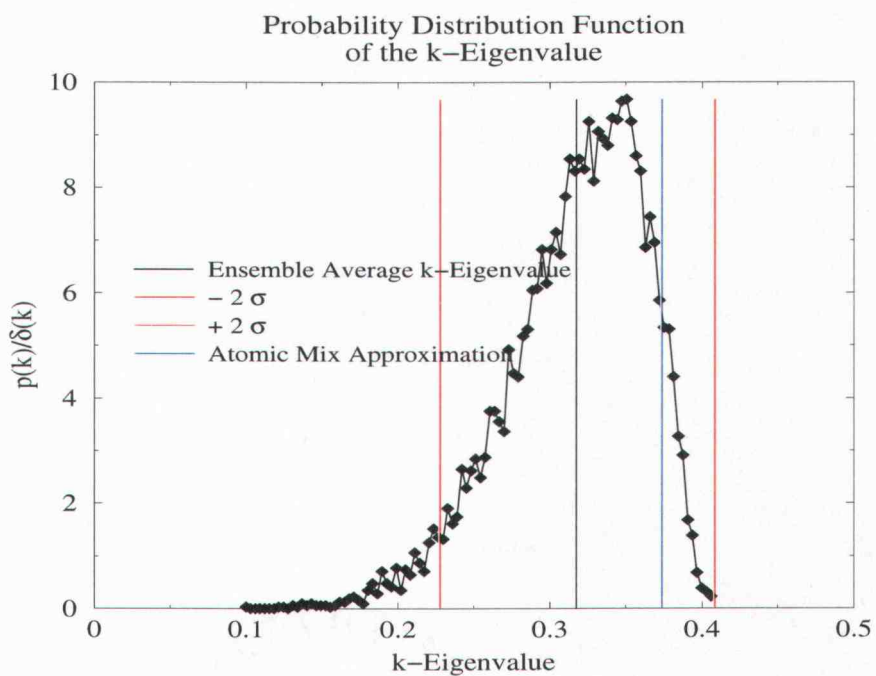
greater probability of fission occurring when neutrons are absorbed in the fuel material. This is not a linear increase. As k_∞ is increased from 1 to $\nu/2$ (a factor of ≈ 1.21) \bar{k} increases a factor of ≈ 1.6 . k_∞ is increase from $\nu/2$ to ν (a factor of 2) yielding only another factor of ≈ 1.3 .

An increase in c^{fuel} with fixed k_∞ does not significantly impact the value of \bar{k} or the standard deviation for the two smallest values of c^{fuel} (0.1 and 0.5). There is a small but noticeable increase in these two quantities for the largest value of c^{fuel} (0.9).

With the increase in k_∞ there is a corresponding increase in the standard deviation of the k-eigenvalue. This increase is slightly smaller than the increase in \bar{k} . The relative standard deviation is relatively independent of the increase in k_∞ .

Three examples of the k-eigenvalue PDF are shown in Figures 13 - 15, which were generated for calculations 1.1.1 - 1.1.3. The shape of the k-eigenvalue PDFs resemble a skewed Gaussian distribution with a truncation of the tail on the right-hand side. There is a noticeable and expected shift in the k-eigenvalue PDF toward larger k-eigenvalues, for increasing k_∞ . The relative standard deviation is nearly constant as a function of increasing k_∞ , which can be seen in the consistent size of the $\pm 2\sigma$ width about the mean.

Figure 16 shows how increasing k_∞ increases the range of possible k-eigenvalues, with a shift toward larger k-eigenvalues. An increase in c^{fuel} causes a small broadening of the k-eigenvalue PDF for the largest value of c^{fuel} . This effect is shown for calculations 1.1.1, 1.2.1, and 1.3.1 in Figure 17 below. The PDF of the k-eigenvalue is very similar as a function of increasing c^{fuel} with constant k_∞ . The overall skewed Gaussian shape is not greatly impacted by either a change in k_∞ or c^{fuel} .

Figure 13: k -Eigenvalue PDF - Calculation 1.1.1Figure 14: k -Eigenvalue PDF - Calculation 1.1.2

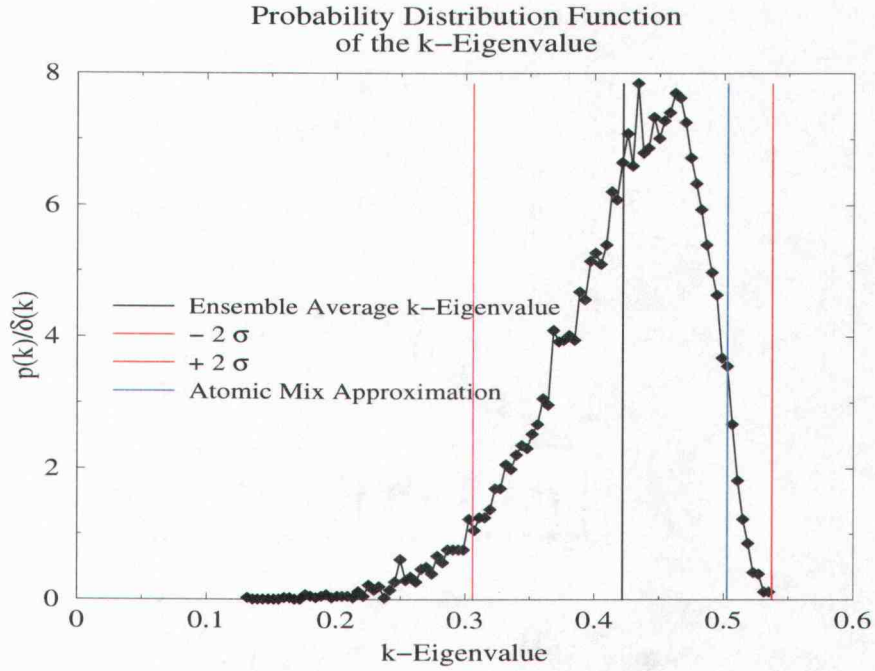
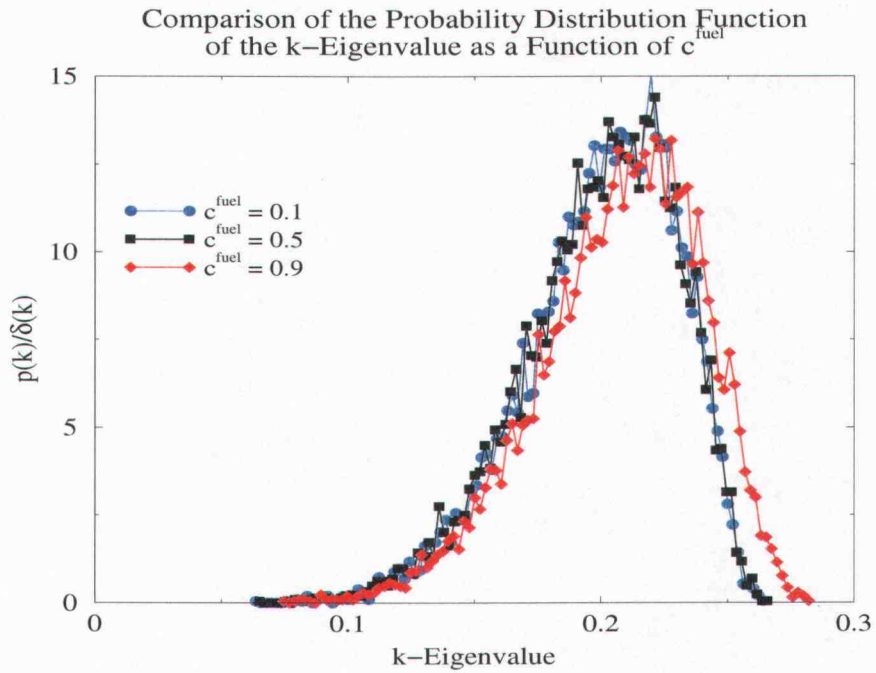
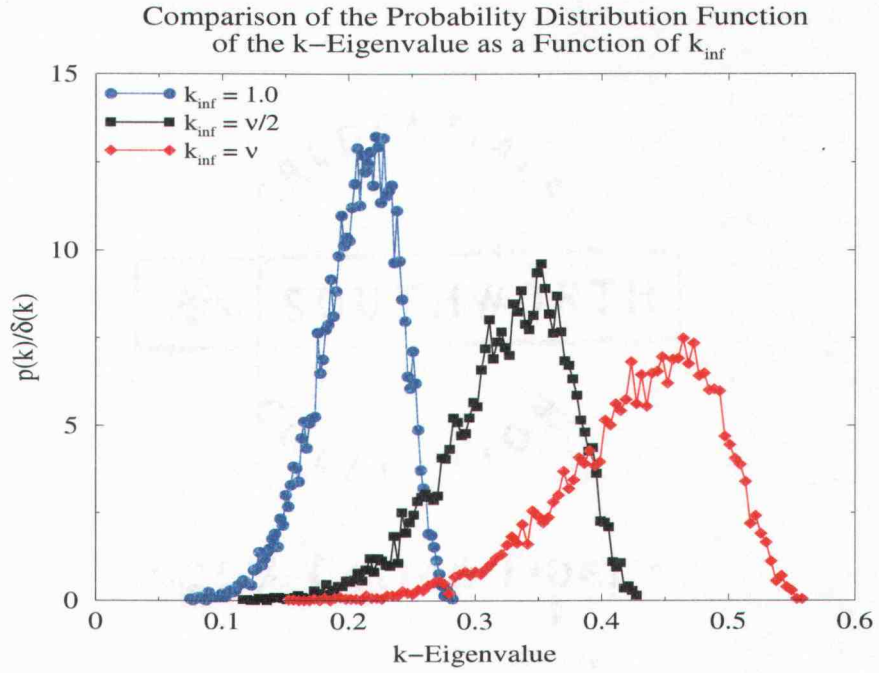


Figure 15: k-Eigenvalue PDF - Calculation 1.1.3

4.4.2 Scalar Flux

Table 8 and 9 give results for the fast and thermal group scalar flux, respectively. Since the flux is a function of space, the minimum and maximum value of both the ensemble average group scalar flux ($(\bar{\phi}_g)_{min}$ and $(\bar{\phi}_g)_{max}$), the standard deviation ($(\sigma_{\bar{\phi}_g})_{min}$ and $(\sigma_{\bar{\phi}_g})_{max}$), and the percent relative standard deviation ($(\frac{\sigma_{\bar{\phi}_g}}{\bar{\phi}_g}\%)_{min}$ and $(\frac{\sigma_{\bar{\phi}_g}}{\bar{\phi}_g}\%)_{max}$) are given. In Figures 18 - 21 it is observed that all of the Set 1 ensemble average solutions with vacuum boundaries have the characteristic symmetric cosine shape of a homogeneous medium flux solution, as does the standard deviation. The minimum and maximum of these quantities illustrate the effect of the variable parameters on the shape of these two solutions, i.e. similar maxima and minima indicate a flat profile, while dissimilar maxima and minima indicate a peaked flux profile.



Fast Group Flux Results						
Calc.	$(\bar{\phi}_1)_{min}$	$(\bar{\phi}_1)_{max}$	$(\sigma_{\bar{\phi}_1})_{min}$	$(\sigma_{\bar{\phi}_1})_{max}$	$\left(\frac{\sigma_{\bar{\phi}_1}}{\bar{\phi}_1}\%\right)_{min}$	$\left(\frac{\sigma_{\bar{\phi}_1}}{\bar{\phi}_1}\%\right)_{max}$
1.1.1	3.9458	6.0618	0.8396	1.2080	19.84	21.99
1.1.2	2.4744	3.8350	0.5065	0.7455	19.39	20.89
1.1.3	1.8570	2.8931	0.3743	0.5496	18.95	20.32
1.2.1	3.7648	6.1130	0.8023	1.2256	19.91	22.38
1.2.2	2.3664	3.8710	0.4761	0.7604	19.58	20.92
1.2.3	1.7782	2.9112	0.3476	0.5629	19.21	20.12
1.3.1	3.0058	6.3814	0.7611	1.3750	21.36	26.88
1.3.2	1.9708	4.0455	0.4334	0.8623	21.18	24.10
1.3.3	1.4411	3.0543	0.3057	0.6440	20.59	22.51

Table 8: Fast Group Flux Results for Set 1; Markov-Markov Statistics, Vacuum Boundaries

These results reveal that as k_∞ increases, the group ensemble average scalar flux, standard deviation, and relative standard deviation decrease for fixed c^{fuel} . This behavior is the inverse of that of the ensemble average and standard deviation of the k-eigenvalue. For fixed k_∞ , the magnitude of the ensemble average scalar flux and relative standard deviation is not greatly impacted for the two smallest values of c^{fuel} , with a shift in the shape for the largest value of c^{fuel} . The shape shifts to a more highly peaked flux profile as indicated by a decrease in the minimum ensemble average flux and an increase in the maximum. The magnitude of the fast group scalar flux is greater than that of the thermal group. However, the relative standard deviation is much greater in the thermal group.

Representative plots of the group scalar flux (with $\pm 2\sigma$ confidence interval) and the atomic mix approximation are shown in Figures 18 - 21 for calculation 1.1.1 and calculation 1.3.1. [These are for an increasing value of c^{fuel} with constant k_∞ , since the introduction of more fast group scattering in the fuel results in an increasingly peaked shape of the fast and thermal scalar flux profiles.] The shape

Thermal Group Flux Results						
Calc.	$(\bar{\phi}_2)_{min}$	$(\bar{\phi}_2)_{max}$	$(\sigma_{\bar{\phi}_2})_{min}$	$(\sigma_{\bar{\phi}_2})_{max}$	$\left(\frac{\sigma_{\bar{\phi}_2}}{\bar{\phi}_2}\%\right)_{min}$	$\left(\frac{\sigma_{\bar{\phi}_2}}{\bar{\phi}_2}\%\right)_{max}$
1.1.1	0.1655	0.9887	0.1116	0.9010	67.40	91.79
1.1.2	0.1322	0.8073	0.0699	0.6442	52.85	80.16
1.1.3	0.1161	0.7288	0.0522	0.5359	44.81	73.72
1.2.1	0.1627	0.9964	0.1122	0.9066	68.94	92.06
1.2.2	0.1305	0.8122	0.0705	0.6471	54.05	80.06
1.2.3	0.1154	0.7325	0.0529	0.5378	45.84	73.65
1.3.1	0.1483	1.0296	0.1101	0.9315	74.23	94.50
1.3.2	0.1216	0.8333	0.0705	0.6603	57.98	81.51
1.3.3	0.1089	0.7485	0.0536	0.5473	49.20	74.02

Table 9: Thermal Group Flux Results for Set 1; Markov-Markov Statistics, Vacuum Boundaries

of the flux profile is independent of an increasing value of k_∞ for fixed c^{fuel} , only the magnitude is decreased.

The cosine shape of the flux profile is consistent with a symmetric homogeneous medium solution. Each realization may look very different (as in Figure 10) but this variability decreases with the averaging process. All of the fast and thermal flux profiles with Markovian segment length distributions in each material and vacuum boundaries have this characteristic cosine shape. The 2σ confidence interval is bounded from the bottom by zero since negative fluxes are never produced as they are unphysical. The flux profile takes on a more peaked curve as c^{fuel} increases. The standard deviation broadens in the fast group as c^{fuel} increases. The fast group standard deviation is smaller than that of the thermal group. The standard deviation in the thermal group increases only slightly with an increase in c^{fuel} .

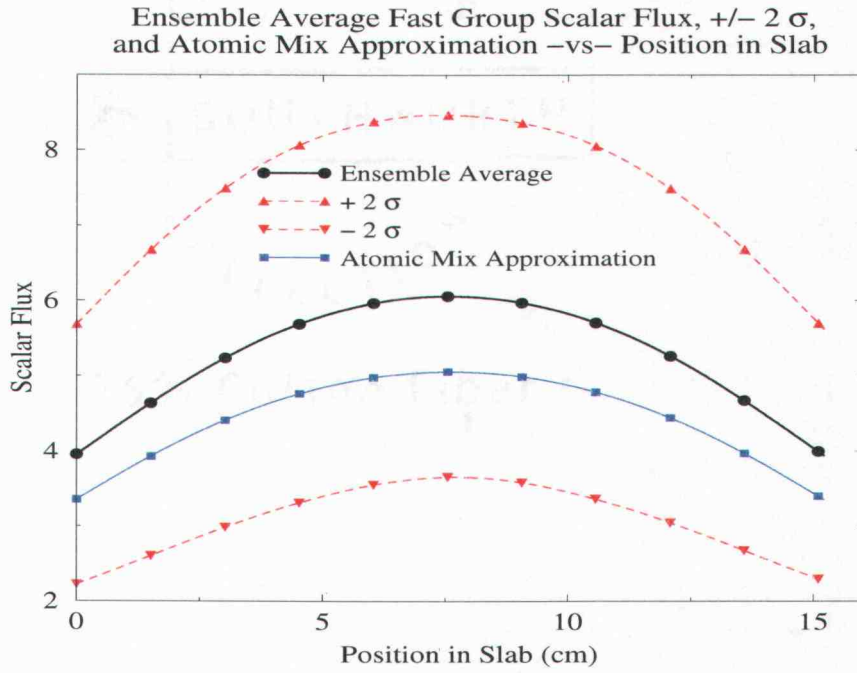


Figure 18: Ensemble Average Fast Group Flux - Calculation 1.1.1

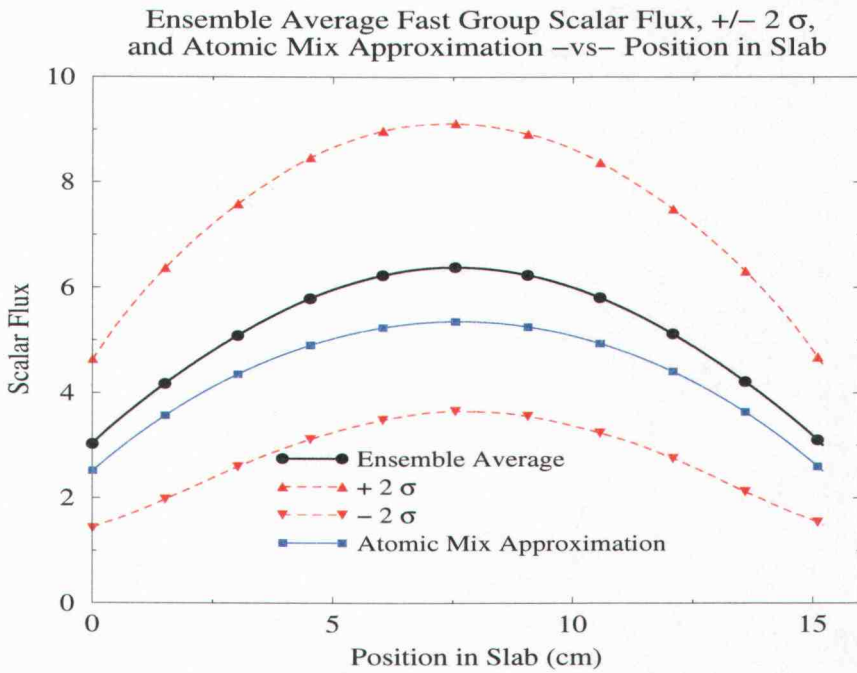


Figure 19: Ensemble Average Fast Group Flux - Calculation 1.3.1

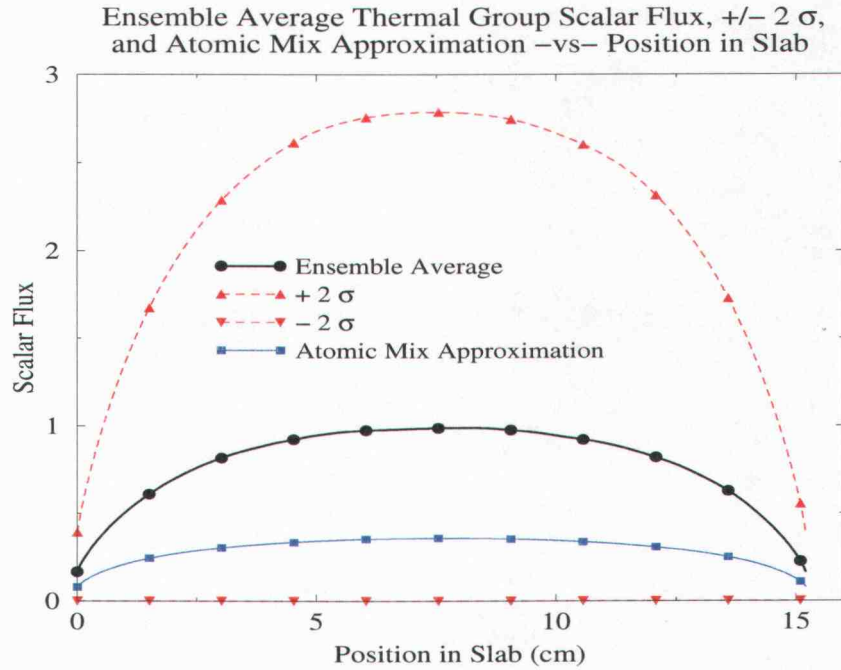


Figure 20: Ensemble Average Thermal Group Flux - Calculation 1.1.1

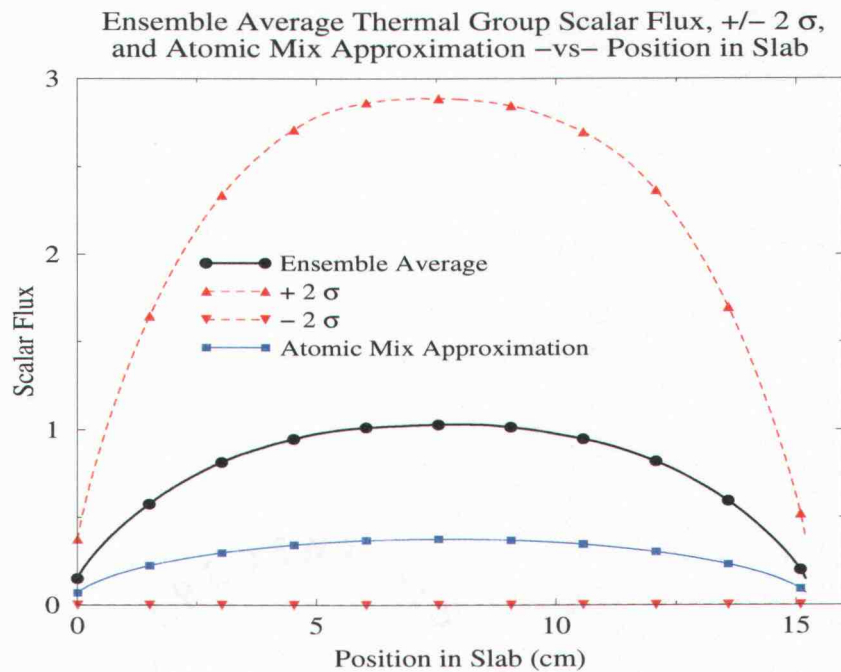


Figure 21: Ensemble Average Thermal Group Flux - Calculation 1.3.1

4.4.3 The Atomic Mix Approximation

A comparison of atomic mix predictions of the ensemble average k-eigenvalue is given below in Table 10. Atomic mix yields conservative estimates of \bar{k} , with

Atomic Mix k-Eigenvalue Comparison			
Calc.	k	$k_{a.m.}$	%R.E.
1.1.1	0.2000	0.2301	15.04
1.1.2	0.3174	0.3729	17.51
1.1.3	0.4216	0.5026	19.22
1.2.1	0.1996	0.2292	14.84
1.2.2	0.3161	0.3718	17.63
1.2.3	0.4194	0.5013	19.53
1.3.1	0.2072	0.2388	15.27
1.3.2	0.3256	0.3884	19.28
1.3.3	0.4301	0.5245	21.94

Table 10: Atomic Mix Prediction of the Ensemble Average k-Eigenvalue for Set 1; Markov-Markov Statistics, Vacuum Boundaries

the relative error ranging between $\approx 15 - 22\%$. The atomic mix prediction of \bar{k} always is contained in the 2σ confidence interval, but always lies outside of the 1σ confidence interval. The difference between the atomic mix and benchmark \bar{k} increases with increasing k_∞ , and is relatively insensitive to changes in c^{fuel} .

For all of the calculations considered, atomic mix under-predicts the magnitude of the flux in both energy groups. This can be seen in Figures 18 - 21 for calculation 1.1.1 and calculation 1.3.1. A comparison of atomic mix predictions of fast and thermal group scalar fluxes is given below in Table 11. The underestimation of the atomic mix approximation is evident, since all of the ratios are greater than unity. Since the flux is a normalized quantity, it is of interest to determine if atomic mix correctly predicts the flux shape. The atomic mix approximation is a fair predictor

of the flux shape in the fast group: the maximum and minimum difference in the ratio vary between $\approx 1 - 5\%$. The atomic mix approximation of the thermal group scalar flux shape differs more significantly: the maximum and minimum ratios vary between $\approx 9 - 35\%$. For relatively flat flux profiles, atomic mix predicts the flux shape fairly well.

Atomic Mix Group Scalar Flux Comparison				
Calc.	$\left(\frac{\bar{\phi}_1}{\phi_{1,a.m.}}\right)_{min} \%$	$\left(\frac{\bar{\phi}_1}{\phi_{1,a.m.}}\right)_{max} \%$	$\left(\frac{\bar{\phi}_2}{\phi_{2,a.m.}}\right)_{min} \%$	$\left(\frac{\bar{\phi}_2}{\phi_{2,a.m.}}\right)_{max} \%$
1.1.1	1.1762	1.1991	2.0623	2.7742
1.1.2	1.2015	1.2196	1.8109	2.1957
1.1.3	1.2189	1.2333	1.6953	1.9410
1.2.1	1.1709	1.1967	2.0806	2.7746
1.2.2	1.1998	1.2183	1.8288	2.1947
1.2.3	1.2193	1.2326	1.7122	1.9397
1.3.1	1.1588	1.2048	2.1618	2.7684
1.3.2	1.1964	1.2490	1.9037	2.1865
1.3.3	1.2207	1.2771	1.7795	1.9328

Table 11: Ensemble Average / Atomic Mix Ratio of Group Scalar Flux Solutions for Set 1; Markov-Markov Statistics, Vacuum Boundaries

4.5 Markov-Markov Mixing Statistics - Reflecting Boundaries

In this section, Set 1 calculations are again considered, but with reflecting boundaries to assess the effect of leakage on ensemble quantities. Only three calculations are considered for increasing values of k_∞ since increasing fast group scattering (c^{fuel}) will not effect the solution with this boundary condition. Therefore, the calculation designation is reduced to “calculation x.z”, where only x = 1 is considered in this section.

4.5.1 The k -Eigenvalue

The k -eigenvalue data is given in Table 12 below. A trend similar to that of the vacuum boundary case is discovered. There is a non-linear increase in the ensemble average k -eigenvalue as k_∞ increases. A similar trend is present in the standard deviation.

Ensemble k -Eigenvalue Results			
Calc.	k	σ_k	$(\frac{\sigma_k}{k} \%)$
1.1	0.6202	0.08309	13.40
1.2	1.0359	0.13233	12.77
1.3	1.4359	0.17585	12.25

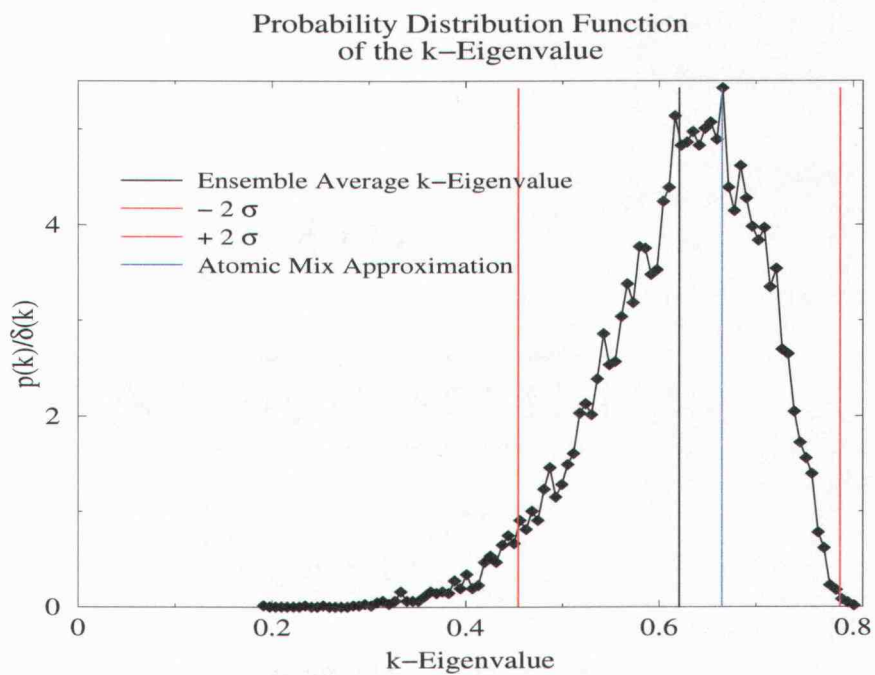
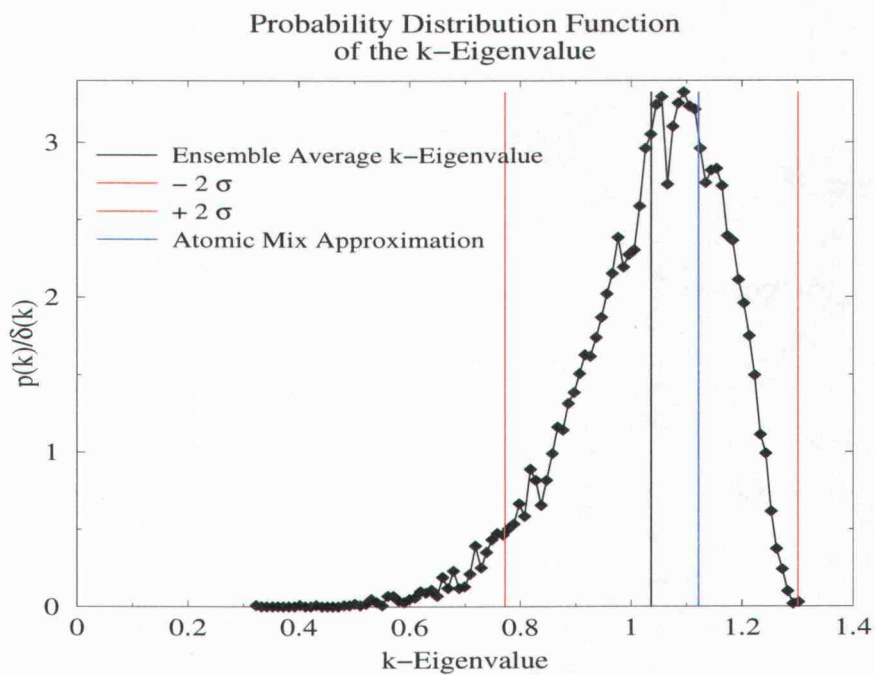
Table 12: k -Eigenvalue Results for Set 1; Markov-Markov Statistics, Reflecting Boundaries

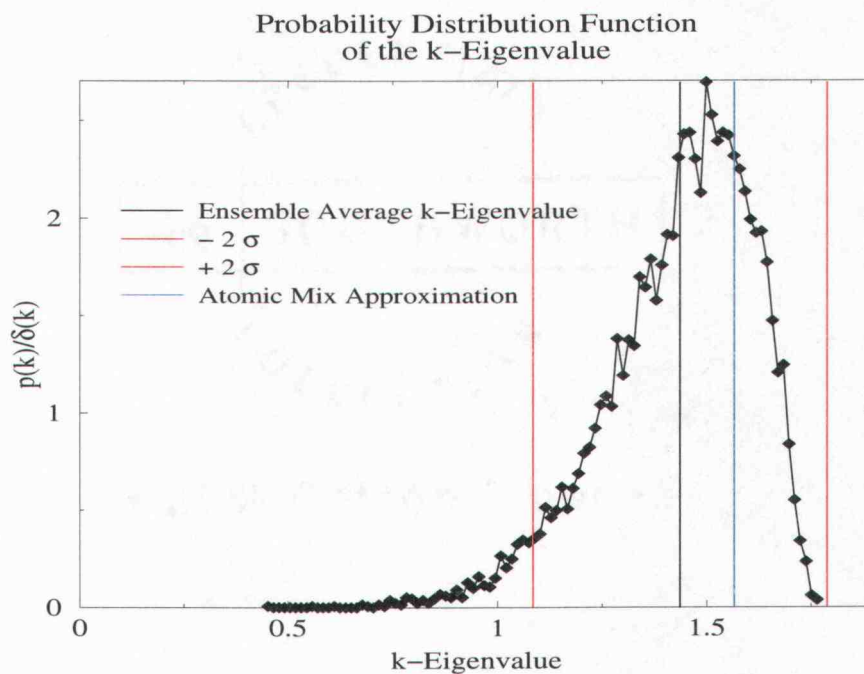
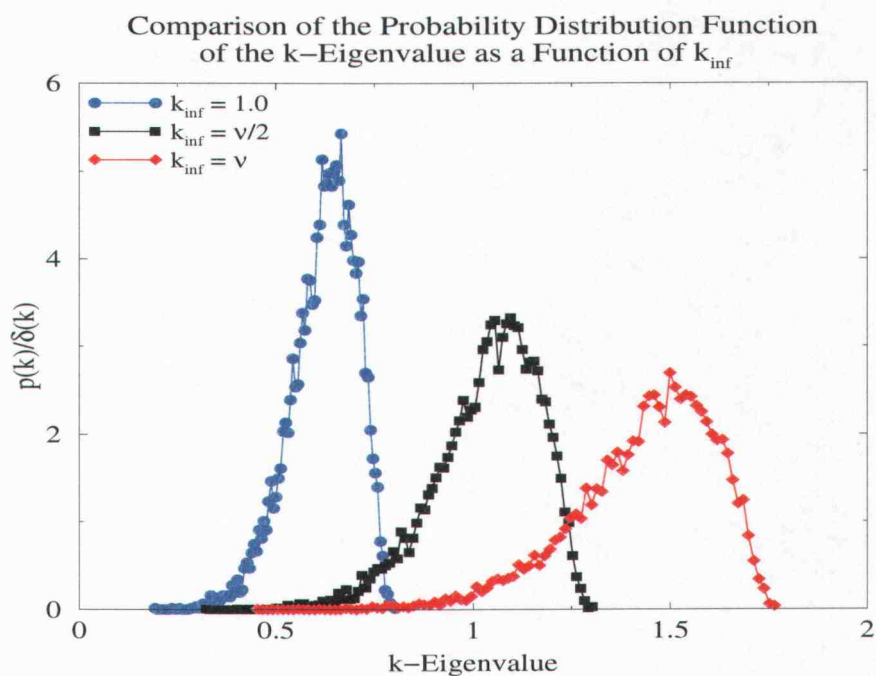
The k -eigenvalue probability distribution functions for these three calculations are shown in Figures 22 - 24 below. These k -eigenvalue PDFs resemble a skewed Gaussian distribution with a truncation of the tail on the right-hand side. All three plots show a similar relative standard deviation.

Figure 25 shows that an increase in k_∞ increases the range of possible k -eigenvalues, with a shift toward larger k -eigenvalues. The overall skewed Gaussian shape of the k -eigenvalue PDF is not greatly impacted by a change in k_∞ .

4.5.2 Scalar Flux

Tables 13 - 14 give results for the fast and thermal group scalar flux, respectively. As shown in the example flux plots below (Figures 26 - 29), all of the Set 1 solutions with reflecting boundaries have a relatively flat shape. The minimum and maximum of these quantities illustrate the effect of the variable parameters

Figure 22: k -Eigenvalue PDF - Calculation 1.1Figure 23: k -Eigenvalue PDF - Calculation 1.2

Figure 24: k -Eigenvalue PDF - Calculation 1.3Figure 25: k -Eigenvalue PDF - Calculation 1.1 - Calculation 1.3

on the shape of these two solutions. Similar maxima and minima designate a flat profile, while dissimilar maxima and minima indicate a peaked flux profile.

Fast Group Flux Results						
Calc.	$(\bar{\phi}_1)_{min}$	$(\bar{\phi}_1)_{max}$	$(\sigma_{\bar{\phi}_1})_{min}$	$(\sigma_{\bar{\phi}_1})_{max}$	$\left(\frac{\sigma_{\bar{\phi}_1}}{\bar{\phi}_1}\%\right)_{min}$	$\left(\frac{\sigma_{\bar{\phi}_1}}{\bar{\phi}_1}\%\right)_{max}$
1.1	4.5169	4.5525	0.8973	0.9201	19.72	20.35
1.2	2.7011	2.7216	0.5189	0.5293	19.07	19.58
1.3	1.9465	1.9605	0.3623	0.3688	18.49	18.94

Table 13: Fast Group Flux Results for Set 1; Markov-Markov Statistics, Reflecting Boundaries

Thermal Group Flux Results						
Calc.	$(\bar{\phi}_2)_{min}$	$(\bar{\phi}_2)_{max}$	$(\sigma_{\bar{\phi}_2})_{min}$	$(\sigma_{\bar{\phi}_2})_{max}$	$\left(\frac{\sigma_{\bar{\phi}_2}}{\bar{\phi}_2}\%\right)_{min}$	$\left(\frac{\sigma_{\bar{\phi}_2}}{\bar{\phi}_2}\%\right)_{max}$
1.1	0.8050	1.0261	0.7675	1.2563	94.79	122.70
1.2	0.6405	0.7817	0.5211	0.8157	81.07	105.17
1.3	0.5674	0.6728	0.4150	0.6267	72.99	94.11

Table 14: Thermal Group Flux Results for Set 1; Markov-Markov Statistics, Reflecting Boundaries

These results reveal that as k_∞ increases the group ensemble average scalar flux and standard deviation decreases. This is the inverse behavior of the ensemble average and standard deviation of the k-eigenvalue. The standard deviation decreases by a slightly greater factor than the ensemble average flux for increasing k_∞ . Therefore, the relative standard deviation decreases as a function of increasing k_∞ . The magnitude of the fast group scalar flux is greater than that of the thermal group. However, the relative standard deviation is much larger in the thermal group.

Representative plots are given for the group scalar fluxes (including the $\pm 2\sigma$

confidence interval) and the atomic mix approximation in Figures 26 - 29 for calculation 1.1 and calculation 1.3.

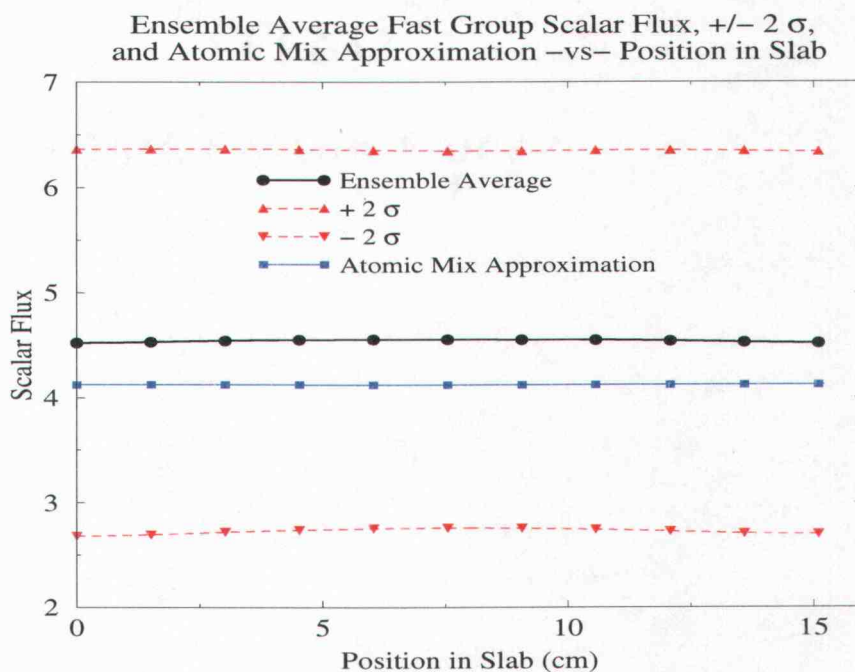


Figure 26: Ensemble Average Fast Group Flux - Calculation 1.1

These solutions show flat flux profiles, consistent with solutions of a homogeneous infinite medium. [Each realization may look very different but this variability decreases with the averaging process.]

4.5.3 The Atomic Mix Approximation

A comparison of the atomic mix prediction of ensemble average k -eigenvalue is given below in Table 15. This approximation yields conservative estimates of \bar{k} with relative errors ranging between $\approx 7 - 9\%$. The atomic mix prediction of \bar{k} always is contained in the σ confidence interval.

For all of the calculations considered, atomic mix under-predicts the magnitude

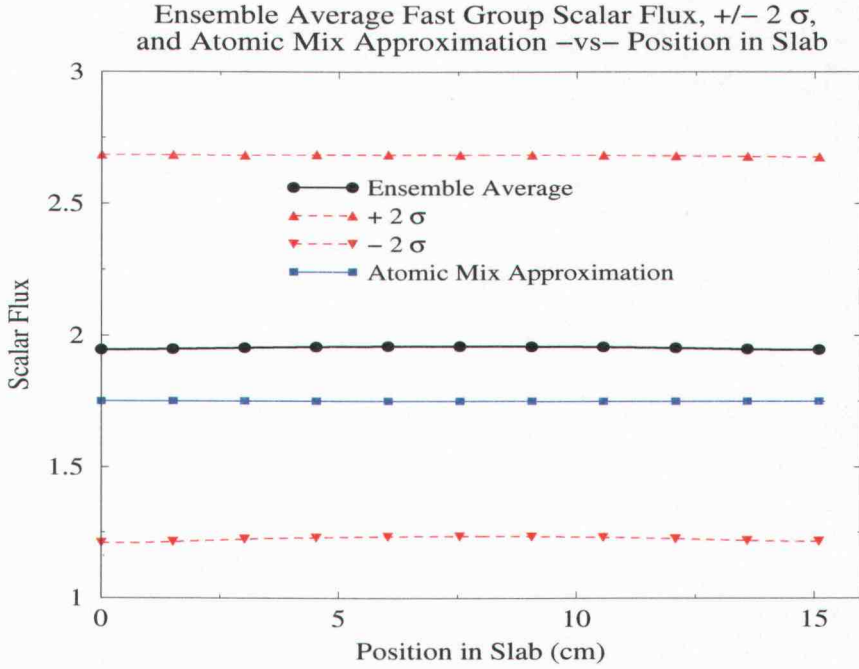


Figure 27: Ensemble Average Fast Group Flux - Calculation 1.3

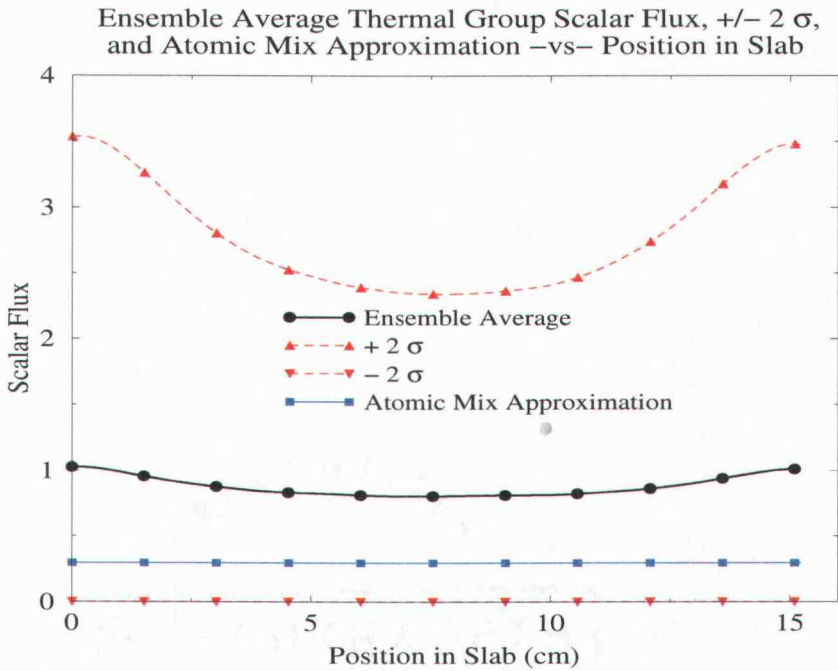


Figure 28: Ensemble Average Thermal Group Flux - Calculation 1.1

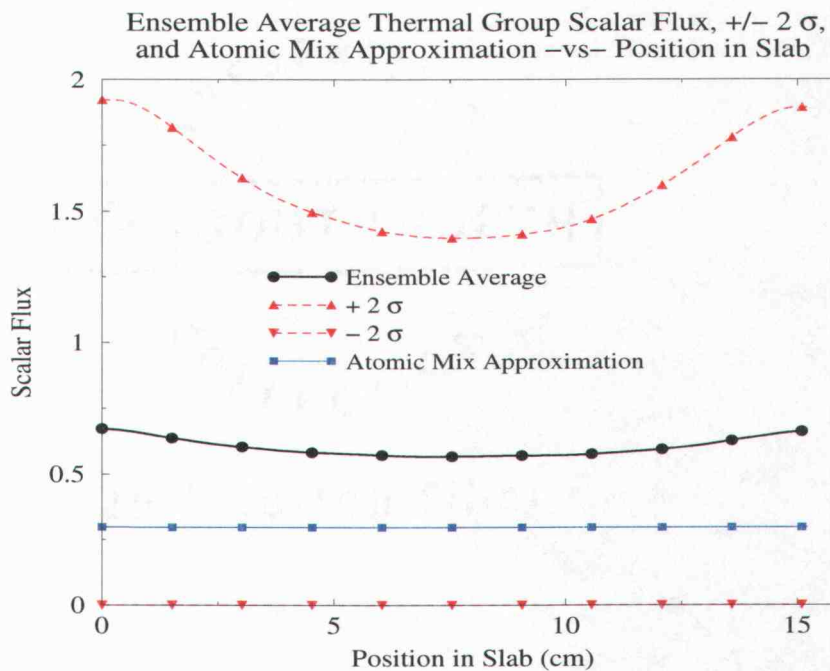


Figure 29: Ensemble Average Thermal Group Flux - Calculation 1.3

Atomic Mix k-Eigenvalue Comparison			
Calc.	k	$k_{a.m.}$	%R.E.
1.1	0.6202	0.6646	7.15
1.2	1.0359	1.1209	8.21
1.3	1.4359	1.5653	9.01

Table 15: Atomic Mix Prediction of the Ensemble Average k-Eigenvalue for Set 1; Markov-Markov Statistics, Reflecting Boundaries

of the flux in both energy groups. This is evident in the representative plots of Figures 26 - 29 for calculation 1.1 and calculation 1.3.

A comparison of the atomic mix prediction of the fast and thermal group scalar fluxes is given below in Table 16. The underestimation of the atomic mix ap-

Atomic Mix Group Scalar Flux Comparison				
Calc.	$\left(\frac{\bar{\phi}_1}{\phi_{1,a.m.}}\right)_{min} \%$	$\left(\frac{\bar{\phi}_1}{\phi_{1,a.m.}}\right)_{max} \%$	$\left(\frac{\bar{\phi}_2}{\phi_{2,a.m.}}\right)_{min} \%$	$\left(\frac{\bar{\phi}_2}{\phi_{2,a.m.}}\right)_{max} \%$
1.1	1.0958	1.1045	2.7158	3.4592
1.2	1.1053	1.1137	2.1607	2.6344
1.3	1.1123	1.1203	1.9141	2.2672

Table 16: Ensemble Average / Atomic Mix Ratio of Group Scalar Flux Solutions for Set 1; Markov-Markov Statistics, Reflecting Boundaries

proximation is evident, since all of the ratios are greater than unity. The atomic mix approximation is again a fair predictor of the flux shape in the fast group: the maximum and minimum difference in the ratio vary between $\approx 0.7 - 0.8\%$. The atomic mix approximation of the thermal group scalar flux shape differs more significantly: the maximum and minimum ratios vary between $\approx 18 - 27\%$. For relatively flat flux profiles, atomic mix will predict the flux shape fairly well.

4.6 Disk-Markov Mixing Statistics - Vacuum Boundaries

The second set of results considered are those for Set 2: the Disk segment length distribution in the fuel material and the Markovian segment length distribution in the moderator material, with vacuum boundaries.

4.6.1 The k -Eigenvalue

In this section, only calculations denoted by $x = 2$ are discussed. Table 17 shows the k -eigenvalue data from the nine vacuum boundary calculations performed with the fuel segment lengths governed by the Disk distribution, and the Markovian segment length distribution in the moderator material.

Ensemble k -Eigenvalue Results			
Calc.	\bar{k}	$\sigma_{\bar{k}}$	$(\frac{\sigma_{\bar{k}}}{\bar{k}}\%)$
2.1.1	0.2057	0.02102	10.22
2.1.2	0.3298	0.03130	9.49
2.1.3	0.4414	0.03958	8.97
2.2.1	0.2051	0.02151	10.49
2.2.2	0.3285	0.03200	9.74
2.2.3	0.4394	0.04037	9.19
2.3.1	0.2127	0.02321	10.91
2.3.2	0.3395	0.03440	10.13
2.3.3	0.4533	0.04320	9.53

Table 17: k -Eigenvalue Results for Set 2; Disk-Markov Statistics, Vacuum Boundaries

The increase in \bar{k} as a function of increased k_{∞} for a fixed c^{fuel} reflects the greater probability of fission occurring when neutrons are absorbed in the fuel material. This is again not a linear increase. As k_{∞} is increased from 1 to $\nu/2$ (a factor of ≈ 1.21) \bar{k} increases a factor of ≈ 1.6 . k_{∞} is increase from $\nu/2$ to ν (a factor of 2) yielding only another factor of ≈ 1.3 .

An increase in c^{fuel} with fixed k_{∞} does not significantly impact the value of \bar{k} or the standard deviation for the two smallest values of c^{fuel} (0.1 and 0.5). There is a small but noticeable increase in these two quantities for the largest value of c^{fuel} (0.9).

With the increase in k_∞ there is a corresponding increase in the standard deviation of the k-eigenvalue. This increase is smaller than the increase in \bar{k} , resulting in a decreasing relative standard deviation as a function of increasing k_∞ for a fixed c^{fuel} .

Three examples of the k-eigenvalue PDF are shown in Figures 30 - 32, which were generated for calculations 2.2.1 - 2.2.3. The shape of the k-eigenvalue PDFs resemble a skewed Gaussian distribution with a truncation of the tail on the right-hand side. There is a noticeable and expected shift in the k-eigenvalue PDF toward greater k-eigenvalues, for increasing k_∞ . The relative standard deviation is somewhat constant (slightly decreasing) as a function of increasing k_∞ . This can be seen by the somewhat consistent size of the $\pm 2\sigma$ width about the mean.

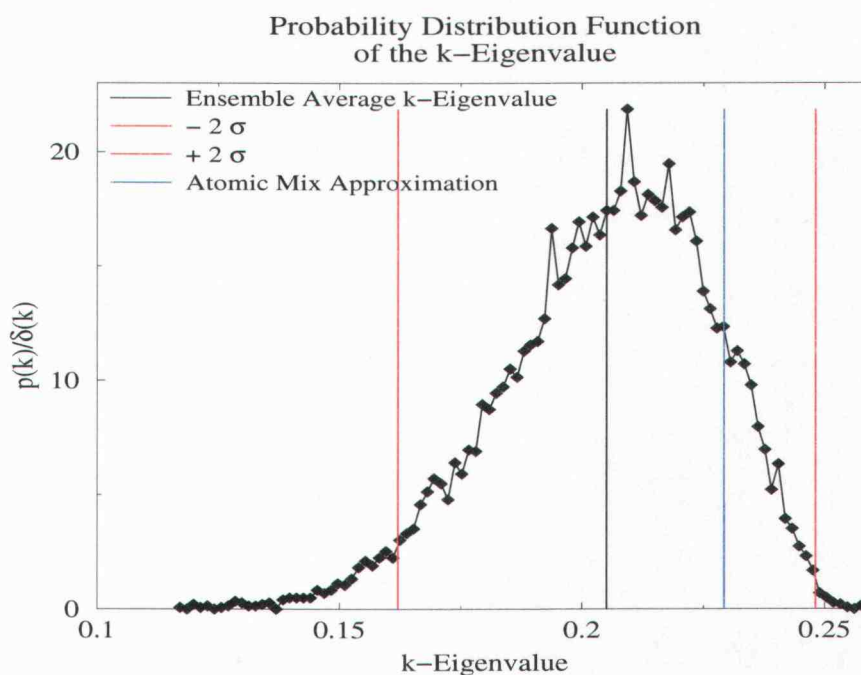


Figure 30: k-Eigenvalue PDF - Calculation 2.2.1

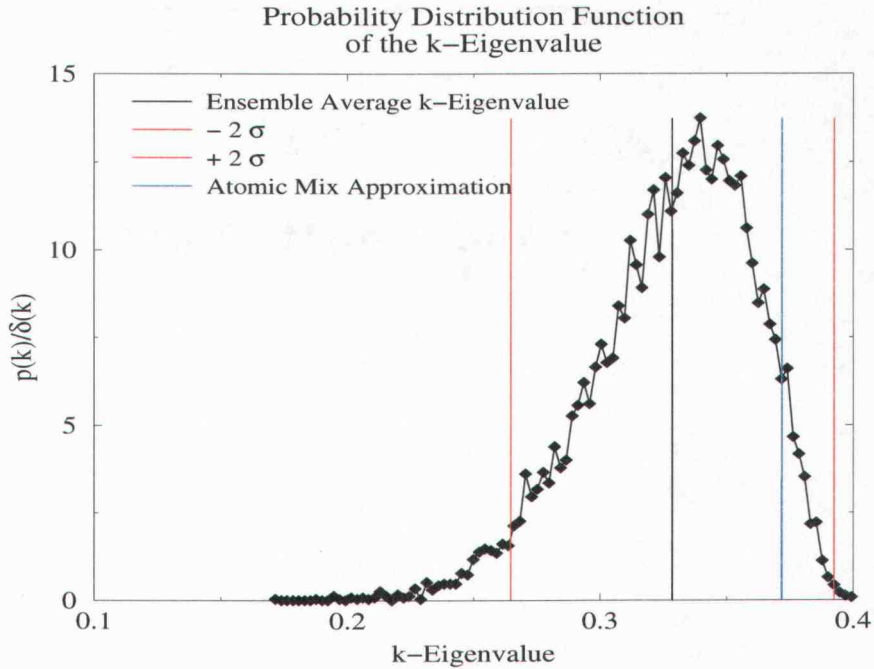


Figure 31: k-Eigenvalue PDF - Calculation 2.2.2

Figure 33 shows how increasing k_∞ widens the range of possible k-eigenvalues, with a shift toward larger k-eigenvalues. An increase in c^{fuel} causes a small broadening of the k-eigenvalue PDF for the largest value of c^{fuel} . This effect is shown for calculations 2.1.2, 2.2.2, and 2.3.2 in Figure 34 below. The PDF of the k-eigenvalue is very similar as a function of increasing c^{fuel} with constant k_∞ . The overall skewed Gaussian shape is not greatly impacted by either a change in k_∞ or c^{fuel} .

4.6.2 Scalar Flux

Table 18 and 19 give results for the fast and thermal group scalar flux, respectively. In Figures 35 - 38 it is observed that all of the Set 2 solutions with vacuum boundaries have the characteristic symmetric cosine shape of a homogeneous medium flux solution, as does the standard deviation about the ensemble

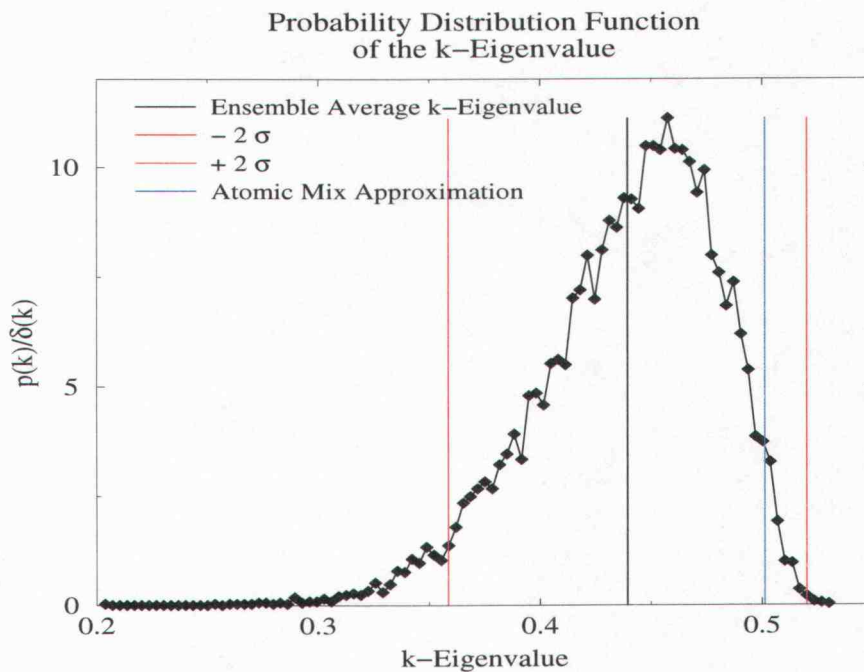


Figure 32: k-Eigenvalue PDF - Calculation 2.2.3

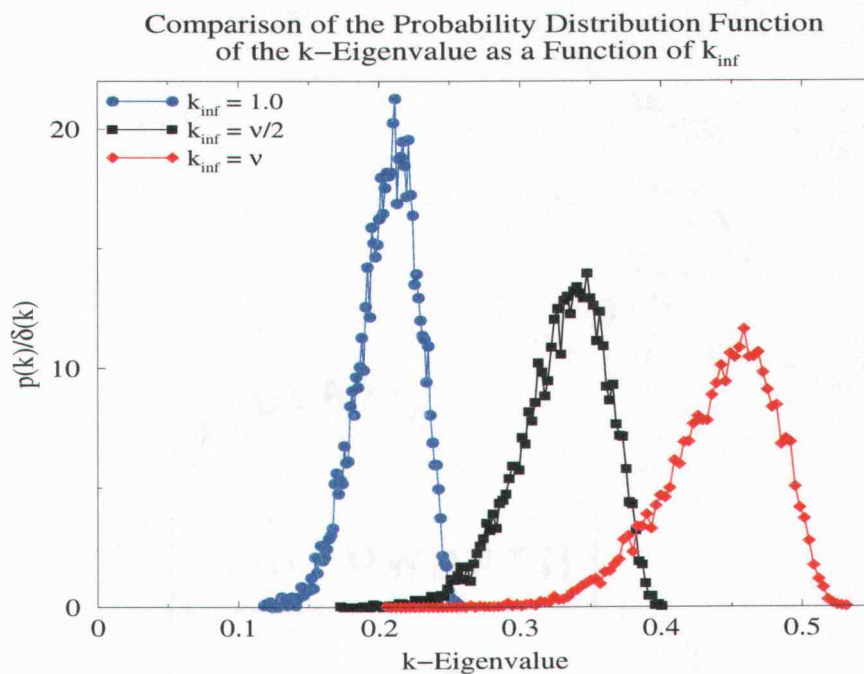


Figure 33: k-Eigenvalue PDF - Calculation 2.1.1, 2.1.2, 2.1.3

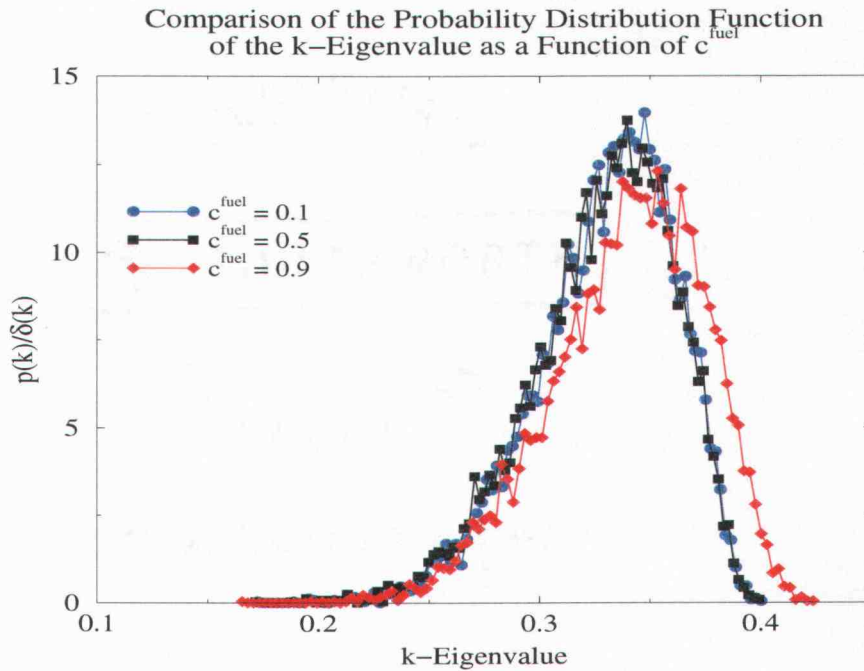


Figure 34: k -Eigenvalue PDF - Calculation 2.1.2, 2.2.2, 2.3.2

average. The minimum and maximum of these quantities illustrate the effect of the variable parameters on the shape of these two solutions.

These results reveal that as k_{∞} increases, the group ensemble average scalar flux, standard deviation, and relative standard deviation decrease for fixed c^{fuel} . This behavior is the inverse of that of the ensemble average and standard deviation of the k -eigenvalue. For fixed k_{∞} , the magnitude of the ensemble average scalar flux and standard deviation is not greatly impacted for the two smallest values of c^{fuel} , with a shift in the shape for the largest value of c^{fuel} . The shape shifts to a more highly peaked flux profile as indicated by a decrease in the minimum ensemble average flux and an increase in the maximum. The magnitude of the fast group scalar flux is greater than that of the thermal group. However, the relative standard deviation is much greater in the thermal group.

Fast Group Scalar Flux Results						
Calc.	$(\bar{\phi})_{min}$	$(\bar{\phi})_{max}$	$(\sigma)_{min}$	$(\sigma)_{max}$	$\left(\frac{\sigma_{\bar{\phi}_1}}{\bar{\phi}_1}\%\right)_{min}$	$\left(\frac{\sigma_{\bar{\phi}_1}}{\bar{\phi}_1}\%\right)_{max}$
2.1.1	3.7801	5.8019	0.5046	0.7577	13.06	13.44
2.1.2	2.3462	3.6353	0.2947	0.4555	12.52	12.77
2.1.3	1.7477	2.7239	0.2122	0.3290	12.06	12.47
2.2.1	3.6046	5.8600	0.4789	0.7782	13.28	13.55
2.2.2	2.2393	3.6726	0.2742	0.4698	12.20	12.80
2.2.3	1.6684	2.7520	0.1935	0.3402	11.56	12.37
2.3.1	2.8464	6.1327	0.4724	0.8903	14.51	17.87
2.3.2	1.7778	3.8146	0.2616	0.5409	13.75	16.09
2.3.3	1.3279	2.8769	0.1785	0.3934	13.14	15.11

Table 18: Fast Group Flux Results for Set 2; Disk-Markov Statistics, Vacuum Boundaries

Thermal Group Scalar Flux Results						
Calc.	$(\bar{\phi})_{min}$	$(\bar{\phi})_{max}$	$(\sigma)_{min}$	$(\sigma)_{max}$	$\left(\frac{\sigma_{\bar{\phi}_2}}{\bar{\phi}_2}\%\right)_{min}$	$\left(\frac{\sigma_{\bar{\phi}_2}}{\bar{\phi}_2}\%\right)_{max}$
2.1.1	0.1338	0.8141	0.0888	0.6997	60.69	88.21
2.1.2	0.1092	0.6707	0.0539	0.4738	46.09	73.49
2.1.3	0.0976	0.6113	0.0395	0.3804	38.28	65.63
2.2.1	0.1313	0.8204	0.0887	0.7040	61.84	89.12
2.2.2	0.1076	0.6750	0.0542	0.4759	47.04	74.08
2.2.3	0.0963	0.6147	0.0399	0.3817	39.14	66.06
2.3.1	0.1189	0.8472	0.0844	0.7234	65.46	91.12
2.3.2	0.0997	0.6928	0.0528	0.4855	49.86	74.73
2.3.3	0.0904	0.6286	0.0394	0.3880	41.67	66.16

Table 19: Thermal Group Flux Results for Set 2; Disk-Markov Statistics, Vacuum Boundaries

Representative plots of the group scalar flux (with $\pm 2\sigma$ confidence interval) and the atomic mix approximation are shown in Figures 35 - 38 for calculation 2.1.2 and calculation 2.3.2. [These are for an increasing value of c^{fuel} with constant k_∞ , since the introduction of more fast group scattering in the fuel results in an increasingly peaked shape of the fast and thermal scalar flux profiles.] The shape of the flux profile is independent of an increasing value of k_∞ for fixed c^{fuel} , only the magnitude is decreased.

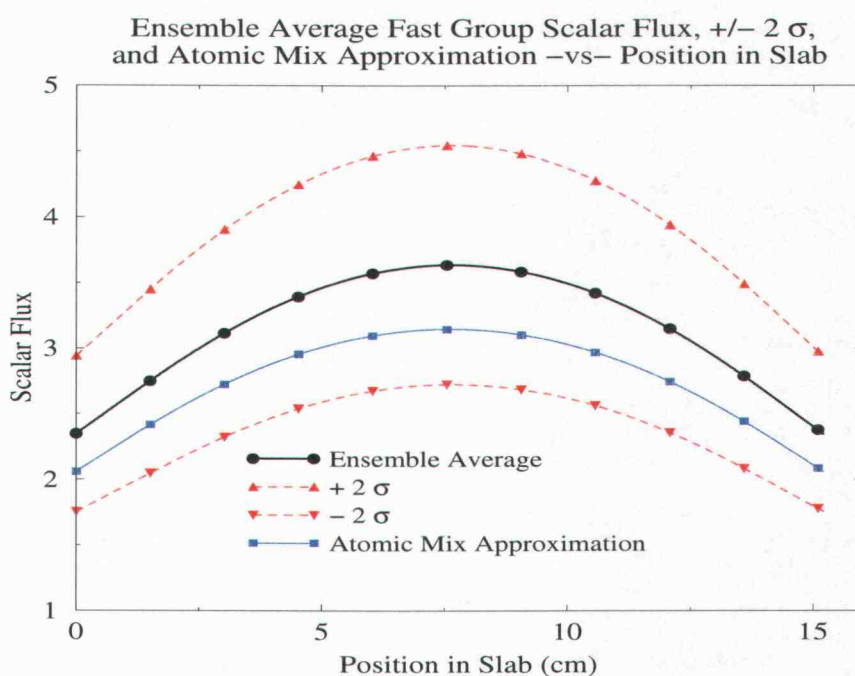


Figure 35: Ensemble Average Fast Group Flux - Calculation 2.1.2

The cosine shape of the flux profile is consistent with a symmetric homogeneous medium solution. Each realization may look very different (as in Figure 10) but this variability decreases with the averaging process. All of the fast and thermal flux profiles in Set 2 with vacuum boundaries have this characteristic cosine shape.

Another characteristic of the flux shape seen for all of the Set 2 calculations with

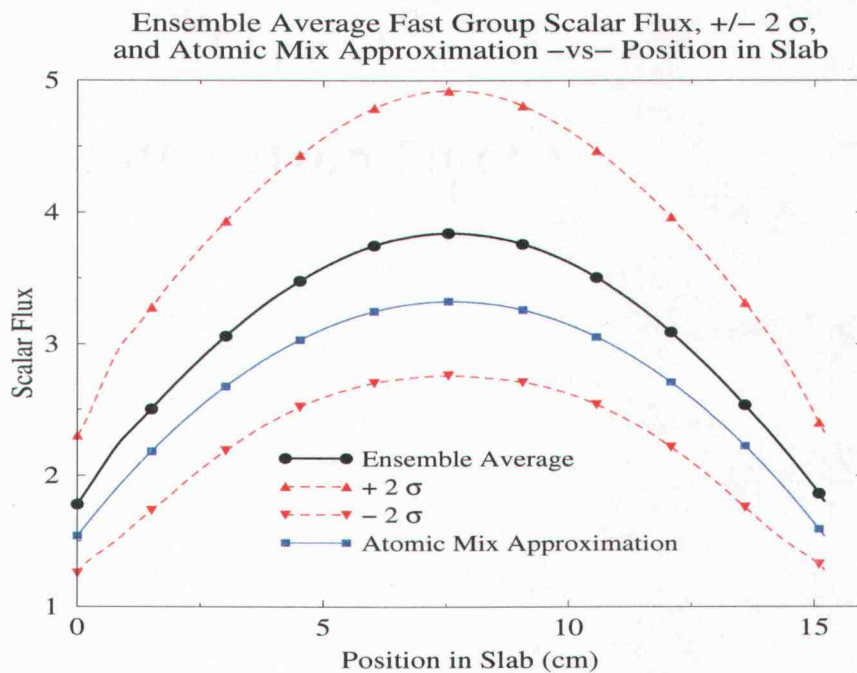


Figure 36: Ensemble Average Fast Group Flux - Calculation 2.3.2

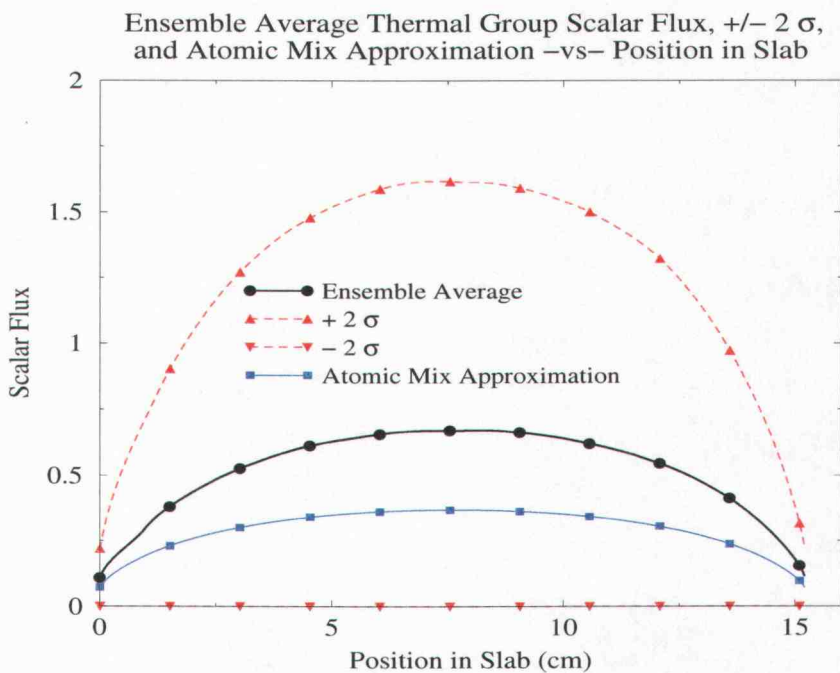


Figure 37: Ensemble Average Thermal Group Flux - Calculation 2.1.2

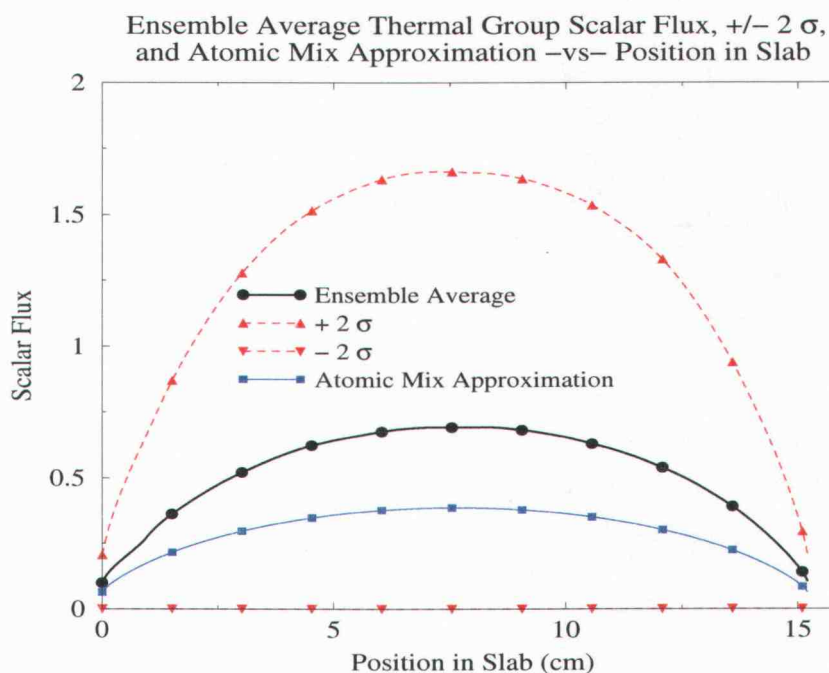


Figure 38: Ensemble Average Thermal Group Flux - Calculation 2.3.2

vacuum boundaries is the small asymmetric peak in the fast group and depression in the thermal group ensemble average scalar fluxes near the left-hand side of the system. This asymmetry is highlighted when investigating the material fluxes (averaged scalar flux solution in material α if material α resides at discrete spatial location i) shown in Figure 39.

This shows a distinct peak in the fast group fuel material (with corresponding depression in the moderator material) near the left-hand side of the system. This behavior is emphasized when using a constant segment size in the fuel material of the mean segment size used previously (Figure 40). This demonstrates an interesting characteristic of the system length population algorithm when using dissimilar distributions for each material type.

The flux profile takes on a more peaked curve as c^{fuel} increases. The standard

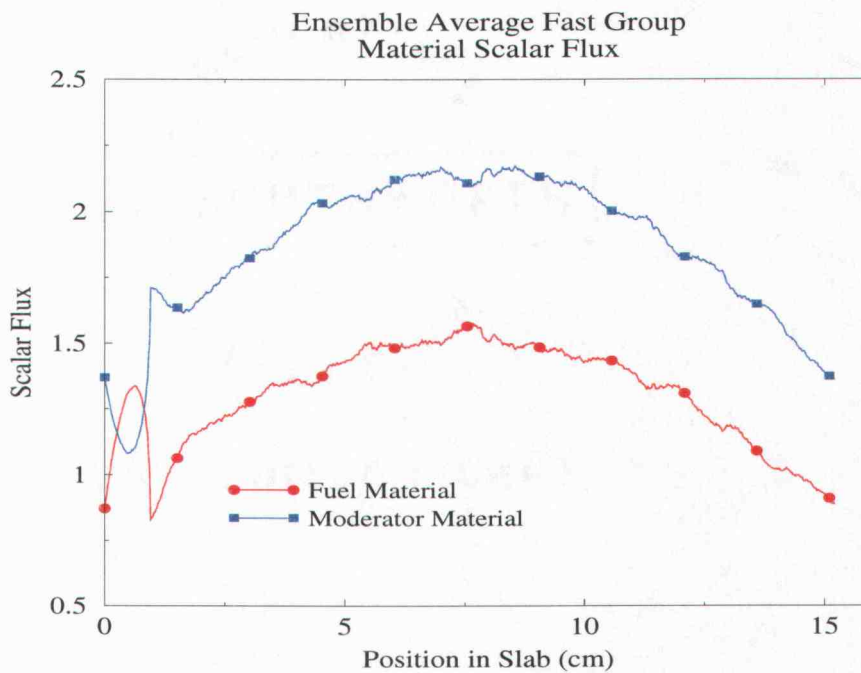


Figure 39: Fast Group Material Average Scalar Flux - Calculation 2.2.2

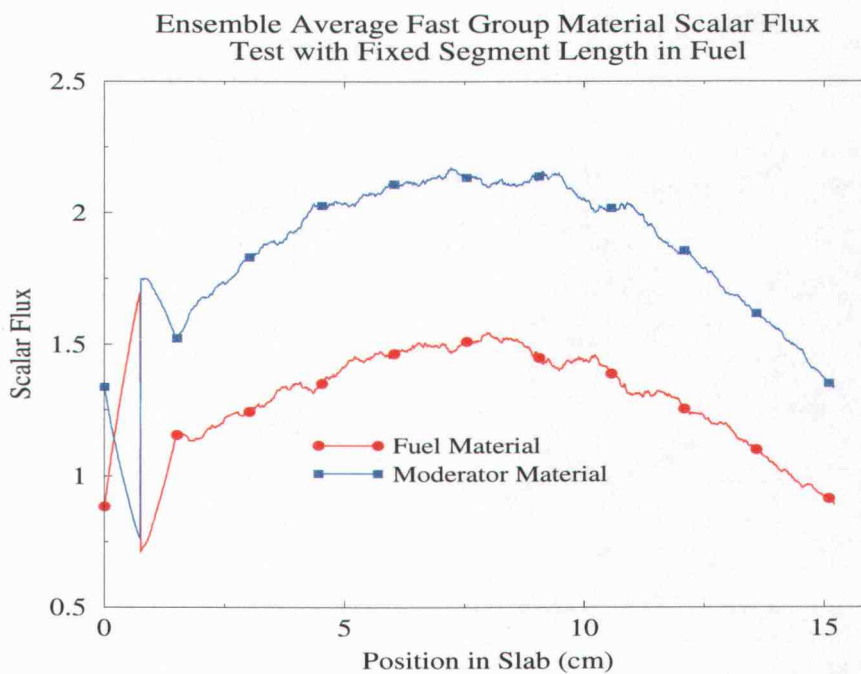


Figure 40: Fast Group Material Average Scalar Flux with Fixed Fuel Segment Length - Calculation 2.2.2

deviation broadens in the fast group as c^{fuel} increases. The fast group standard deviation is smaller than that of the thermal group. The standard deviation in the thermal group increases only slightly with an increase in c^{fuel} .

4.6.3 The Atomic Mix Approximation

A comparison of atomic mix predictions of the ensemble average k-eigenvalue is given below in Table 20. Atomic mix yields conservative estimates of \bar{k} , with

Atomic Mix k-Eigenvalue Comparison			
Calc.	k	$k_{a.m.}$	%R.E.
2.1.1	0.2057	0.2301	11.85
2.1.2	0.3298	0.3729	13.07
2.1.3	0.4414	0.5026	13.85
2.2.1	0.2051	0.2292	11.79
2.2.2	0.3285	0.3718	13.19
2.2.3	0.4394	0.5013	14.08
2.3.1	0.2127	0.2388	12.29
2.3.2	0.3395	0.3884	14.41
2.3.3	0.4533	0.5245	15.71

Table 20: Atomic Mix Prediction of the Ensemble Average k-Eigenvalue for Set 2; Disk-Markov Statistics, Vacuum Boundaries

the relative error ranging between $\approx 12 - 16\%$. The atomic mix prediction of \bar{k} always is contained in the 2σ confidence interval, but always lies outside of the 1σ confidence interval. The difference between the atomic mix and benchmark \bar{k} increases with increasing k_∞ and only slightly (if at all) with c^{fuel} .

For all of the calculations considered, atomic mix under-predicts the magnitude of the flux in both energy groups. This can be seen in Figures 35 - 38 for calculation 2.1.2 and calculation 2.3.2. A comparison of atomic mix predictions of fast and thermal group scalar fluxes is given below in Table 21.

Atomic Mix Group Scalar Flux Comparison				
Calc.	$\left(\frac{\bar{\phi}_1}{\phi_{1,a.m.}}\right)_{min} \%$	$\left(\frac{\bar{\phi}_1}{\phi_{1,a.m.}}\right)_{max} \%$	$\left(\frac{\bar{\phi}_2}{\phi_{2,a.m.}}\right)_{min} \%$	$\left(\frac{\bar{\phi}_2}{\phi_{2,a.m.}}\right)_{max} \%$
2.1.1	1.1249	1.1475	1.6670	2.2855
2.1.2	1.1370	1.1559	1.4620	1.8280
2.1.3	1.1446	1.1610	1.3479	1.6320
2.2.1	1.1230	1.1469	1.6798	2.2829
2.2.2	1.1377	1.1557	1.4710	1.8250
2.2.3	1.1465	1.1609	1.3557	1.6291
2.3.1	1.1174	1.1479	1.7334	2.2664
2.3.2	1.1384	1.1721	1.4978	1.8101
2.3.3	1.1505	1.1865	1.3788	1.6164

Table 21: Benchmark / Atomic Mix Ratio of Group Scalar Flux Solutions for Set 2; Disk-Markov Statistics, Vacuum Boundaries

The underestimation of the atomic mix approximation is evident, since all of the ratios are greater than unity. The atomic mix approximation is a fair predictor of the flux shape in the fast group: the maximum and minimum difference in the ratio vary between $\approx 1 - 3\%$. The atomic mix approximation of the thermal group scalar flux shape differs more significantly: the maximum and minimum ratios vary between $\approx 17 - 37\%$. For relatively flat flux profiles, atomic mix predicts the flux shape fairly well.

4.7 Disk-Markov Mixing Statistics - Reflecting Boundaries

In this section, Set 2 calculations are again considered, but with reflecting boundaries to assess the effect of leakage on ensemble quantities. The calculation designation is reduced to “calculation x.z”, where only $x = 2$ is considered in this section.

4.7.1 The k -Eigenvalue

The k -eigenvalue data is given in Table 22 below. A trend similar to that of the

Ensemble k -Eigenvalue Results			
Calc.	\bar{k}	$\sigma_{\bar{k}}$	$(\frac{\sigma_{\bar{k}}}{\bar{k}}\%)$
2.1	0.6267	0.06008	9.59
2.2	1.0527	0.09603	9.12
2.3	1.4654	0.12765	8.71

Table 22: k -Eigenvalue Results for Set 2; Disk-Markov Statistics, Reflecting Boundaries

vacuum boundary case is discovered. There is a non-linear increase in the ensemble average k -eigenvalue as k_{∞} increases. A similar trend is present in the standard deviation.

The k -eigenvalue probability distribution functions for these three calculations are shown in Figures 41 - 43 below. These k -eigenvalue PDFs resemble a skewed Gaussian distribution with a truncation of the tail on the right-hand side. All three plots show a similar relative standard deviation.

Figure 44 shows that an increase in k_{∞} increases the range of possible k -eigenvalues, with a shift toward larger k -eigenvalues. The shape of the k -eigenvalue PDF is not greatly impacted by a change in k_{∞} .

4.7.2 Scalar Flux

Tables 23 - 24 give results for the fast and thermal group scalar flux, respectively. As shown in the example flux plots below (Figures 45 - 48), all of the Set 2 solutions with reflecting boundaries have a relatively flat shape. The minimum and maximum of these quantities illustrate the effect of the variable parameters

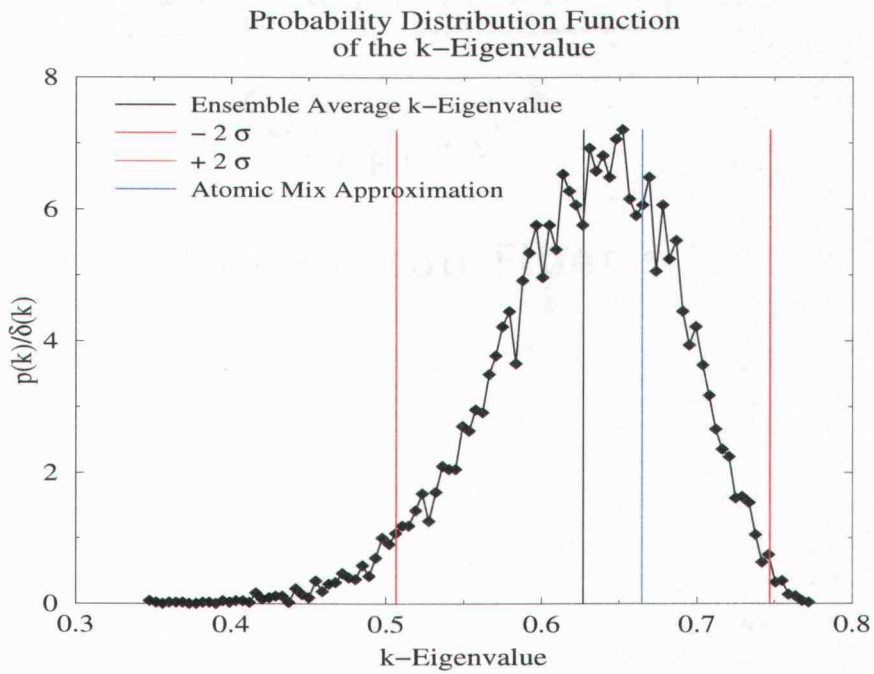


Figure 41: k-Eigenvalue PDF - Calculation 2.1

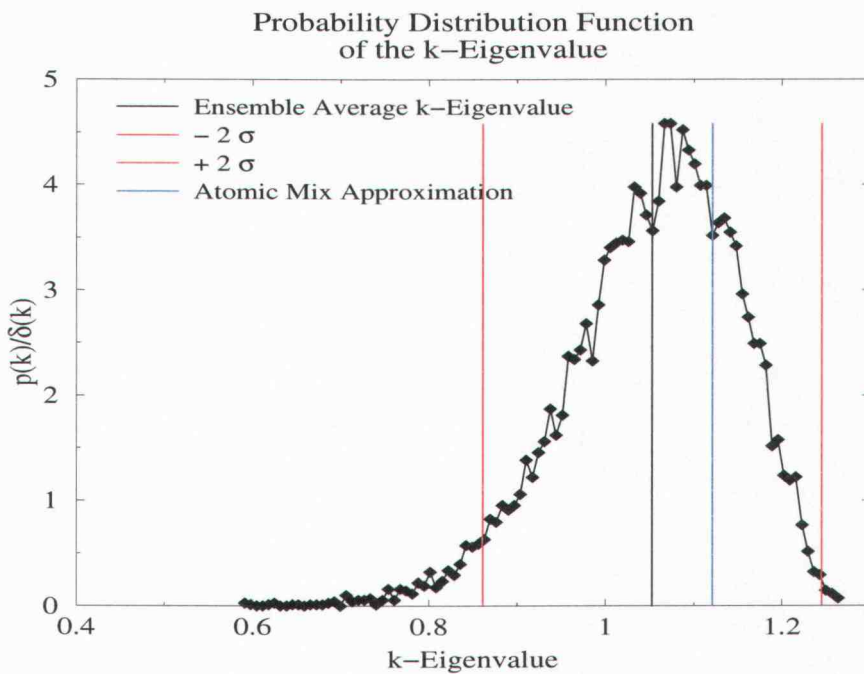
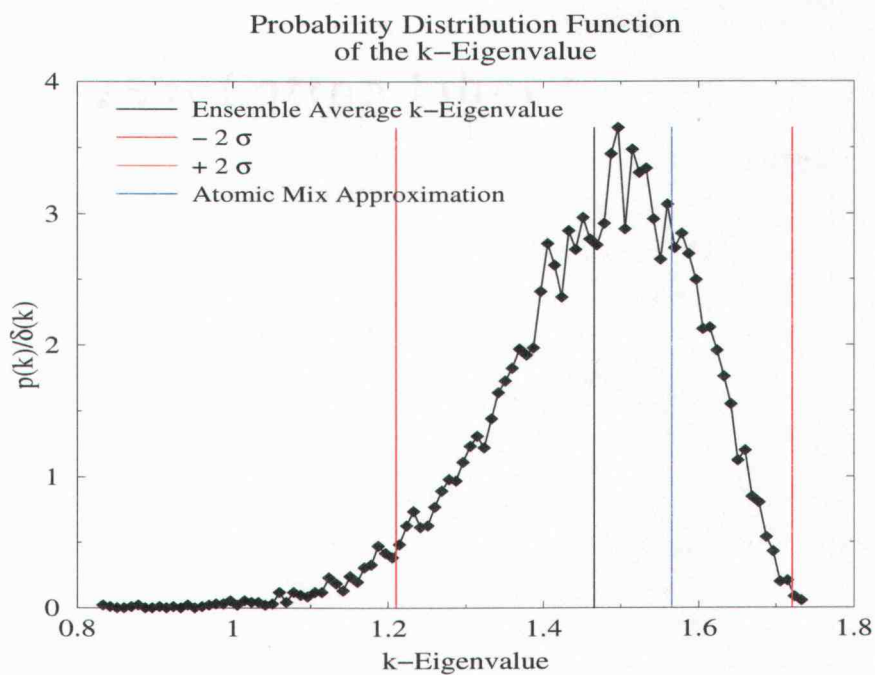
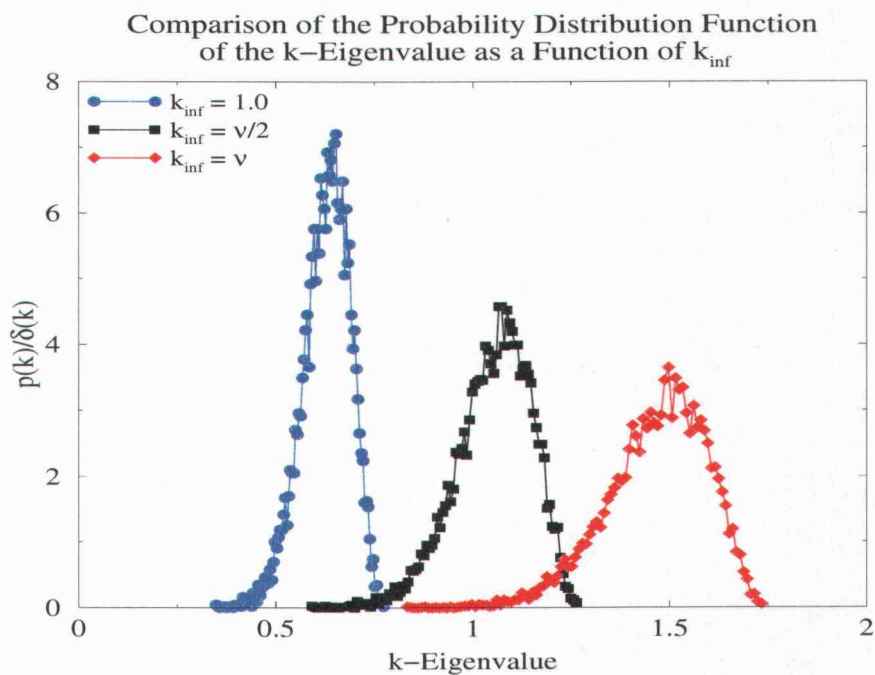


Figure 42: k-Eigenvalue PDF - Calculation 2.2

Figure 43: k -Eigenvalue PDF - Calculation 2.3Figure 44: k -Eigenvalue PDF - Calculation 2.1 - Calculation 2.3

on the shape of these two solutions. Similar maxima and minima designate a flat profile, while dissimilar maxima and minima indicate a peaked flux profile.

Tables 13 - 14 give results for the fast and thermal group scalar flux, respectively. These results reveal that as k_∞ increases the group ensemble average scalar flux and standard deviation decreases. This is the inverse behavior of the ensemble average and standard deviation of the k-eigenvalue. The standard deviation decreases by a slightly greater factor than the ensemble average flux for increasing k_∞ . Therefore, the relative standard deviation decreases as a function of increasing k_∞ . The magnitude of the fast group scalar flux is greater than that of the thermal group. However, the relative standard deviation is much larger in the thermal group.

Fast Group Flux Results						
Calc.	$(\bar{\phi}_1)_{min}$	$(\bar{\phi}_1)_{max}$	$(\sigma_{\bar{\phi}_1})_{min}$	$(\sigma_{\bar{\phi}_1})_{max}$	$\left(\frac{\sigma_{\bar{\phi}_1}}{\bar{\phi}_1}\%\right)_{min}$	$\left(\frac{\sigma_{\bar{\phi}_1}}{\bar{\phi}_1}\%\right)_{max}$
2.1	4.4053	4.4537	0.5832	0.5957	13.12	13.46
2.2	2.6246	2.6485	0.3337	0.3411	12.64	12.95
2.3	1.8862	1.9007	0.2311	0.2365	12.19	12.51

Table 23: Fast Group Flux Results for Set 1; Disk-Markov Statistics, Reflecting Boundaries

Thermal Group Flux Results						
Calc.	$(\bar{\phi}_2)_{min}$	$(\bar{\phi}_2)_{max}$	$(\sigma_{\bar{\phi}_2})_{min}$	$(\sigma_{\bar{\phi}_2})_{max}$	$\left(\frac{\sigma_{\bar{\phi}_2}}{\bar{\phi}_2}\%\right)_{min}$	$\left(\frac{\sigma_{\bar{\phi}_2}}{\bar{\phi}_2}\%\right)_{max}$
2.1	0.6655	0.8584	0.5953	1.0956	89.17	141.58
2.2	0.5345	0.6529	0.3839	0.6818	71.68	116.54
2.3	0.4781	0.5643	0.2957	0.5093	61.75	100.62

Table 24: Thermal Group Flux Results for Set 1; Disk-Markov Statistics, Reflecting Boundaries

Representative plots are given for the group scalar fluxes (including the $\pm 2\sigma$

confidence interval) and the atomic mix approximation in Figures 45 - 48 for calculation 2.1 and calculation 2.3.

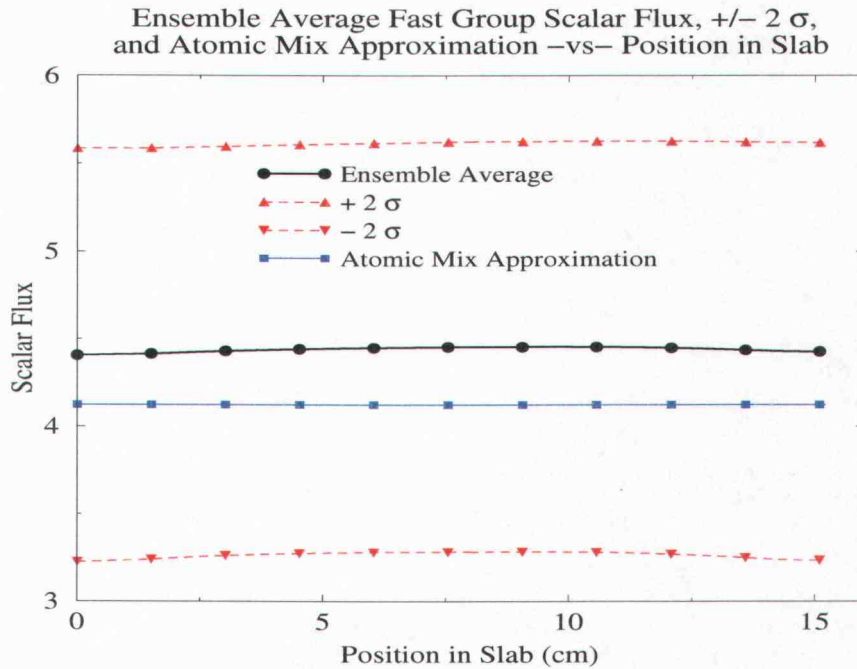


Figure 45: Ensemble Average Fast Group Flux - Calculation 2.1

These solutions show flat flux profiles, consistent with solutions of a homogeneous infinite medium. [Each realization may look very different but this variability decreases with the averaging process.] As in the vacuum boundary case, the flux profile for all of the Set 2 calculations with reflecting boundaries has a small asymmetric peak in the fast group, and depression in the thermal group ensemble average scalar fluxes near the left-hand side of the system.

4.7.3 The Atomic Mix Approximation

A comparison of the atomic mix prediction of ensemble average k -eigenvalue is given below in Table 25. This approximation yields conservative estimates of \bar{k}

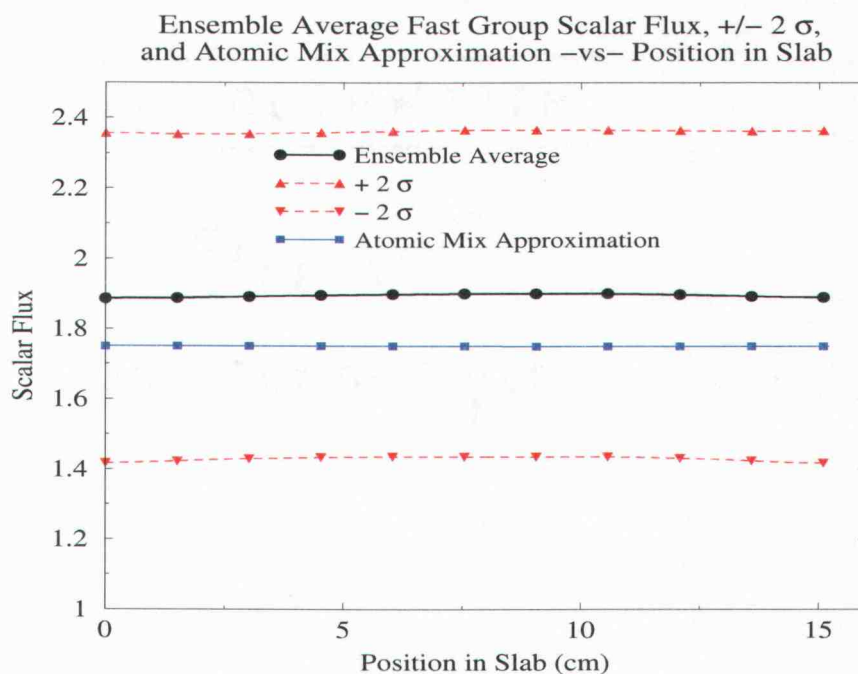


Figure 46: Ensemble Average Fast Group Flux - Calculation 2.3

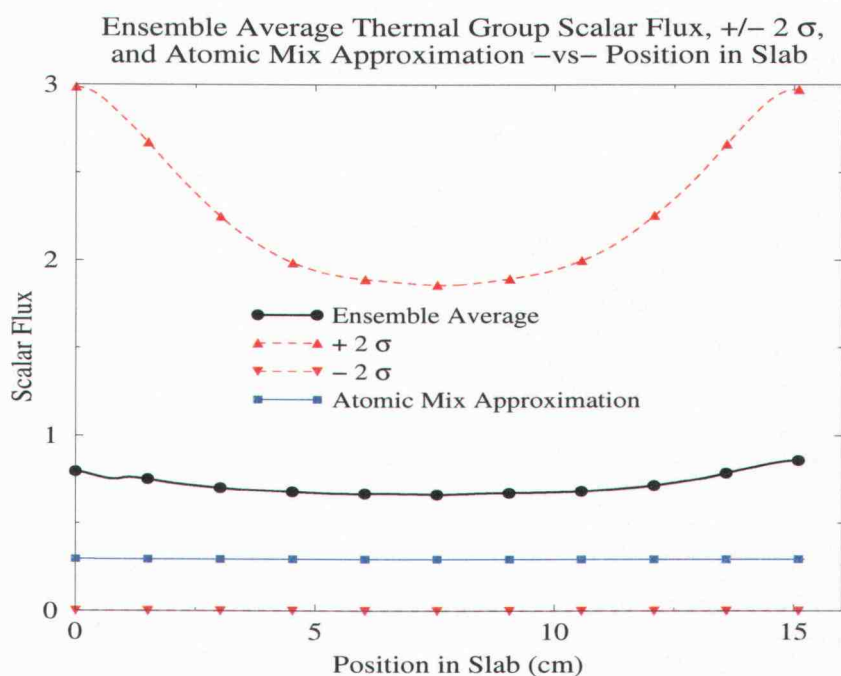


Figure 47: Ensemble Average Thermal Group Flux - Calculation 2.1

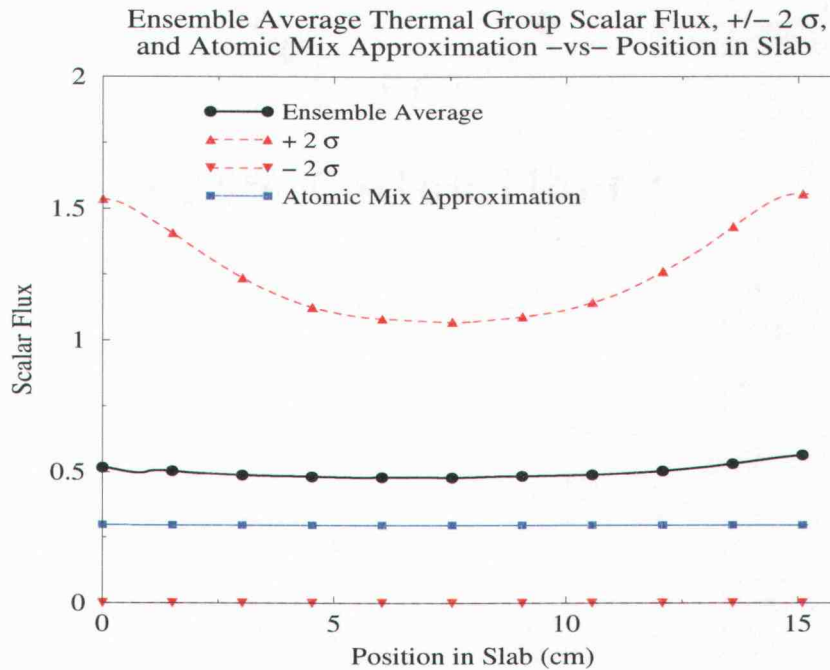


Figure 48: Ensemble Average Thermal Group Flux - Calculation 2.3

with relative errors ranging between $\approx 6 - 7\%$. The atomic mix prediction of \bar{k} always is contained in the σ confidence interval.

Atomic Mix k-Eigenvalue Comparison			
Calc.	\bar{k}	$k_{a.m.}$	%R.E.
2.1	0.6267	0.6646	6.04
2.2	1.0527	1.1209	6.48
2.3	1.4654	1.5653	6.82

Table 25: Atomic Mix Prediction of the Ensemble Average k-Eigenvalue for Set 2; Disk-Markov Statistics, Reflecting Boundaries

For all of the calculations considered, atomic mix under-predicts the magnitude of the flux in both energy groups. This is evident in the representative plots of Figures 45 - 48 for calculation 2.1 and calculation 2.3.

A comparison of the atomic mix prediction of the fast and thermal group scalar

fluxes is given below in Table 26. The underestimation of the atomic mix approx-

Atomic Mix Group Scalar Flux Comparison				
Calc.	$\left(\frac{\bar{\phi}_1}{\phi_{1,a.m.}}\right)_{min} \%$	$\left(\frac{\bar{\phi}_1}{\phi_{1,a.m.}}\right)_{max} \%$	$\left(\frac{\bar{\phi}_2}{\phi_{2,a.m.}}\right)_{min} \%$	$\left(\frac{\bar{\phi}_2}{\phi_{2,a.m.}}\right)_{max} \%$
2.1	1.0687	1.0805	2.2452	2.8964
2.2	1.0739	1.0838	1.8032	2.2032
2.3	1.0777	1.0861	1.6128	1.9047

Table 26: Ensemble Average / Atomic Mix Ratio of Group Scalar Flux Solutions for Set 2; Disk-Markov Statistics, Reflecting Boundaries

imation is evident, since all of the ratios are greater than unity. The atomic mix approximation is again a fair predictor of the flux shape in the fast group: the maximum and minimum difference in the ratio vary between $\approx 0.8 - 1\%$. The atomic mix approximation of the thermal group scalar flux shape differs more significantly: the maximum and minimum ratios vary between $\approx 18 - 29\%$. For relatively flat flux profiles, atomic mix will predict the flux shape fairly well.

4.8 Disk-Matrix Mixing Statistics - Vacuum Boundaries

The final set of results considered are those for Set 3: the Disk segment length distribution in the fuel material and the Matrix segment length distribution in the moderator material, with vacuum boundaries.

4.8.1 The k -Eigenvalue

In this section, only calculations denoted by $x = 3$ are discussed. Table 27 shows the k -eigenvalue data from the nine vacuum boundary calculations performed with the fuel segment lengths governed by the Disk distribution, and the Matrix segment length distribution in the moderator material.

Ensemble k-Eigenvalue Results			
Calc.	k	$\sigma_{\bar{k}}$	$(\frac{\sigma_{\bar{k}}}{\bar{k}}\%)$
3.1.1	0.1937	0.02429	12.54
3.1.2	0.3109	0.03945	12.69
3.1.3	0.4165	0.05377	12.91
3.2.1	0.1929	0.02477	12.84
3.2.2	0.3094	0.04004	12.94
3.2.3	0.4144	0.05437	13.12
3.3.1	0.2004	0.02815	14.05
3.3.2	0.3206	0.04533	14.14
3.3.3	0.4288	0.06133	14.31

Table 27: k-Eigenvalue Results for Set 3; Disk-Matrix Statistics, Vacuum Boundaries

The increase in \bar{k} as a function of increased k_{∞} for a fixed c^{fuel} reflects the greater probability of fission occurring when neutrons are absorbed in the fuel material. This is again not a linear increase. As k_{∞} is increased from 1 to $\nu/2$ (a factor of ≈ 1.21) \bar{k} increases a factor of ≈ 1.6 . k_{∞} is increase from $\nu/2$ to ν (a factor of 2) yielding only another factor of ≈ 1.3 .

An increase in c^{fuel} with fixed k_{∞} does not significantly impact the value of \bar{k} or the standard deviation for the two smallest values of c^{fuel} (0.1 and 0.5). There is a small but noticeable increase in these two quantities for the largest value of c^{fuel} (0.9).

With the increase in k_{∞} there is a corresponding increase in the standard deviation of the k-eigenvalue. This increase is larger than the increase in \bar{k} , resulting in an increasing relative standard deviation as a function of increasing k_{∞} for a fixed c^{fuel} .

Three examples of the k-eigenvalue PDF are shown in Figures 49 - 51, which were generated for calculations 3.3.1 - 3.3.3.

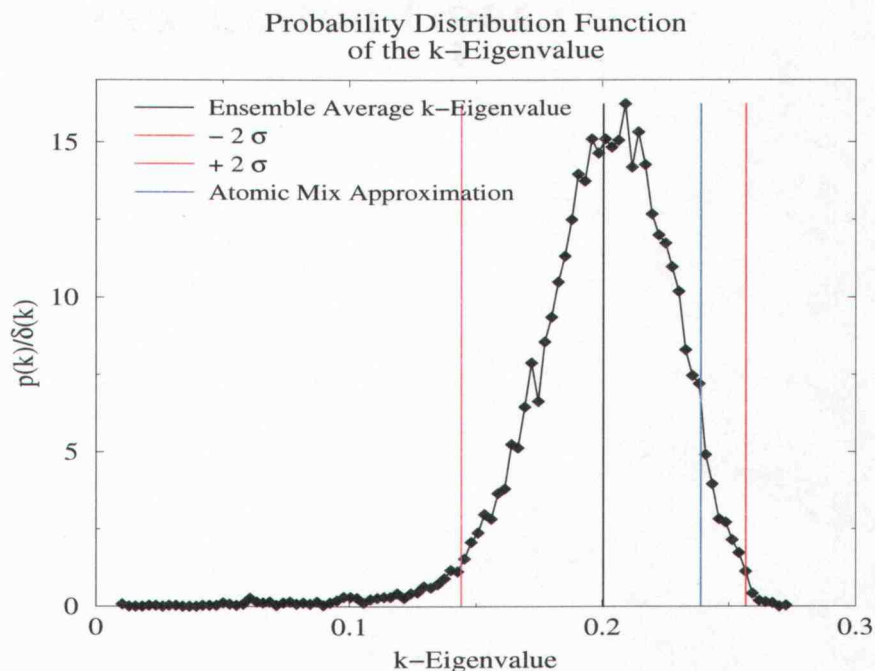


Figure 49: k-Eigenvalue PDF - Calculation 3.3.1

The shape of the k-eigenvalue PDFs resemble a skewed Gaussian distribution with a truncation of the tail on the right-hand side, and a long tail on the left-hand side. There is a noticeable and expected shift in the k-eigenvalue PDF toward larger k-eigenvalues for increasing k_∞ . The relative standard deviation is nearly constant as a function of increasing k_∞ , which can be seen in the consistent size of the $\pm 2\sigma$ width about the mean.

Figure 52 shows how increasing k_∞ widens the range of possible k-eigenvalues, with a shift toward larger k-eigenvalues. An increase in c^{fuel} causes a small broadening of the k-eigenvalue PDF for the largest value of c^{fuel} . This effect is shown for calculations 3.1.3, 3.2.3, and 3.3.3 in Figure 53 below. The PDF of the k-eigenvalue is very similar as a function of increasing c^{fuel} with constant k_∞ . The overall shape is not greatly impacted by either a change in k_∞ or c^{fuel} .

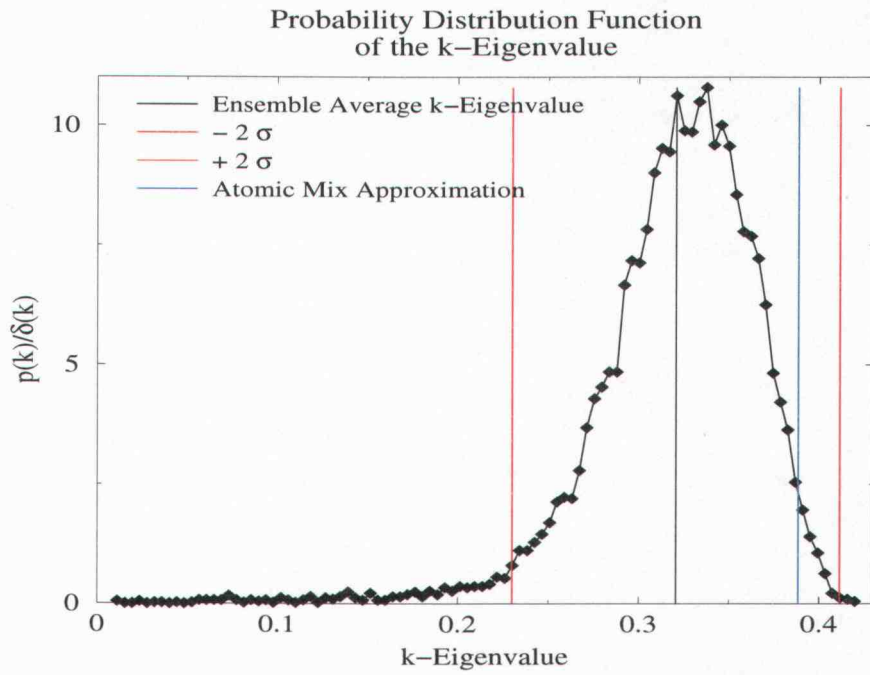


Figure 50: k-Eigenvalue PDF - Calculation 3.3.2

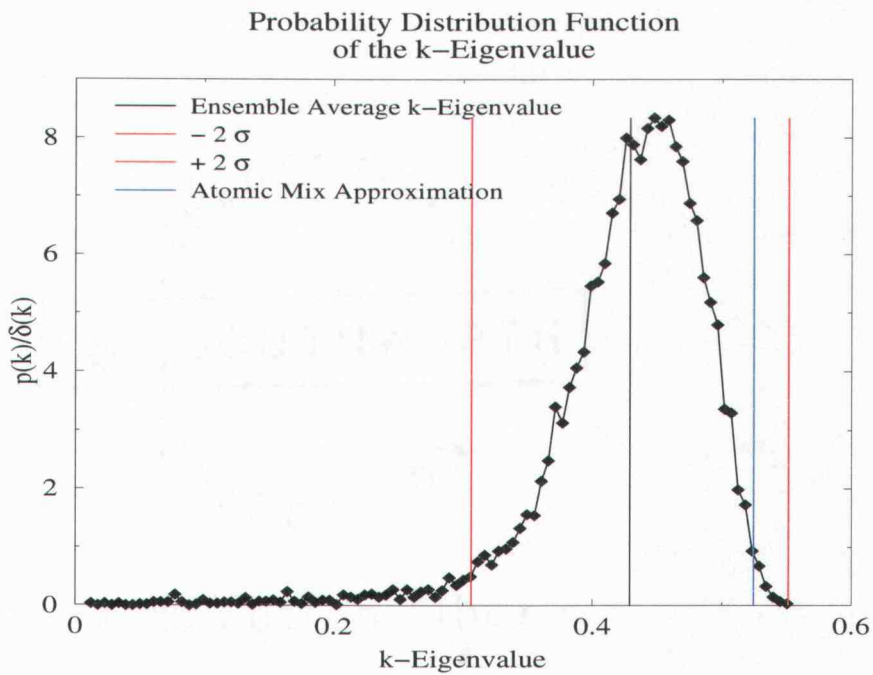


Figure 51: k-Eigenvalue PDF - Calculation 3.3.3

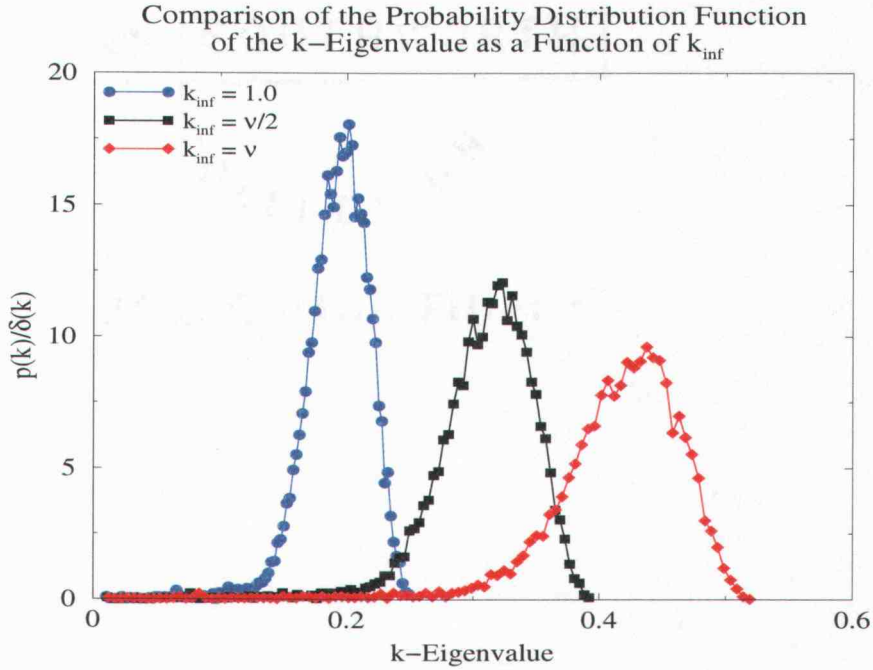
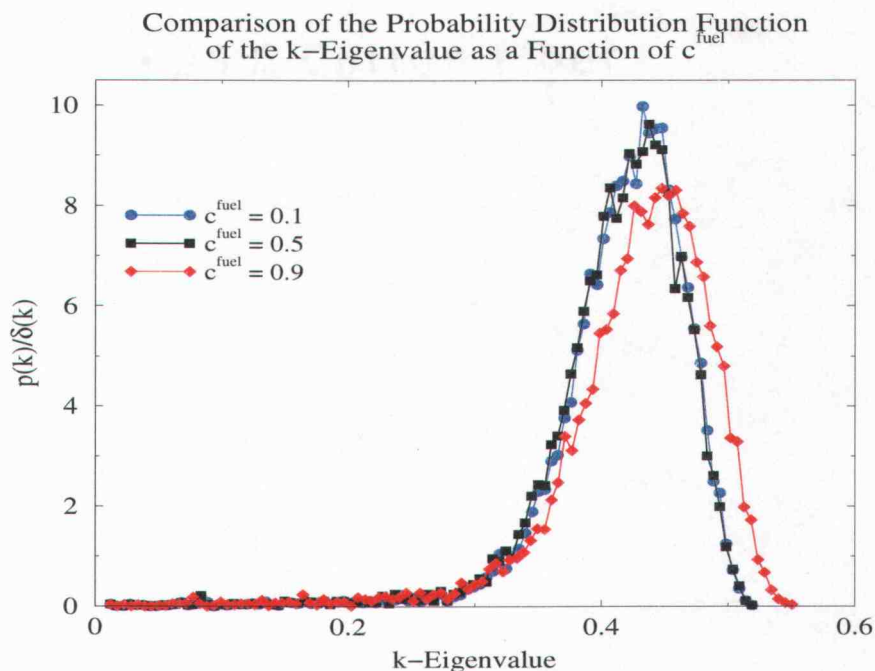


Figure 52: k -Eigenvalue PDF - Calculation 3.2.1 - Calculation 3.2.3

4.8.2 Scalar Flux

Table 28 and 29 give results for the fast and thermal group scalar flux, respectively. In Figures 54 - 57 it is observed that all of the Set 3 ensemble average solutions with vacuum boundaries have a slightly asymmetric cosine shape. The minimum and maximum of these quantities illustrate the effect of the variable parameters on the shape of these two solutions.

These results reveal that as k_{∞} increases, the group ensemble average scalar flux and standard deviation decreases for fixed c^{fuel} , while the relative standard deviation increases. This behavior is the inverse of that of the ensemble average and standard deviation of the k -eigenvalue. For fixed k_{∞} , the magnitude of the ensemble average scalar flux and standard deviation is not greatly impacted for the two smallest values of c^{fuel} , with a shift in the shape for the largest value of c^{fuel} .

Figure 53: k -Eigenvalue PDF - Calculation 3.1.3 - Calculation 3.3.3

Fast Group Scalar Flux Results						
Calc.	$(\bar{\phi})_{min}$	$(\bar{\phi})_{max}$	$(\sigma)_{min}$	$(\sigma)_{max}$	$\left(\frac{\sigma_{\phi_1}}{\phi_1}\right)_{min} \%$	$\left(\frac{\sigma_{\phi_1}}{\phi_1}\right)_{max} \%$
3.1.1	4.0214	6.1280	1.2283	2.6288	20.17	61.30
3.1.2	2.5193	3.8476	1.0511	2.4253	27.49	89.81
3.1.3	1.8933	2.8911	1.0048	2.3492	34.97	115.25
3.2.1	3.8517	6.1926	1.2439	2.6127	20.21	63.98
3.2.2	2.4154	3.8882	1.0589	2.4184	27.40	93.88
3.2.3	1.8163	2.9213	1.0101	2.3451	34.79	120.49
3.3.1	3.1014	6.4879	1.3308	2.6250	20.70	79.55
3.3.2	1.9581	4.0686	1.1100	2.4056	27.48	116.76
3.3.3	1.4790	3.0538	1.0481	2.3375	34.56	149.51

Table 28: Fast Group Flux Results for Set 3; Disk-Matrix Statistics, Vacuum Boundaries

Thermal Group Scalar Flux Results						
Calc.	$(\bar{\phi})_{min}$	$(\bar{\phi})_{max}$	$(\sigma)_{min}$	$(\sigma)_{max}$	$\left(\frac{\sigma_{\phi_2}}{\phi_2}\%\right)_{min}$	$\left(\frac{\sigma_{\phi_2}}{\phi_2}\%\right)_{max}$
3.1.1	0.1437	1.2886	0.2918	3.2816	154.81	290.80
3.1.2	0.1220	1.0079	0.2664	2.8459	175.44	329.23
3.1.3	0.1119	0.8918	0.2601	2.6855	193.02	354.40
3.2.1	0.1412	1.2981	0.2937	3.2937	157.57	291.99
3.2.2	0.1204	1.0141	0.2675	2.8542	177.92	330.59
3.2.3	0.1106	0.8967	0.2609	2.6925	195.36	356.27
3.3.1	0.1297	1.3406	0.2991	3.3765	172.98	303.56
3.3.2	0.1131	1.0429	0.2731	2.9154	191.94	345.07
3.3.3	0.1051	0.9199	0.2653	2.7463	208.55	372.11

Table 29: Thermal Group Flux Results for Set 3; Disk-Matrix Statistics, Vacuum Boundaries

The shape shifts to a more highly peaked flux profile as indicated by a decrease in the minimum ensemble average flux and an increase in the maximum. The magnitude of the fast group scalar flux is greater than that of the thermal group. However, the relative standard deviation is much greater in the thermal group.

Representative plots of the group scalar flux (with $\pm 2\sigma$ confidence interval) and the atomic mix approximation are shown in Figures 54 - 57 for calculation 3.1.3 and calculation 3.3.3. [These are for an increasing value of c^{fuel} with constant k_∞ , since the introduction of more fast group scattering in the fuel results in a increasingly peaked shape of the fast and thermal scalar flux profiles.] The shape of the flux profile is independent of an increasing value of k_∞ for fixed c^{fuel} , only the magnitude is decreased.

The cosine shape of the flux profile is similar to a symmetric homogeneous medium solution. Each realization may look very different (as in Figure 10) but this variability decreases with the averaging process. An asymmetry is noticeable in the flux profile with a shift in the peak toward the left-hand side of the system in

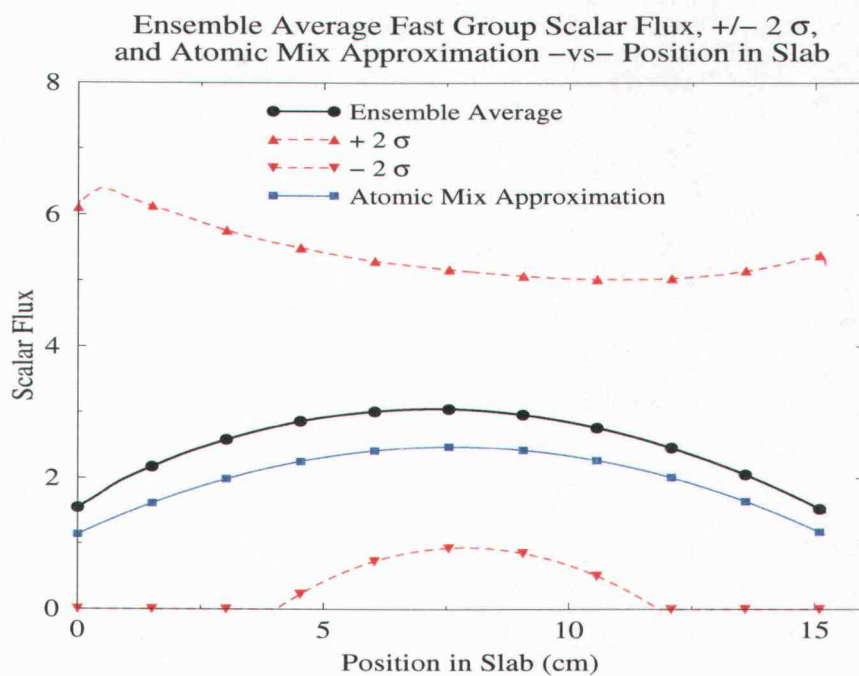


Figure 54: Ensemble Average Fast Group Flux - Calculation 3.1.3

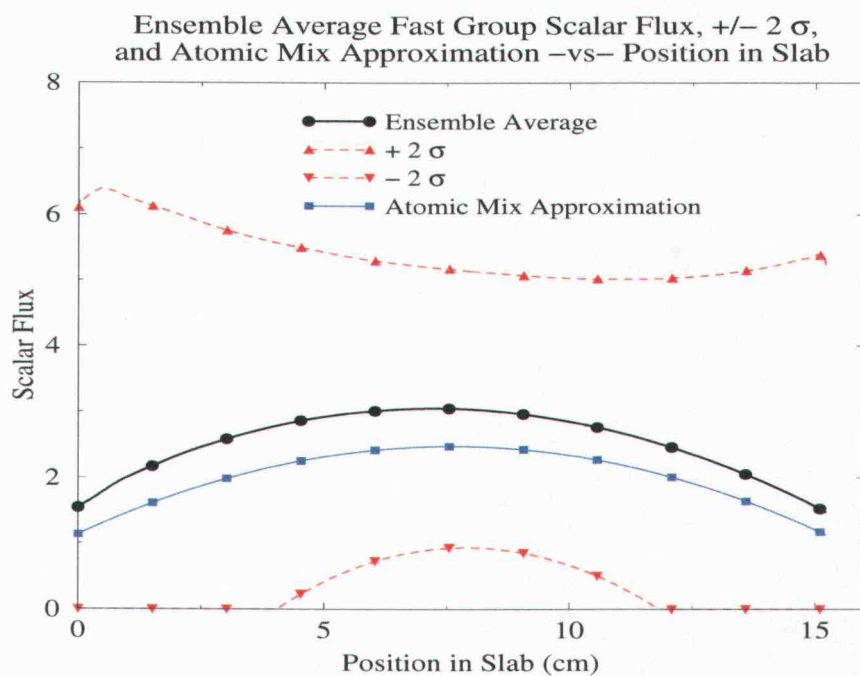


Figure 55: Ensemble Average Fast Group Flux - Calculation 3.3.3

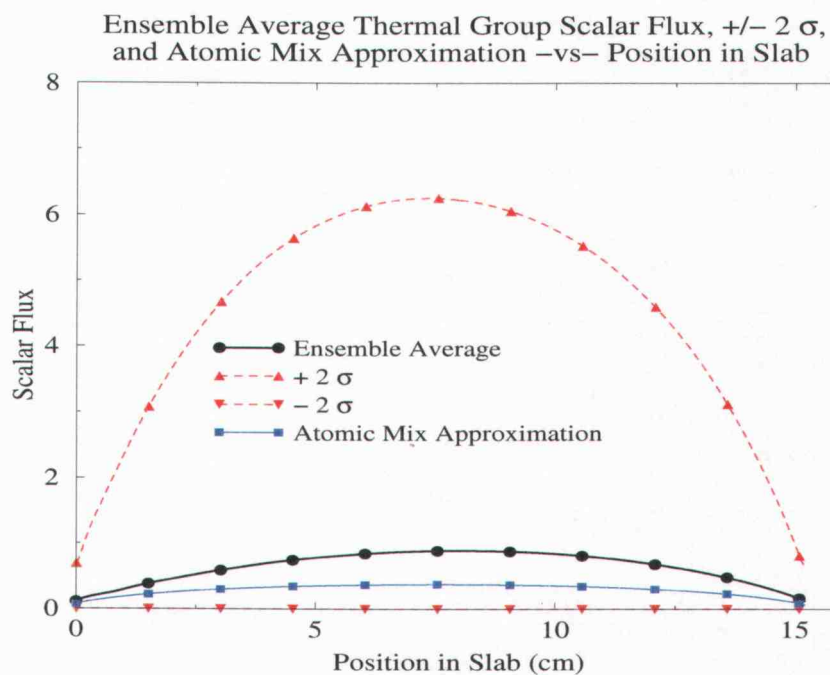


Figure 56: Ensemble Average Thermal Group Flux - Calculation 3.1.3

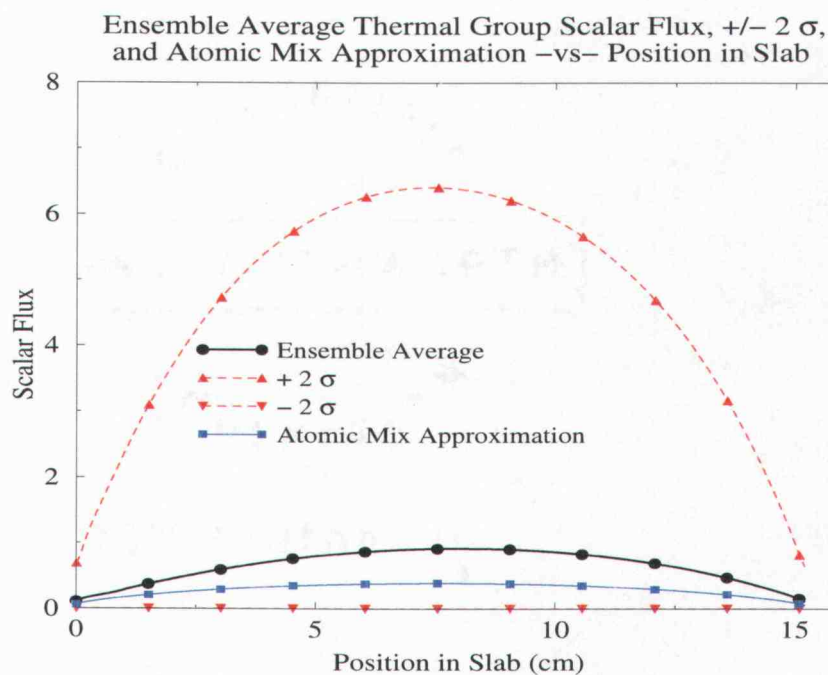


Figure 57: Ensemble Average Thermal Group Flux - Calculation 3.3.3

the fast group and a shift in the peak toward to the right-hand side in the thermal group. All of the fast and thermal flux profiles in Set 3 with vacuum boundaries have this characteristic cosine shape.

As in the Set 2 calculations there is the small asymmetric peak in the fast group and depression in the thermal group ensemble average scalar fluxes near the left-hand side of the system. This asymmetry is emphasized when investigating the material fluxes (averaged scalar flux solution in material α if material α resides at discrete spatial location i) shown in Figure 58. This shows a distinct peak in the fast group fuel material (with corresponding depression in the moderator material) near the left-hand side of the system. The flux profile takes on a more peaked curve as c^{fuel} increases. The relative standard deviation broadens in the fast group and thermal group as c^{fuel} increases. The fast group relative standard deviation is smaller than that of the thermal group.

4.8.3 *The Atomic Mix Approximation*

A comparison of atomic mix predictions of the ensemble average k-eigenvalue is given below in Table 30. Atomic mix yields conservative estimates of \bar{k} , with the relative error ranging between $\approx 19 - 22\%$. The atomic mix prediction of \bar{k} always is contained in the 2σ confidence interval, but always lies outside of the 1σ confidence interval. The difference between the atomic mix and benchmark \bar{k} increases slightly with increasing k_∞ and c^{fuel} .

For all of the calculations considered, atomic mix under-predicts the magnitude of the flux in both energy groups. This can be seen in Figures 54 - 57 for calculation 3.1.3 and calculation 3.3.3. A comparison of atomic mix predictions of fast and thermal group scalar fluxes is given below in Table 31.

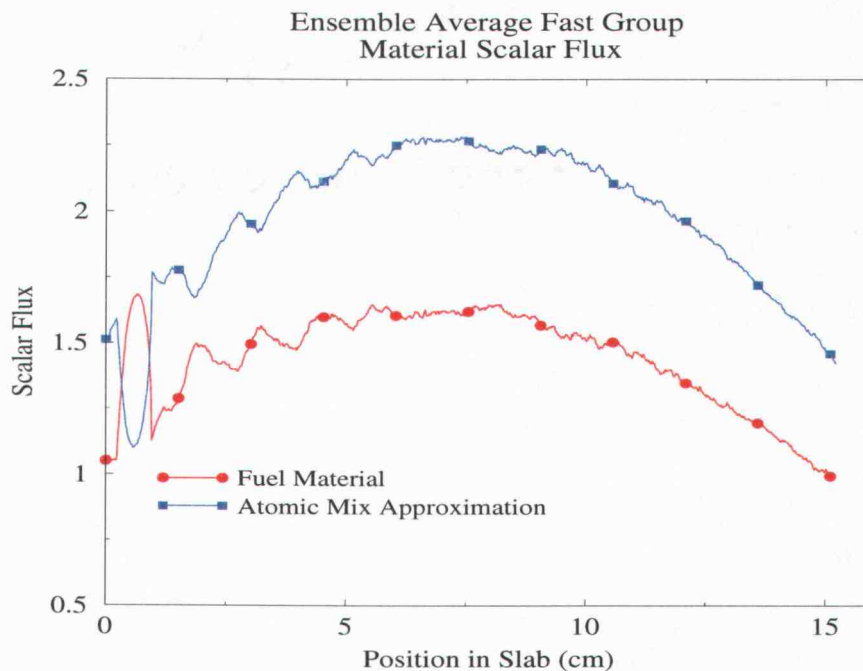


Figure 58: Fast Group Material Average Scalar Flux - Calculation 3.2.2

Atomic Mix k-Eigenvalue Comparison			
Calc.	k	$k_{a.m.}$	%R.E.
3.1.1	0.1937	0.2301	18.81
3.1.2	0.3109	0.3729	19.96
3.1.3	0.4165	0.5026	20.65
3.2.1	0.1929	0.2292	18.85
3.2.2	0.3094	0.3718	20.16
3.2.3	0.4144	0.5013	20.96
3.3.1	0.2004	0.2388	19.16
3.3.2	0.3206	0.3884	21.15
3.3.3	0.4288	0.5245	22.32

Table 30: Atomic Mix Prediction of the Ensemble Average k-Eigenvalue for Set 3; Disk-Matrix Statistics, Vacuum Boundaries

Atomic Mix Group Scalar Flux Comparison				
Calc.	$\left(\frac{\sigma_{\phi_1}}{\phi_{1,a.m.}}\right)_{min} \%$	$\left(\frac{\bar{\phi}_1}{\phi_{1,a.m.}}\right)_{max} \%$	$\left(\frac{\bar{\phi}_2}{\phi_{2,a.m.}}\right)_{min} \%$	$\left(\frac{\bar{\phi}_2}{\phi_{2,a.m.}}\right)_{max} \%$
3.1.1	1.1922	1.2729	1.7681	3.6378
3.1.2	1.2092	1.3064	1.5976	2.7534
3.1.3	1.2202	1.3331	1.5223	2.3827
3.2.1	1.1907	1.2677	1.7831	3.6357
3.2.2	1.2087	1.3035	1.6114	2.7508
3.2.3	1.2202	1.3318	1.5349	2.3806
3.3.1	1.1854	1.2884	1.8549	3.6245
3.3.2	1.2064	1.3374	1.6750	2.7429
3.3.3	1.2193	1.3741	1.5923	2.3761

Table 31: Benchmark / Atomic Mix Ratio of Group Scalar Flux Solutions for Set 3; Disk-Matrix Statistics, Vacuum Boundaries

The underestimation of the atomic mix approximation is evident, since all of the ratios are greater than unity. The atomic mix approximation is a fair predictor of the fast and thermal group flux shape: the maximum and minimum difference in the ratio vary between $\approx 1.2 - 1.4\%$ in the fast group and between $\approx 1.9 - 3.6\%$ in the thermal group.

4.9 Disk-Matrix Mixing Statistics - Reflecting Boundaries

In this section, Set 3 calculations are again considered, but with reflecting boundaries to assess the effect of leakage on ensemble quantities. The calculation designation is reduced to “calculation x.z”, where only $x = 3$ is considered in this section.

4.9.1 The k -Eigenvalue

The k -eigenvalue data is given in Table 32 below. A trend similar to that of the vacuum boundary case is discovered. There is a non-linear increase in the ensemble

average k-eigenvalue as k_∞ increases. A similar trend is present in the standard deviation.

Ensemble k-Eigenvalue Results			
Calc.	\bar{k}	$\sigma_{\bar{k}}$	$(\frac{\sigma_{\bar{k}}}{\bar{k}}\%)$
3.1	0.5926	0.06498	10.97
3.2	0.9964	0.10693	10.73
3.3	1.3883	0.14659	10.56

Table 32: k-Eigenvalue Results for Set 3; Disk-Matrix Statistics, Reflecting Boundaries

The k-eigenvalue probability distribution functions for these three calculations are shown in Figures 59 - 61 below. These k-eigenvalue PDFs resemble a Gaussian distribution with a truncation of the tail on the right-hand side. All three plots show a similar relative standard deviation.

Figure 62 shows that an increase in k_∞ increases the range of possible k-eigenvalues, with a shift toward larger k-eigenvalues. The shape of the k-eigenvalue PDF is not greatly impacted by a change in k_∞ .

4.9.2 Scalar Flux

Tables 33 - 34 give results for the fast and thermal group scalar flux, respectively. As shown in the example flux plots below (Figures 63 - 66), all of the Set 3 ensemble average solutions do not have the flat shape as in the other two sets of mixing statistics. The fast group ensemble flux shape decreases from left-to-right. The thermal group ensemble flux shape shows a minimum near the left-hand side of the system, increasing further into the system. The minimum and maximum of these quantities illustrate the effect of the variable parameters on the shape of these two solutions. Similar maxima and minima designate a flat profile, while

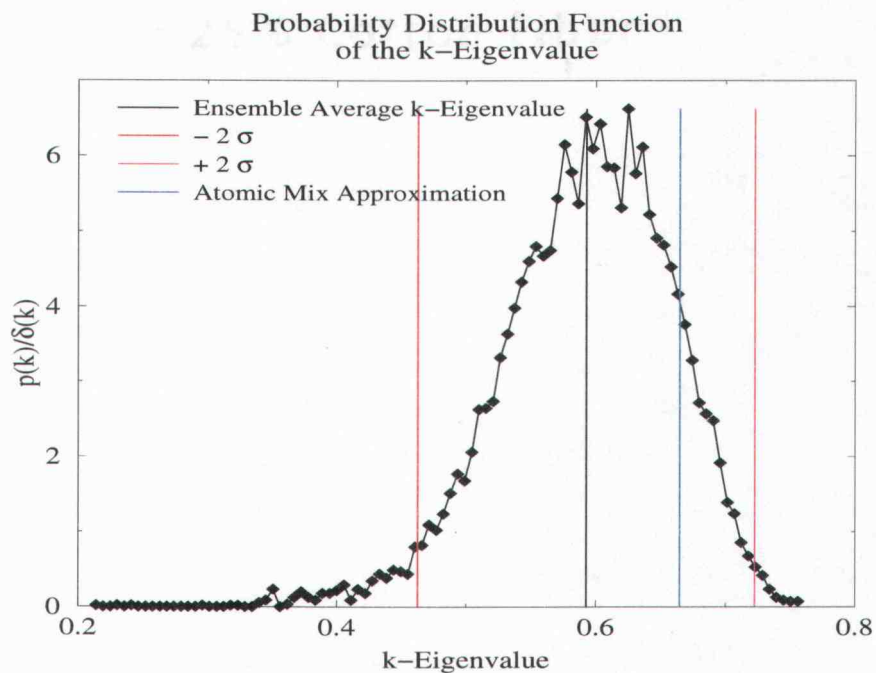


Figure 59: k-Eigenvalue PDF - Calculation 3.1

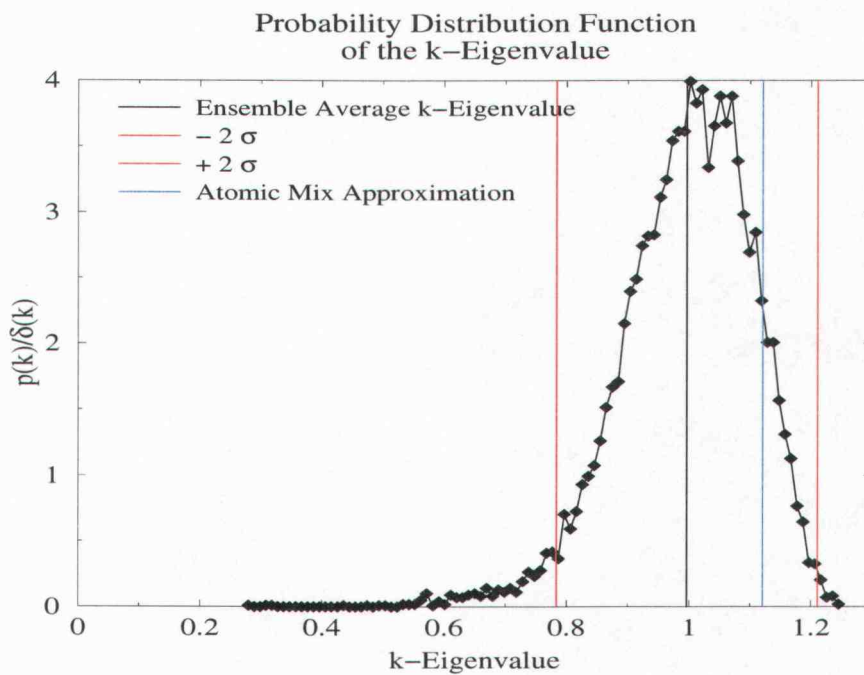


Figure 60: k-Eigenvalue PDF - Calculation 3.2

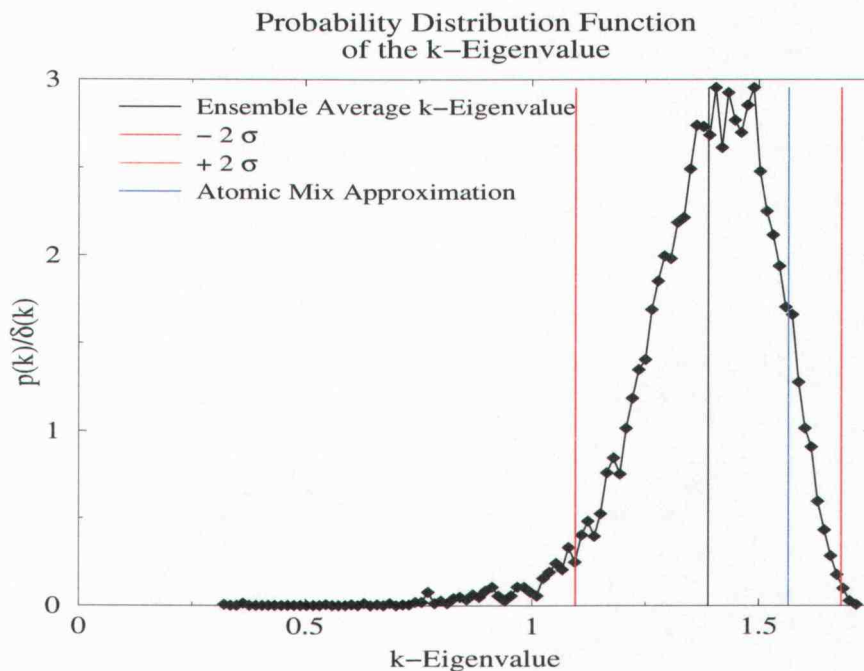


Figure 61: k-Eigenvalue PDF - Calculation 3.3

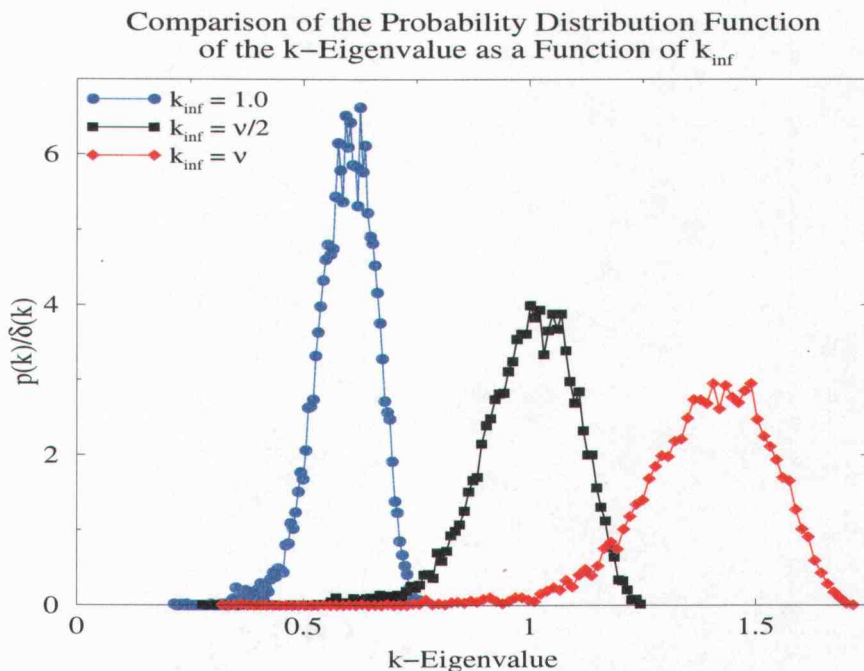


Figure 62: k-Eigenvalue PDF - Calculation 3.1 - Calculation 3.3

dissimilar maxima and minima indicate a peaked flux profile.

Tables 33 - 34 give results for the fast and thermal group scalar flux, respectively. These results reveal that as k_∞ increases the group ensemble average scalar flux and standard deviation decreases. This is the inverse behavior of the ensemble average and standard deviation of the k-eigenvalue. The relative standard deviation is very consistent in the fast group as a function of increasing k_∞ , and decreases in the thermal group. The magnitude of the fast group scalar flux is greater than that of the thermal group. However, the relative standard deviation is much larger in the thermal group.

Fast Group Flux Results						
Calc.	$(\bar{\phi}_1)_{min}$	$(\bar{\phi}_1)_{max}$	$(\sigma_{\bar{\phi}_1})_{min}$	$(\sigma_{\bar{\phi}_1})_{max}$	$\left(\frac{\sigma_{\bar{\phi}_1}}{\bar{\phi}_1}\%\right)_{min}$	$\left(\frac{\sigma_{\bar{\phi}_1}}{\bar{\phi}_1}\%\right)_{max}$
3.1	4.6735	4.7881	0.6401	0.8859	13.57	18.52
3.2	2.7784	2.8541	0.3749	0.5518	13.37	19.34
3.3	1.9935	2.0520	0.2679	0.4165	13.33	20.31

Table 33: Fast Group Flux Results for Set 3; Disk-Matrix Statistics, Reflecting Boundaries

Thermal Group Flux Results						
Calc.	$(\bar{\phi}_2)_{min}$	$(\bar{\phi}_2)_{max}$	$(\sigma_{\bar{\phi}_2})_{min}$	$(\sigma_{\bar{\phi}_2})_{max}$	$\left(\frac{\sigma_{\bar{\phi}_2}}{\bar{\phi}_2}\%\right)_{min}$	$\left(\frac{\sigma_{\bar{\phi}_2}}{\bar{\phi}_2}\%\right)_{max}$
3.1	0.7259	1.4724	1.5751	2.8481	193.08	217.90
3.2	0.5630	1.0174	1.0303	1.7562	171.73	183.61
3.3	0.4957	0.8261	0.8127	1.3099	155.36	164.81

Table 34: Thermal Group Flux Results for Set 3; Disk-Matrix Statistics, Reflecting Boundaries

Representative plots are given for the group scalar fluxes (including the $\pm 2\sigma$ confidence interval) and the atomic mix approximation in Figures 63 - 66 for calculation 3.1 and calculation 3.3. As in the vacuum boundary case, the flux profile

for all of the Set 3 calculations with reflecting boundaries has a small asymmetric peak in the fast group and depression in the thermal group ensemble average scalar fluxes near the left-hand side of the system.

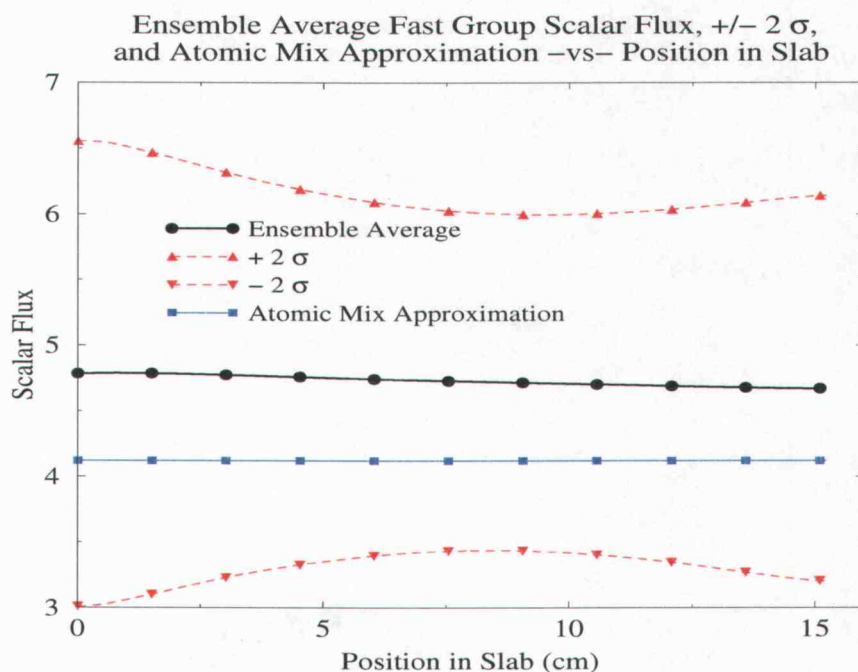


Figure 63: Ensemble Average Fast Group Flux - Calculation 3.1

4.9.3 The Atomic Mix Approximation

A comparison of the atomic mix prediction of ensemble average k -eigenvalue is given below in Table 35. This approximation yields conservative estimates of \bar{k} with relative errors around $\approx 12\%$. The atomic mix prediction of \bar{k} always is contained in the 2σ confidence interval, but always lies outside of the 1σ confidence interval.

For all of the calculations considered, atomic mix under-predicts the magnitude of the flux in both energy groups. This is evident in the representative plots of

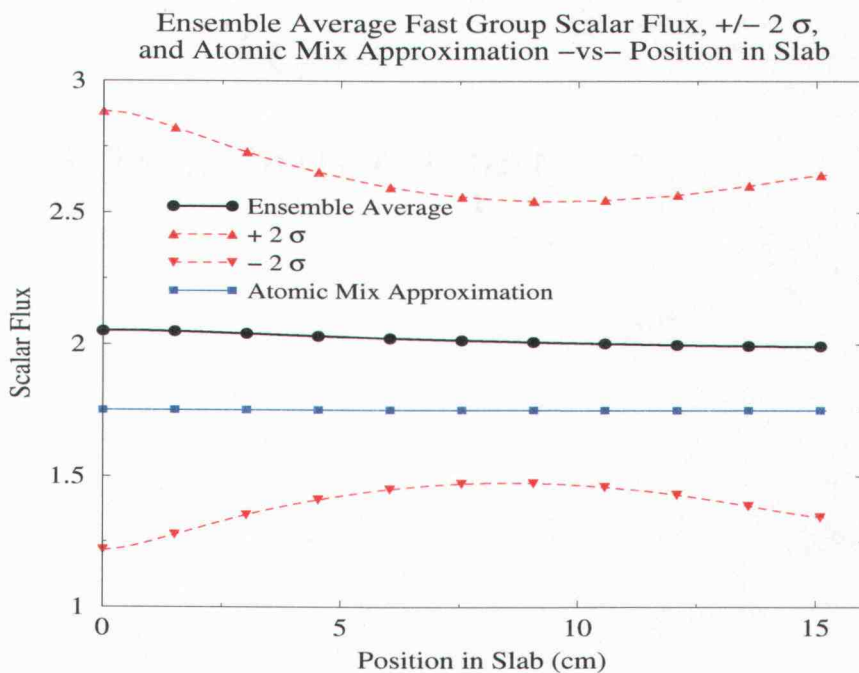


Figure 64: Ensemble Average Fast Group Flux - Calculation 3.3

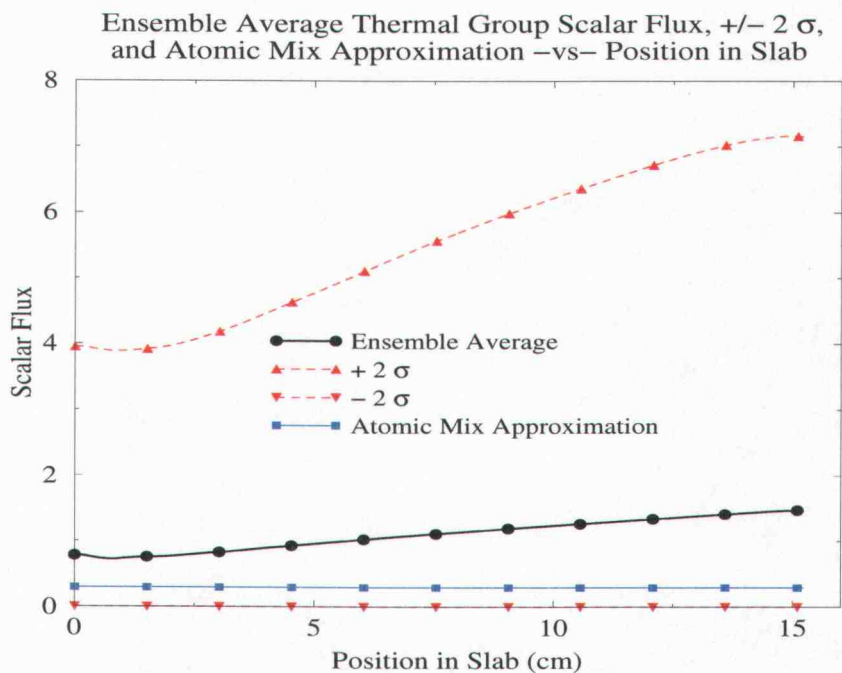


Figure 65: Ensemble Average Thermal Group Flux - Calculation 3.1

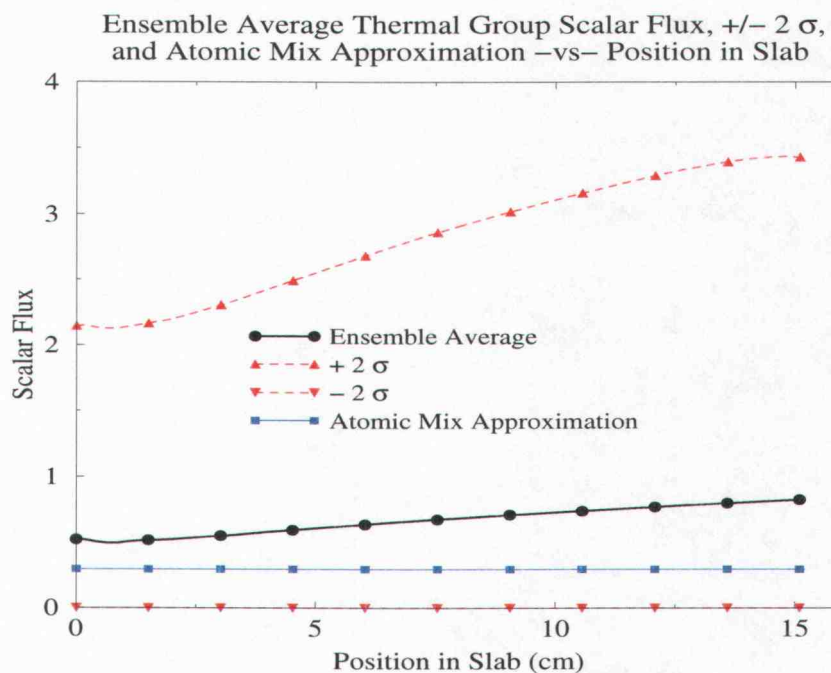


Figure 66: Ensemble Average Thermal Group Flux - Calculation 3.3

Atomic Mix k-Eigenvalue Comparison			
Calc.	k	$k_{a.m.}$	%R.E.
3.1	0.5926	0.6646	12.14
3.2	0.9964	1.1209	12.50
3.3	1.3883	1.5653	12.75

Table 35: Atomic Mix Prediction of the Ensemble Average k-Eigenvalue for Set 3; Disk-Matrix Statistics, Reflecting Boundaries

Figures 63 - 66 for calculation 3.1 and calculation 3.3.

A comparison of the atomic mix prediction of the fast and thermal group scalar fluxes is given below in Table 36.

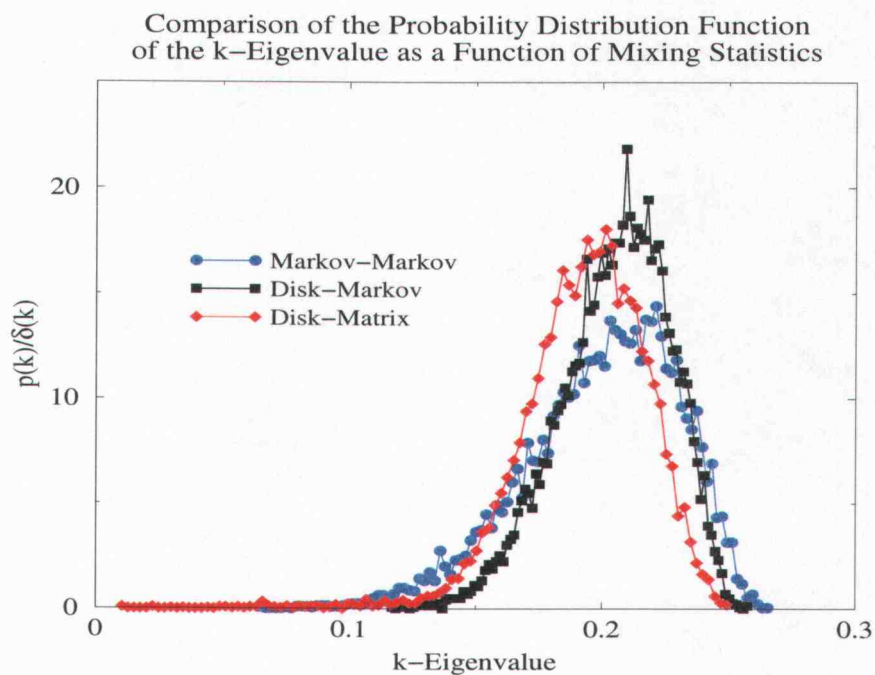
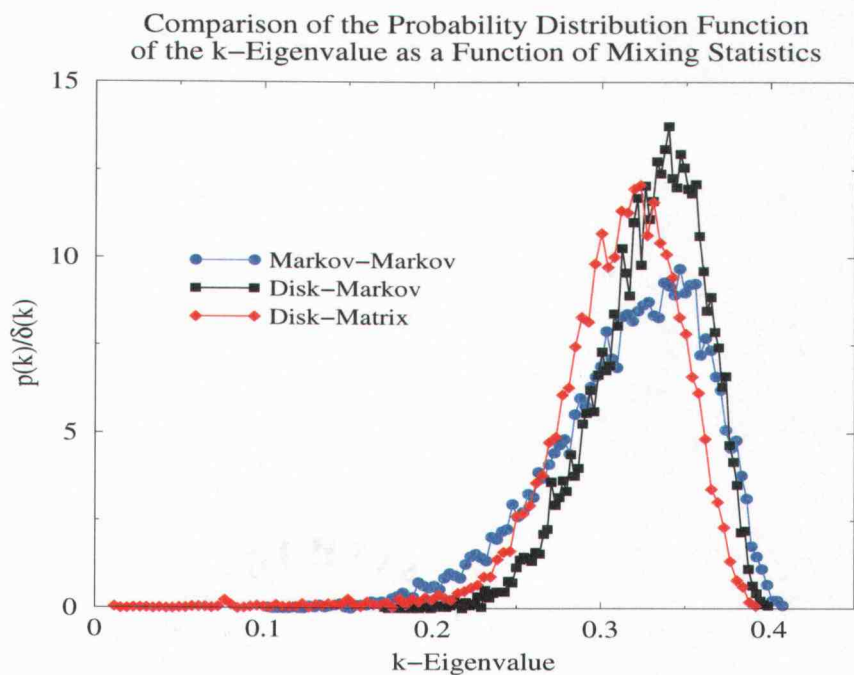
Atomic Mix Group Scalar Flux Comparison				
Calc.	$\left(\frac{\bar{\phi}_1}{\phi_{1,a.m.}}\right)_{min} \%$	$\left(\frac{\bar{\phi}_1}{\phi_{1,a.m.}}\right)_{max} \%$	$\left(\frac{\bar{\phi}_2}{\phi_{2,a.m.}}\right)_{min} \%$	$\left(\frac{\bar{\phi}_2}{\phi_{2,a.m.}}\right)_{max} \%$
3.1	1.1338	1.1616	2.4489	4.9680
3.2	1.1370	1.1678	1.8993	3.4333
3.3	1.1392	1.1724	1.6723	2.7880

Table 36: Ensemble Average / Atomic Mix Ratio of Group Scalar Flux Solutions for Set 3; Disk-Matrix Statistics, Reflecting Boundaries

The underestimation of the atomic mix approximation is evident, since all of the ratios are greater than unity. The atomic mix approximation is again a fair predictor of the flux shape in the fast group: the maximum and minimum difference in the ratio vary between $\approx 1.13 - 1.17\%$. The atomic mix approximation of the thermal group scalar flux shape differs more significantly: the maximum and minimum ratios vary between $\approx 1.7 - 5\%$. For relatively flat flux profiles, atomic mix will predict the flux shape fairly well.

4.10 Markov-Markov, Disk-Markov, and Disk-Matrix PDF Comparison

The following three representative plots (Figures 67 - 69) show the impact of the three different mixing statistics on the k-eigenvalue PDF shape for calculations with the same values of k_∞ and c^{fuel} . In these three figures, there is an increasing value of k_∞ for a fixed value of c^{fuel} .

Figure 67: k -Eigenvalue PDF Mixing Statistics Comparison - Calculation x.2.1Figure 68: k -Eigenvalue PDF Mixing Statistics Comparison - Calculation x.2.2

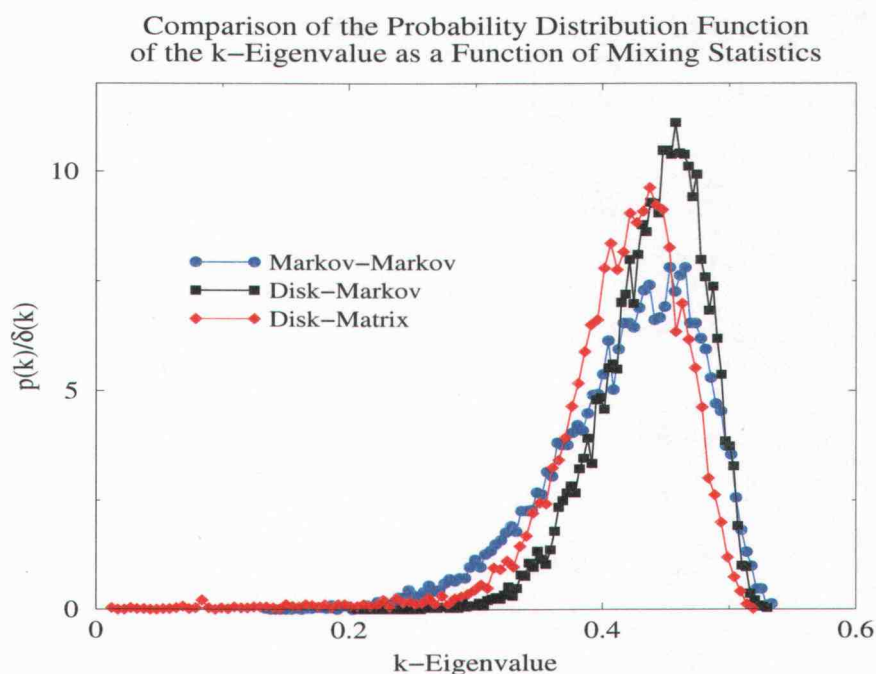


Figure 69: k -Eigenvalue PDF Mixing Statistics Comparison - Calculation x.2.3

The standard deviation of the segment lengths of the Disk distribution is a factor of ≈ 3.52 smaller than in the standard deviation of the Markovian distribution. This reduced randomness in the segment length size of the fuel material for the Set 2 calculations shows that the k -eigenvalue PDF assumes a less skewed, normal looking distribution when compared with the k -eigenvalue PDF of the Set 1 calculations. The standard deviation of the segment lengths of the Matrix distribution is a factor of ≈ 1.63 larger than standard deviation of the Markovian distribution. For the Set 3 calculations, the PDF retains the normal looking distribution of the Set 2 calculations, but develops a much longer tail on the left side of the PDF due to the increased randomness in the moderator material using the Matrix distribution. The PDFs of Set 3 calculations also shift toward lower k -eigenvalues relative to the other two distributions.

4.11 Summary

Trends were identified in the statistical solution of ensemble group scalar flux and the k-eigenvalue when varying k_{∞} and c^{fuel} . The impact of these variable parameters on the group flux profile and the k-eigenvalue PDF was evaluated. Representative plots of the group flux and k-eigenvalue PDF were provided. Tables of data summarizing trends from all of the calculations performed were also provided. These trends were identified considering both vacuum and reflecting boundaries for each of the three sets of statistical distributions considered.

5 CONCLUSIONS

5.1 Introduction

In this chapter, the results presented in Chapter 4 are discussed. In particular, the behavior of the ensemble average k-eigenvalue, the ensemble average group flux, and the accuracy of the atomic approximation as a model for neutron transport in a binary stochastic multiplying medium are analyzed. Some overall conclusions, as well as some recommendations for further research for benchmarking and modeling development for stochastic media transport are given.

5.2 k-Eigenvalue

With an increase in k_∞ with a constant c^{fuel} there was a non-linear increase in both the ensemble average k-eigenvalue and standard deviation. For the Set 1 and Set 2 calculations, this factor of increase is not as great for the standard deviation as it is for the ensemble average. This effect is shown by a decreasing relative standard deviation with increasing k_∞ for both vacuum and reflecting boundaries. In the case of the Set 3 calculations, an increase in k_∞ results in a very slight increase in the relative standard deviation with vacuum boundary conditions, and a very slight decrease with reflecting boundary conditions. The effect of an increase in the ensemble average k-eigenvalue is expected with an increased probability of fission per absorption, achieved with the increase in k_∞ .

Changes in c^{fuel} do not significantly impact the ensemble average k-eigenvalue or standard deviation for the two smallest values ($c^{fuel} \leq 0.5$) for constant k_∞ , but does result in a small increase in the relative standard deviation. There is a

more noticeable increase in these two quantities for the largest value of c^{fuel} . For fixed $\sigma_{a,1}^{fuel}$, an increase in $\sigma_{s,1\rightarrow 1}^{fuel}$ increases σ_1^{fuel} , giving an increased probability of overall interaction. For $c^{fuel} = 0.9$, 90% of the total interactions that occur will be within-group scattering. This allows more fast neutrons born in the fuel to escape the fuel and enter the moderator, where they can thermalize and subsequently cause more fission. This results in a broadening of the k-eigenvalue PDF toward larger k-eigenvalues similar to an increase in k_∞ for a fixed c^{fuel} .

The trends discussed above were evident in all three sets of mixing statistics considered. The ensemble average k-eigenvalue in the Set 2 mixing statistics is greater than that in Set 1. In Sets 1 and 2, the same fuel mean segment length is used, but the Disk distribution has a significantly smaller (factor of ≈ 3.52) standard deviation than the Markovian distribution. In the case of the Markovian distribution, the fuel segment lengths can be arbitrarily large or small. The Disk distribution has a finite maximum fuel segment length. The Disk fuel distribution provides better fuel utilization, indicated by the higher ensemble average k-eigenvalue. This is due to smaller segment lengths of fuel overall, causing less fast absorption and more moderation. This effect causes more fission on average, and an increase in the ensemble average k-eigenvalue. The smallest ensemble average k-eigenvalues occurred for the Set 3 calculations. The ensemble fuel content is reduced relative to the other two sets of mixing statistics. This is due to the large standard deviation of the segment lengths in the moderator when using the Matrix distribution (a factor of ≈ 1.63 greater than the Markovian distribution).

The shape of the k-eigenvalue PDF is similar to a Gaussian distribution with a truncated tail on the side of the highest k-eigenvalue. This is the same qualitative shape witnessed by Williams [Wil 00a] - [Wil 01], obtained with the FGH method.

The shape can never be exactly Gaussian, as there exists a minimum and maximum k-eigenvalue for any random system [Wil 00a]. This truncated Gaussian-like shape indicates the optimal configuration (highest k), is a low probability event. Any deviation from this optimal configuration causes a rapid decrease in the k-eigenvalue, yielding the Gaussian-like peak roughly centered about the ensemble average.

The impact of an increasing k_{∞} causes a broadening in the PDF toward larger k-eigenvalues as a consequence of the higher probability of fission per absorption in the fuel. This broadening is also noticeable for the largest value of c^{fuel} because of the increased probability of moderation and subsequent fission. The shapes of these broadened PDFs are relatively unchanged, always resembling a skewed Gaussian distribution. The mixing statistics do impact the shape of the k-eigenvalue PDF. The smaller standard deviation of the fuel segment length in the case of the Disk distribution of Set 2 and 3, causes the PDF to take on a more normal shape. The k-eigenvalue PDFs resulting from the Set 3 calculations show a similar distribution shape to that of Set 2, but are slightly shifted toward smaller k-eigenvalues. A much longer tail develops showing that such variation in the moderator segment lengths as given by the Matrix distribution, results in many more low probability configurations which yield small k-eigenvalues.

The addition of reflecting boundaries causes an increase in the k-eigenvalue, with no noticeable affect on the shape of the k-eigenvalue PDF.

5.3 Scalar Flux

The ensemble average and standard deviation of the scalar flux exhibit trends opposite those of the k-eigenvalue due to the reciprocal relationship of the flux

and k-eigenvalue. An increase in k_∞ for fixed values of c^{fuel} , causes a decrease in the group flux magnitude. The group flux is decreased by a factor of the increase in the ensemble average k-eigenvalue. There is also a corresponding decrease in the standard deviation. For Set 1 and 2 with vacuum boundaries, the relative standard deviation of the group fluxes decreases with increasing k_∞ and fixed c^{fuel} . The relative standard deviation is roughly constant for the smallest values of c^{fuel} with fixed k_∞ and shows an increase for the largest value of c^{fuel} . In the case of Set 3 calculations with vacuum boundaries, the relative standard deviation increases with increasing k_∞ and fixed c^{fuel} . The relative standard deviation is roughly constant for the smallest values of c^{fuel} with fixed k_∞ and shows the most drastic increase for the largest value of c^{fuel} . All sets of statistics showed a decrease in the relative standard deviation with an increase in k_∞ when using reflecting boundaries.

The fast group scalar flux has a much lower relative standard deviation than the thermal group scalar flux. This indicates less variation in the fast group scalar flux profile from realization to realization. The cross sections in the fast group are such that the mean free path of neutrons is larger. Greater interaction probabilities in the thermal group result in steeper gradients in the flux profile. Averaging over the ensemble of these realizations, gives a larger standard deviation in the thermal group. Very large standard deviations occur for these sets of mixing statistics. For the fast group ensemble average scalar flux, the relative standard deviation ranges from $\approx 12 - 150\%$ with vacuum boundaries, and from $\approx 12 - 20\%$ with reflecting boundaries. The thermal group relative standard deviation of the ensemble average scalar flux varied from $\approx 38 - 372\%$ with vacuum boundaries, and $\approx 62 - 218\%$ for reflecting boundaries. With such large standard deviation, a solution consisting of only the ensemble average scalar flux does not contain enough statistical infor-

mation to be meaningful. Higher statistical moments of the solution are necessary.

In the case of Set 1 with vacuum boundaries, the group flux profile has the cosine shape characteristic of a homogeneous medium. This shape takes on a greater peaked shape for the largest values of c^{fuel} . In the case of reflecting boundaries the shape takes on a flatter profile. Since the segment length distributions are the same in each material for Set 1, the flux profiles of each realization average together nicely, illustrating a similar profile to that of a homogeneous medium.

In the case of Set 2 with vacuum boundaries, the group flux profile also has this characteristic cosine shape (again with a more peaked distribution for the largest value of c^{fuel}) with a small asymmetry on the left-hand side of the system. In the case of reflecting boundaries, this small asymmetry is also present. This asymmetric behavior is caused by the small segment length standard deviation in the fuel material when using the Disk distribution rather than the Markovian distribution.

The algorithm for randomly populating the system proceeds from left to right, and as a result, the left-hand side is the most ordered point of the system. Further into the slab, the material at any given point is much more random, as it is dependent upon the random material segments that have come before it. This increased variation (as a function of the distance into the system from the left edge) is due mostly to the large variation of the moderator material segment length. Recalling Eq. (80), and considering mean chord lengths of 0.746 cm and 1.153 cm used in the fuel and moderator materials respectively, the probability of a fuel segment appearing as the first material segment of the system is $\approx 39\%$. Fuel segment lengths are much less variable than the moderator segment lengths. Therefore, if a fuel segment is chosen as the first material segment on the left-hand side of the

system, it will be of a less variable size than if a moderator segment is chosen. If a moderator segment is chosen and is small it will be followed by a fuel segment of a less variable size. The flux profile will look similar in this scenario to the flux profile if a fuel segment was chosen as the first material segment. If a large moderator segment is chosen, the adjoining fuel segment will be far away from the left edge, in a more random area of the system. The ensemble average flux profile appears to preferentially have a fuel segment on or near the left edge, giving a small fast flux peak and small thermal flux depression at this location. This characteristic of the system population algorithm was emphasized by calculations performed using a fixed segment length for the fuel material.

The addition of reflecting boundaries has no appreciable effect on the relative standard deviation of the Set 2 fast group scalar flux. The relative standard deviation of the thermal group scalar flux is increased greatly. This is again due to the choice of cross sections. Since no neutrons leak out of the system, and there is a small amount of absorption in the fast group (only in the fuel) compared to the amount of absorption in the thermal group (fuel and moderator) neutrons will be preferentially absorbed in the thermal group, resulting in steeper gradients for individual realization and an overall larger standard deviation for reflecting boundaries.

In the case of Set 3 with vacuum boundaries, the ensemble average group flux profiles have a skewed cosine shape (with a more peaked flux profile for the largest value of c^{fuel}). Like in Set 2, a small asymmetry on the left-hand side is present due to the dissimilar segment length distribution in the fuel and moderator. This asymmetry is greater in Set 3 than in Set 2 because of the increases variability in the moderator segment (Matrix) distribution. The ensemble average fast group

flux peak is shifted toward the left edge of the system, while the ensemble average thermal group peak is shifted toward the right edge. Since the standard deviation of the segment lengths is ≈ 1.63 greater in the Matrix distribution than in the Markovian distribution, longer segments of moderator are more frequent. This makes it more likely (relative to the Set 1 or Set 2 calculations) that a moderator segment will appear near the right hand side than a fuel segment. Therefore, the ensemble average fast group flux peak occurs where there is a higher average number of fuel segments (near the left-hand side). Likewise, the ensemble average thermal group flux peaks where there is a higher average number of moderator segments (near the right-hand side).

This same effect is again displayed when using reflecting boundaries, but with a much flatter flux profile. The addition of reflecting boundaries flattens and decreases the group relative standard deviation a great deal. This is due to the elimination of leakage with increased probability of large moderator segment lengths. The asymmetries present in the flux profile are clearly a consequence of the numerical algorithm employed to populate the slab with random material segments. Beginning populating the slab from both sides for the same number of realizations, would give a more symmetric ensemble average flux profile.

5.4 Atomic Mix

Current numerical models used in the design of nuclear reactors predict the k -eigenvalue and scalar flux very accurately. In designing nuclear systems of a stochastic nature, models which can predict the k -eigenvalue and flux profiles with the same level of accuracy are necessary. The atomic mix approximation gives very inaccurate predictions of ensemble average quantities. The large relative errors of

the atomic mix predictions of the benchmark quantities are unacceptably high with respect to current modeling practices. Relative error in predicting the ensemble average k-eigenvalue errors range from $\approx 12 - 22\%$ using vacuum boundaries, and from $\approx 6 - 13\%$ when using reflecting boundaries.

Since the flux solution is scaled by an arbitrary factor, it is more important to determine whether or not the atomic mix prediction is able to predict the correct flux shape, than the overall relative error of the predicted magnitude. For those statistics considered, the atomic mix approximation is better able to predict ensemble average flux solutions which are symmetric and smooth, and are the result of mixing statistics with small standard deviation of the segment lengths. Only for systems where the heterogeneous nature of the system gets effectively averaged out can atomic mix be expected to be an accurate prediction of the ensemble average group flux and k-eigenvalue.

This result is consistent with previously published results. The research conducted on the development of models for transport in binary stochastic media indicate that in order for a model to reasonably predict the behavior of a stochastic media system, it must take into account the mean and standard deviation of the material distributions. Atomic mix only takes into account the mean segment length of the material distributions. Since the same material mean segment lengths are used in each set of mixing statistics, the atomic mix approximation gives the same result for each set of mixing statistics considered. This makes it a poor model for such a system where ensemble quantities depend on higher statistical information than the mean.

The atomic mix approximation can only predict ensemble average quantities, and is known to be inaccurate in predicting these quantities when segment lengths

are larger than a mean free path of a particle. A more useful model of stochastic media transport should not only accurately predict ensemble average quantities, but also include predictions of higher statistical moments such as the standard deviation. For transport in stochastic media, only this type of solution will be meaningful.

5.5 Overall Conclusions and Future Work

The results of this study are in agreement with past observations of the qualitative shape of the k-eigenvalue PDF. This shape has been observed for k-eigenvalue problems in binary stochastic media simulated with very different numerical techniques. Statistical moments of the flux solution were also investigated, revealing a large standard deviation. Asymmetric benchmark flux solutions may result when using different segment distributions in the materials. This is an effect of the numerical simulation algorithm, and is likely not physical. Further benchmarking is necessary to research variability in other system parameters. It is of the utmost importance to sample from accurately determined distribution functions of material segment lengths in order to perform meaningful benchmark calculations for the system of interest.

The systems with vacuum boundaries considered in this study are, for the most part, leakage dominated. This may smooth out the effect of random fuel segments compared to a more absorption dominated system. For a less leakage dominated system, increasing the c^{fuel} parameter may have a more noticeable effect.

Accurate models of stochastic medium k-eigenvalue problems must reproduce those trends observed here for both the k-eigenvalue and the group scalar flux. These models will definitely need to take into account both the mean and standard

deviation of the segment length distributions. They also should produce accurate predictions of both ensemble average and the standard deviation of benchmark quantities in order to give statistically meaningful results for neutron transport problems in a stochastic medium.

Simulations of neutron transport in stochastic media will have to be extended into multi-dimensions to better determine the real effect of spatial randomness of the medium components. Assembly level parameterization of random “assemblies” can be compiled in order to determine if a modeling treatment, such as the widely used nodal method, could be applied to a stochastic medium.

BIBLIOGRAPHY

- [Ada 89] Adams, M.L., Larsen, E.W., and Pomraning, G.C., "Benchmark Results for Particle Transport in a Binary Markov Statistical Medium", *Journal of Quantitative Spectroscopy and Radiation Transfer*, **42**, 253 (1989).
- [Ada 98] Adams, M.L., Walters, W.F., and Warening, T.A., "Characteristics Methods in Thick Diffusive Problems", *Nuclear Science and Engineering*, **130**, 18 (1998).
- [Ada 04] Adams, M.L. "Computational Methods for Particle-Transport Problems (Lecture Notes for Texas A&M NE 654 Course - Winter 2004)", (2004).
- [Ada 92] Adams, M.L. and Martin, W.R., "Diffusion Synthetic Acceleration of Discontinuous Finite Element Transport Iterations", *Nuclear Science and Engineering*, **111**, 145 (1992).
- [Bel 70] Bell, G.I. and Glasstone, S., **Nuclear Reactor Theory**, Robert E. Krieger Publishing Co., Inc., Malabar, FL (1970).
- [Boi 90] Boisse, P., "Radiative Transfer Inside Clumpy Media: The Penetration of UV Photons Inside Molecular Clouds", *Astronomy and Astrophysics*, **228**, 483 (1990).
- [Cha 61] Chandrasekhar, S., **Hydrodynamic and Hydromagnetic Stability**, Oxford University Press, New York, NY (1961).
- [Dav 04] Davis, I.M., Palmer, T.S., and Larsen, E.W., "A Comparison of Binary Stochastic Media Transport Models in 'Solid-Void' Mixtures", *PHYSOR 2004 - The Physics of Fuel Cycles and Advanced Nuclear Systems: Global Developments*, Chicago, Illinois, April 25-29 (2004).
- [Don 03a] Donovan, T.J. and Danon, Y., "Application of Monte Carlo Chord-Length Sampling Algorithms to Transport Through a Two-Dimensional Binary Stochastic Mixture", *Nuclear Science and Engineering*, **143**, 226 (2003).
- [Don 03b] Donovan, T.J., Sutton, T.M., and Danon, Y., "Implementation of Chord Length Sampling for Transport Through a Binary Stochastic Mixture", *Nuclear Mathematical and Computational Sciences: A Century in Review a Century Anew*, Gatlinburg, Tennessee, April 6-11 (2003).
- [Dud 76] Duderstadt, J.J. and Hamilton, L.J., **Nuclear Reactor Analysis**, John Wiley & Sons, Inc., New York (1976).

- [Ede 93] Edenius, M. and Forssen, B., **CASMO-3: A Fuel Assembly Burnup Program User's Manual, Version 4.7**, Studsvik of America, Inc, Newton, MA (1993).
- [Fri 90] Frisch, H., Pomraning, G.C., and Zweifel, P.F., "An Exact Analytical Solution of a Radiative Transfer Problem in a Binary Mixture", *Journal of Quantitative Spectroscopy and Radiation Transfer*, **43**, 271 (1990).
- [Hof 01] Hoffman, J.D., **Numerical Methods for Engineers and Scientists**, Marcel Dekker, Inc., New York, NY (2001).
- [Jah 01] Jahshan, S.N. and Singleterry, R.C., "The Effect of Stochastic Perturbation of Fuel Distribution on the Criticality of a One Speed Reactor and the Development of Multi-Material Multinomial Line Statistics", *Annals of Nuclear Energy*, **28**, 1697 (2001).
- [Jah 98] Jahshan, S.N., "The Stochastic Behavior of the Eigenvalue Due to Spatial Perturbation in the Fuel Distribution of the One-Speed Slab Reactor", *Nuclear Science and Engineering*, **130**, 85 (1998).
- [Lev 88] Levermore, C.D., Wong, J. and Pomraning, G.C., "Renewal Theory for Transport Processes in Binary Statistical Mixtures", *Journal of Mathematical Physics*, **29**, 995 (1988).
- [Lew 93] Lewis, E.E. and Miller, W.F., **Computational Methods of Neutron Transport**, American Nuclear Society, Inc., La Grange Park, IL (1993).
- [Mal 92] Malvagi, F. and Pomraning, G.C., "A Comparison of Models for Particle Transport Through Stochastic Mixtures", *Nuclear Science and Engineering*, **111**, 215 (1992).
- [Mil 01] Miller, D.S., Graziani, F., and Rodrigue, G., "Benchmarks and Models for the Time-Dependent Grey Radiation Transport With Material Temperature in Binary Stochastic Media", *Journal of Quantitative Spectroscopy and Radiation Transfer*, **70**, 115 (2001).
- [Ols 03] Olson, G.L, Morel, J.E., and Larsen, E.W., "Chord Length Distributions in Binary Stochastic Media in Two and Three Dimensions", *ANS Winter Meeting, New Orleans, Louisiana*, November 16-20 (2003).
- [Pom 91a] Pomraning, G.C., "The Effect of Random Material Density on Reactor Criticality", *Nuclear Science and Engineering*, **108**, 325 (1991).
- [Pom 91b] Pomraning, G.C., **Linear Kinetic Theory and Particle Transport in Stochastic Mixtures**, World Scientific Co. Pte. Ltd., Singapore (1991).

- [Pom 91c] Pomraning, G.C., "A Model for Interface Intensities in Stochastic Particle Transport", *Journal of Quantitative Spectroscopy and Radiation Transfer*, **46**, 221 (1991).
- [Pom 88] Pomraning, G.C., "Radiative Transfer in Random Media with Scattering", *Journal of Quantitative Spectroscopy and Radiation Transfer*, **40**, 479 (1988).
- [Pom 90b] Pomraning, G.C., "Radiative Transfer in Rayleigh-Taylor Unstable ICF Pellets", *Laser and Particle Beams*, **8**, 741 (1990).
- [Pom 89] Pomraning, G.C., "Statistics, Renewal Theory, and Particle Transport", *Journal of Quantitative Spectroscopy and Radiation Transfer*, **42**, 279 (1989).
- [Pom 99] Pomraning, G.C., "A Stochastic Eigenvalue Problem", *Annals of Nuclear Energy*, **26**, 217 (1999).
- [Pom 98] Pomraning, G.C., "Transport in Discrete Stochastic Mixtures", *Transport Theory and Statistical Physics*, **27**, 405 (1998).
- [Pom 96a] Pomraning, G.C., "Transport Theory in Discrete Stochastic Mixtures", *Advances in Nuclear Science and Technology*, **24**, 47 (1996).
- [Pom 96b] Pomraning, G.C., "The Variance in Stochastic Transport Problems with Markovian Mixing", *Journal of Quantitative Spectroscopy and Radiation Transfer*, **56**, 626 (1996).
- [San 89] Sanchez, R., "Linear Kinetic Theory in Stochastic Media", *Journal of Mathematical Physics*, **30**, 2498 (1989).
- [San 91] Sanchez, R. and Pomraning, G.C., "A Statistical Analysis of the Double Heterogeneity Problem", *Annals of Nuclear Energy*, **18**, 371 (1991).
- [Ste 02] Stephens, G.L., Vane, D.G., and Boain, R.J., et. al., "The CloudSat Mission and the A-Train", *Bulletin of the American Meteorological Society*, **83**, 237 (2002).
- [Su 93] Su, B. and Pomraning, G.C., "Benchmark Results for Particle Transport in Binary Non-Markovian Mixtures", *Journal of Quantitative Spectroscopy and Radiation Transfer*, **50**, 211 (1993).
- [Su 94] Su, B. and Pomraning, G.C., "Limiting Correlation Length Solutions in Stochastic Radiative Transfer", *Journal of Quantitative Spectroscopy and Radiation Transfer*, **51**, 893 (1994).

- [Su 95] Su, B. and Pomraning, G.C., "Modification of a Previous Higher Order Model for Particle Transport in Binary Stochastic Media", *Journal of Quantitative Spectroscopy and Radiation Transfer*, **54**, 779 (1995).
- [Tic 04] Tickner, J., "Simulating Nuclear Particle Transport in Stochastic Media Using Perlin Noise Functions", *Nuclear Instruments and Methods in Physics Research. Section B, Beam Interactions with Materials and Atoms*, **213**, 124 (2004).
- [Van 89] Vanderhaegen, D., and Deutsch, C., "Linear Radiation Transport in Randomly Distributed Binary Mixtures: A One-Dimensional and Exact Treatment for the Scattering Case", *Journal of Statistical Physics*, **54**, 331 (1989).
- [Wil 00a] Williams, M.M.R., "The Effect of Random Geometry on the Criticality of a Multiplying System", *Annals of Nuclear Energy*, **27**, 143 (1999).
- [Wil 00b] Williams, M.M.R., "The Effect of Random Geometry on the Criticality of a Multiplying System II: Extension to Resonance Absorption", *Annals of Nuclear Energy*, **27**, 517 (2000).
- [Wil 02] Williams, M.M.R., "The Effect of Random Geometry on the Criticality of a Multiplying System III: Three Dimensional Systems and Spherical Absorbers", *Nuclear Science and Engineering*, **141**, 13 (2002).
- [Wil 03a] Williams, M.M.R., "The Effect of Random Geometry on the Criticality of a Multiplying System IV: Transport Theory", *Nuclear Science and Engineering*, **143**, 1 (2003).
- [Wil 03b] Williams, M.M.R., "The Effect of Random Geometry on the Criticality of a Multiplying System V: Influence of the Reflector", *Annals of Nuclear Energy*, **30**, 943 (2003).
- [Wil 01] Williams, M.M.R. and Larsen, E.W., "Neutron Transport in Spatially Random Media: Eigenvalue Problems", *Nuclear Science and Engineering*, **139**, 66 (2001).
- [Wil 03c] Williams, M.M.R., "The Probability Density Function of the Multiplication Factor Due to Small, Random Displacements of Fissile Spheres", *Annals of Nuclear Energy*, **30**, 17 (2003).
- [Yav 88] Yavuz, M., and Larsen, E.W., "Diffusion Synthetic Acceleration for S_N Problems with Reflecting Boundaries", *Transactions of the American Nuclear Society*, **56**, 305 (1988).

- [Zuc 94] Zuchuat, O., Sanchez, R., Zmijarevic, I., and Malvagi, F, "Transport in Renewal Statistical Media: Benchmarking and Comparison with Models", *Journal of Quantitative Spectroscopy and Radiation Transfer*, **51**, 689 (1994).